MULTILEVEL DIFFRACTIVE OPTICS FOR

BROADBAND APPLICATIONS

by

Nabil Mohammad

A dissertation submitted to the faculty of
The University of Utah
in partial fulfillment of the requirements for the degree of

Doctor of Philosophy

Department of Electrical and Computer Engineering

The University of Utah

December 2017

The University of Utah Graduate School

STATEMENT OF DISSERTATION APPROVAL

The dissertation of **Nabil Mohammad**

has been approved by the following supervisory committee members:

Rajesh Menon	, Chair	**6/15/2017** Date Approved
Carlos H. Mastrangelo	, Member	**6/15/2017** Date Approved
Michael A. Scarpulla	, Member	**6/15/2017** Date Approved
David Alan Schurig	, Member	**6/15/2017** Date Approved
Feng Liu	, Member	**6/15/2017** Date Approved

and by **Gianluca Lazzi** , Chair/Dean of

the Department/College/School of **Electrical and Computer Engineering**

and by David B. Kieda, Dean of The Graduate School.

ABSTRACT

Diffractive optics, an important part of modern optics, involves the control of optical fields by thin microstructured elements via diffraction and interference. Although the basic theoretical understanding of diffractive optics has been known for a long time, many of its applications have not yet been explored. As a result, the field of diffractive optics is old and young at the same time. The interest in diffractive optics originates from the fact that diffractive optical elements are flat and lightweight. This makes their applications into compact optical systems more feasible compared to bulky refractive optics. Although these elements demonstrate excellent diffraction efficiency for monochromatic light, they fail to generate complex intensity profiles under broadband illumination. This is due to the fact that the degrees-of-freedom in these elements are insufficient to overcome their strong chromatic aberration. As a result, despite their so many advantages over refractive optics, their applications are somewhat limited in broadband systems.

In this dissertation, a recently developed diffractive optical element, called a polychromat, is demonstrated for several broadband applications. The polychromat is comprised of linear "grooves" or square "pixels" with feature size in the micrometer scale. The grooves or pixels can have multiple height levels. Such grooved or pixelated structures with multilevel topography provide enormous degrees-of-freedom which in turn facilitates generation of complex intensity distributions with high diffraction efficiency under

broadband illumination. Furthermore, the super-wavelength feature size and low aspect ratio of this micro-optic make its fabrication process simpler. Also, this diffractive element is not polarization sensitive. As a result, the polychromat holds the potential to be used in numerous technological applications.

Throughout this dissertation, the broadband operation of the polychromat is demonstrated in four different areas, namely, photovoltaics, displays, lenses and holograms. Specifically, we have developed a polychromat-photovoltaic system which facilitates better photon-to-electron conversion via spectrum splitting and concentration, a modified liquid crystal display (LCD) that offers higher luminance compared to a standard LCD, a cylindrical lens that demonstrates super-achromatic focusing over the entire visible band, a planar diffractive lens that images over the visible and near-IR spectrum and broadband transmission holograms that project complex full-color images with high efficiency. In each of these applications, a unique figure of merit was defined and the height topography of the polychromat was optimized to maximize the figure of merit. The optimization was achieved with the aid of scalar diffraction theory and a modified version of direct binary search algorithm. Single step grayscale lithography was developed and optimized to fabricate these devices with the smallest possible fabrication errors. Rigorous characterization of these systems demonstrated broadband performance of the polychromat in all of the applications.

To my family

TABLE OF CONTENTS

LIST OF TABLES

Tables

ACKNOWLEDGEMENTS

with the confocal microscopy.

Last but not the least, I am deeply grateful to my family and friends for their understanding, encouragement, tremendous support and care.

CHAPTER 1

INTRODUCTION

1.1 Diffractive Optics

Optics describes the behavior and properties of light, a form of electromagnetic radiation. Electromagnetic radiation spans over a wide range of wavelengths (~1pm to 100Mm), from high frequency gamma rays to low frequency radio waves [1]. Optics generally deals with ultraviolet, visible and infrared light. The behavior and properties of light are governed by the same principles that describe all forms of electromagnetic radiation [2]. From our everyday experience it is well known to us that when light encounters an obstacle or an aperture it creates a shadow. This is true when the size of the obstacle or the aperture is much larger than the wavelength of the light. However, something interesting happens when the obstacle or aperture size is comparable to the wavelength of light. We see variations of intensity of light when we carefully examine the edges of the shadow [3]. This phenomenon is known as diffraction. The intensity distribution generated by the obstacle or aperture is known as the diffraction pattern. This diffraction pattern can be manipulated by properly engineering the obstacle or apertures. This has led to a very useful branch of optics called diffractive optics. Diffractive optical elements are a broad class of optical components that operate on the principle of diffraction and interference to modulate the optical wave-front to generate complex electromagnetic

fields in either far field or near-field regimes [4]. Because of planar geometries and light weight, diffractive optics offer numerous advantages over refractive optics and can easily be incorporated into compact optical systems that suffer from restricted form factor. Diffractive optics have a wide range of applications, for example, in gratings, diffractive lenses, beam splitters, beam shapers, line generators, Gaussian generators, polarizers, diffusers [5].

1.2 Broadband Diffractive Optics

Diffractive optics are usually designed for applications that utilize monochromatic light. Achieving complex diffraction patterns under broadband light using conventional diffractive optics is challenging due to the nature of strong chromatic aberration present in such elements [6-8]. Different approaches have been followed to design multiwavelength or broadband diffractive optics such as refractive-diffractive hybrid lenses [9-11], phase matching [12], iterative method based on the Gerchberg-Saxton algorithm [13], and direct binary search methods [14]. In the past, an extension of direct binary search algorithm was presented to design high efficiency broadband diffractive optics called a polychromat [15]. Previously, this broadband diffractive micro-optic was demonstrated as multicolor encoders [15], phase masks for 3D lithography [16] and dispersion elements in computational spectroscopy [17]. In this dissertation, the concept of polychromat is extended to demonstrate its application for solar spectrum splitting and concentration (Chapters 2 and 3), super achromatic focusing (Chapter 4), broadband imaging (Chapter 5), color splitting in liquid crystal displays (LCDs) (Chapter 6) and full-color transmission holograms (Chapter 7).

The polychromat is essentially pixelated microstructures (Figure 1.1(a)). For 1D case (Figure 1.1(b)), it is pixelated in one direction while uniform in the other and pixelated in both directions in the case of 2D form (Figure 1.1(c)). Applications of 1D form of the polychromat are described in Chapters 2, 3 and 4 while demonstrations of 2D form of this micro-optic are provided in Chapters 5, 6 and 7. The pixels have uniform widths (Δ) and the height of each pixel is quantized into multiple levels. In this work, Δ=3μm which is limited by the resolution of the tool used to fabricate the polychromat. Different maximum heights have been used for different applications. Number of quantization levels are determined by the fabrication process parameters as well as by the tool. The input light is diffracted by the polychromat microstructures and propagates a certain distance d. The diffracted light is detected on the X'Y' plane. The height profile can be optimized to achieve a particular diffraction pattern depending on the application.

The polychromat can be designed using a nonlinear optimization method based on direct binary search algorithm [15]. The algorithm is shown in Figure 1.2. In this algorithm, an initial height profile is chosen at the beginning. The initial height profiles can be chosen in different ways. In this work, a random height profile was chosen. The algorithm proceeds in an iterative manner. In each iteration, the height of each pixel is perturbed. As in diffractive phase element, height imparts local phase difference which is given by:

$$\phi(\mathrm{x},y,\lambda) = \frac{2\pi}{\lambda}(n(\lambda)-1)h(x,y) = \frac{2\pi}{\lambda}(n(\lambda)-1)\sum_{m}\sum_{n}\Delta h p_{m,n} rect(\frac{x-m\Delta_x}{\Delta_x})rect(\frac{y-n\Delta_y}{\Delta_y}) \quad (1.1)$$

Here, λ is the wavelength; n(λ) is the wavelength dependent refractive index of the material; 2π/λ is the wavevector; h(x,y) is the 2D height profile of the polychromat; Δh is

the unit height, Δh=H/(N-1), H is the maximum height; N is the number of levels; $p_{m,n} \epsilon [0,N] \cap Z$; rect() is the rectangle function; m,nϵ[-M/2,M/2] is the pixel index, (M+1) is the number of pixels in each direction; Δx and Δy are the pixel widths in x and y direction, respectively.

$$T(\mathrm{x}, y, \lambda) = \mathrm{e}^{\mathrm{i}\varphi(\mathrm{x},\lambda)} \quad (1.2)$$

From the transmission function of the polychromat, we can calculate the diffracted field at the image plane (x',y') located at distance d from the polychromat using Fresnel Transformation [18]:

$$U(\mathrm{x}', y', d, \lambda) = \frac{e^{ikd}}{i\lambda d} \int g_{illum}(\mathrm{x}, y, \lambda) \mathrm{T}(\mathrm{x}, y, \lambda) \mathrm{e}^{\mathrm{i}\frac{k}{2d}[(x-x')^2 + (y-y')^2]} \, dxdy \quad (1.3)$$

Here, U(x',y',d, λ) is the complex diffracted field and g_{illum}(x,y,λ) is the incident light. A figure of merit (FOM) can be evaluated from the diffracted field. The figure of merit can be defined in different ways depending on the particular application for which the polychromat is designed. Details on defining the figure of merit are described in the later chapters. Once the initial FOM is calculated, the algorithm selects one pixel at a time and perturbs the initial height of that pixel by Δh. Then the FOM is evaluated for the updated height. If the new FOM is higher than the original one, the perturbation is accepted. Otherwise the height of the pixel is returned to its original value. In this manner every pixel of the polychromat is perturbed and a loop is completed. This process continues until none of the perturbation of the pixels results in improved FOM. The process can also terminate

when the improvement in the FOM is less than a defined tolerance value. The end result is the optimized height profile of the polychromat.

The diffractive optics can be fabricated using direct laser write grayscale lithography [19, 20]. For this purpose, µpg 101 pattern generator tool [21] (available at Utah Nanofabrication facility) has been used. In direct laser write grayscale photolithography, intensity of laser beam is modulated as it is scanned across the surface of a photoresist. As a result, multilevel structures can be achieved following development. The steps of grayscale are following: a) calibration, b) conversion of design file into a grayscale map, and c) fabrication of final device. The goal of calibration is to make a correlation between a particular intensity of the laser and corresponding exposed depth. For this purpose, first a positive photoresist is spin coated on a glass substrate and baked on a hotplate or in an oven. Next, a calibration design file is written using the µpg 101 tool and developed after exposure. The calibration file is essentially a bmp file which consists of lines with graylevels ranging varying from 1 to 100. During exposure the laser intensity increases with increasing value of graylevels which leads to larger exposed depths. Exposed depth corresponding to a particular graylevel can be known after the calibration. The height profile of a particular polychromat can then be converted into a grayscale map using the calibration data. This grayscale map is used to write the final device using the same process conditions used for calibration. Details on the exact process parameters can be found in each chapter.

1.3 Outlines

Chapter 1 briefly describes the concept of diffractive optics. A background of broadband diffractive optics is presented. This is followed by a short description of a new type of broadband diffractive micro-optic (polychromat). A brief description on the design and fabrication process of the polychromat device is presented. This polychromat is demonstrated for different broadband applications throughout the rest of the dissertation.

Chapter 2 provides the application of the polychromat as a solar spectrum splitter and concentrator. The polychromat separates the incident spectrum into three spectral bands and concentrates these bands onto three different photovoltaic cells. This leads to an increase in the peak output power density of the cells by 43.63%, 30.84% and 30.86%, respectively, when compared to normal operation without the polychromat. Details on the design, fabrication and characterization of this polychromat-photovoltaic system are provided in this chapter.

The polychromat described in Chapter 2 was designed for and experimented with artificial light. Chapter 3 describes a polychromat-photovoltaic system designed for standard solar spectrum (AM1.5). Outdoor measurements of this system along with the design and fabrication process are discussed. Effect of alignment error, spectral variation and solar cell degradation on the polychromat performance are also provided in details.

The polychromat can be designed to function as a chromatic aberration corrected cylindrical lens. Utilizing the enormous degrees of freedoms, the polychromat can be optimized to correct the chromatic aberration over the entire visible spectrum. A detailed description of this work is given in Chapter 4.

Imaging over the entire visible and near IR spectrum using the polychromat is

discussed in Chapter 5. In this case, the polychromat acts as an ultrathin flat lens.

Chapter 6 describes the application of polychromat as a color splitter in liquid crystal displays (LCDs). In standard color LCDs, absorptive color filter reduces the efficiency because the color filter absorbs one third of the incident light. In this chapter, a polychromat based color splitting system is demonstrated. The polychromat separates the incident light into three colors thereby increasing the transmission efficiency significantly. An increase of 19% in transmission efficiency is experimentally demonstrated with a standard LCD for a white screen without any decrease in color gamut.

Chapter 7 details the application of polychromat as a broadband, on-axis transmission holograms. When designed properly, the polychromat can project full color images invariant to viewing angle. Absolute transmission efficiencies of >86% across the visible spectrum from 405nm to 633nm (peak value of about 92%) are experimentally demonstrated.

The dissertation concludes in Chapter 8 with a summary of this work and future research directions.

.
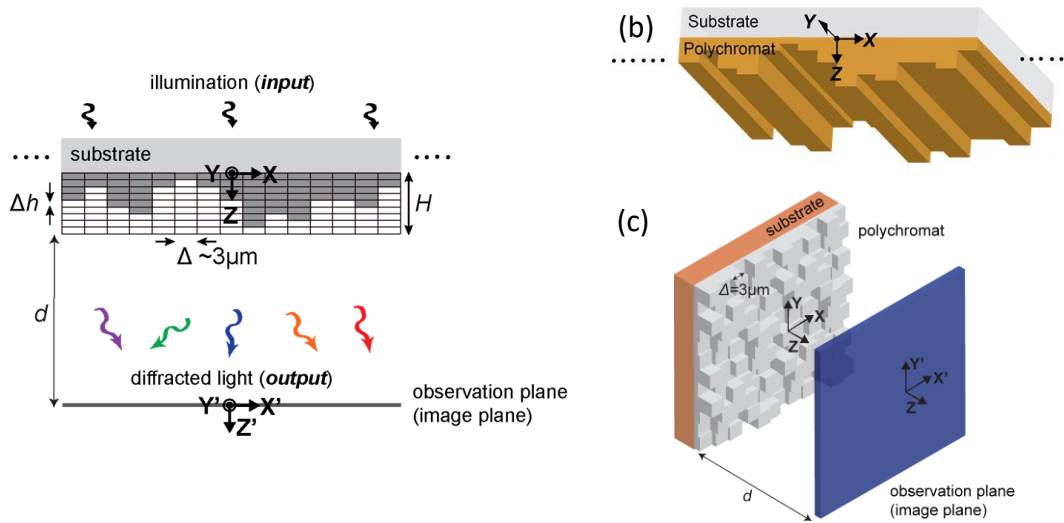
Figure 1.1. Polychromat structure. (a) Schematic representation of the polychromat. The polychromat is a pixelated structure with heights varying from 0 to a maximum height of H in a step height of Δh. The microstructures diffract the incident light, and a diffraction pattern is observed at the image plane. Polychromat in (b) 1D and (c) 2D form. For 1D case, the polychromat is pixelated in one direction and uniform in the other direction while in 2D the pixels are squares. (Image courtesy of Peng Wang)
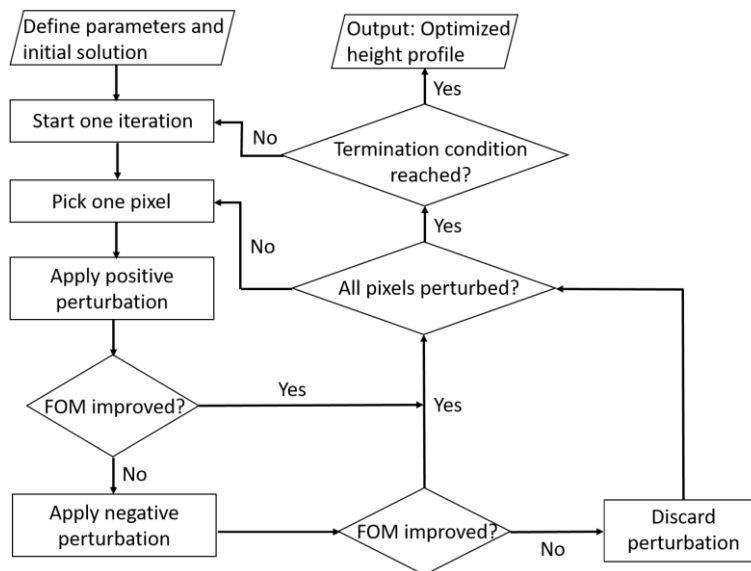
Figure 1.2. Optimization algorithm for designing the polychromat.

1.4 References

[1] G. Elert, *The Electromagnetic Spectrum, The Physics Hypertextbook* (Hypertextbook.com, 1998).

[2] B. E. Saleh, M. C. Teich, and B. E. Saleh, *Fundamentals of Photonics* (New York: Wiley, 1991).

[3] H. Zappe, *Fundamentals of Micro-optics* (Cambridge University Press, 2010).

[4] B. Kress, and P. Meyrueis, *Digital Diffractive Optics: An Introduction to Planar Diffractive Optics and Related Technology* (Wiley-VCH, 2000)

[5] D. C. O'Shea, *Diffractive Optics: Design, Fabrication, and Test* (Spie Press, 2004).

[6] R. Menon, A. Patel, D. Gil, and H. I. Smith, "Maskless lithography," Mater. Today **8**, 26-33 (2005).

[7] H-Y. Tsai, H. I. Smith, and R. Menon, "Reduction of focal-spot size using dichromats in absorbance modulation," Opt. Lett. **33**, 2916-2918 (2008).

[8] X. Wan, B. Shen, and R. Menon, "Diffractive lens design for optimized focusing," J. Opt. Soc. Am. A **31**, B27-B33 (2014).

[9] N. Davidson, A. A. Friesem, and E. Hasman, "Analytic design of hybrid diffractive-refractive achromats," Appl. Opt. 32, 4770-4774 (1993).

[10] A. Flores, M. R. Wang, and J. J. Yang, "Achromatic hybrid refractive-diffractive lens with extended depth of focus," Appl. Opt. **43**, 5618-5630 (2004).

[11] P. Valley, N. Savidis, J. Schwiegerling, M. R. Dodge, G. Peyman, and N. Peyghambarian, "Adjustable hybrid diffractive/refractive achromatic lens," Opt. Express **19**, 7468-7479 (2011).

[12] D. W. Sweeney, and G. E. Sommargren, "Harmonic diffractive lenses," Appl. Opt. **34**, 2469–2475 (1995).

[13] S. Noach, A. Lewis, Y. Arieli, and N. Eisenberg, "Integrated diffractive andrefractive elements for spectrum shaping," Appl. Opt. **35**, 3635–3639 (1996).

[14] T. R. M. Sales, and D. H. Raguin, "Multiwavelength operation with thin diffractive elements," Appl. Opt. **38**, 3012–3018 (1999).

[15] G. Kim, J. A. Dominguez-Caballero, and R. Menon, "Design and analysis of multi-wavelength diffractive optics," Opt. Express **20**, 2814-2823 (2012).

[16] P. Wang, and R. Menon, "Optical microlithography on oblique and multiplane surfaces using diffractive phase masks," J. Micro/Nanolith. MEMS MOEMS **14**, 02350796 (2015).

[17] P. Wang, and R. Menon, "Computational spectrometer based on a broadband diffractive optic," Opt. Express **22**, 14575-14587 (2014).

[18] J. W. Goodman, *Introduction to Fourier Optics* (Roberts and Company Publishers, 2005).

[19] N. Kaste, A. Filbert, U. Mescheder, T. Rang, and G. Rang, "Process development for 3D laser lithography," WIT Trans. Built. Env. **137**, 139-150.

[20] L. Mosher, C. M. Waits, B. Morgan, and R. Ghodssi, "Double-exposure grayscale photolithography," J. Microelectromech. S., **18**, 308-315.

[21] http://www.himt.de/index.php/upg-101.html

CHAPTER 2

ENHANCING PHOTOVOLTAIC OUTPUT POWER USING A

DIFFRACTIVE MICRO-OPTIC

This chapter is adapted with permission from the author's previous publication: N. Mohammad, P. Wang, D. J. Friedman, and R. Menon, "Enhancing photovoltaic output power by 3-band spectrum-splitting and concentration using a diffractive micro-optic," Optics Express **22**, A1519-A1525 (2014).

2.1 Abstract

We report the enhancement of photovoltaic output power by separating the incident spectrum into three bands, and concentrating these bands onto three different photovoltaic cells. The spectrum-splitting and concentration is achieved via a thin, planar micro-optical element that demonstrates high optical efficiency over the entire spectrum of interest. The optic (which we call a polychromat) was designed using a modified version of the direct-binary-search algorithm. The polychromat was fabricated using grayscale lithography. Rigorous optical characterization demonstrates excellent agreement with simulation results. Electrical characterization of the solar cells made from GaInP, GaAs and Si indicate increase in the peak output power density of 43.63%, 30.84% and 30.86%, respectively, when compared to normal operation without the polychromat. This represents an overall increase of 35.52% in output power density. The potential for cost-effective large-area manufacturing and for high system efficiencies makes our approach a strong candidate for low cost solar power.

2.2 Introduction

A single bandgap solar cell suffers from poor efficiency due to its inability to convert photons of all energy into charge carriers. This limitation results from two phenomena: nonabsorption and thermalization [1]. In the former case photons having energy less than the bandgap are not absorbed at all, while those having higher energy than the bandgap lose the excess energy by dissipating heat rapidly within the semiconductor. This limitation can be overcome by utilizing solar cells with different bandgaps and illuminating them with appropriate spectral bands. This demands an efficient method of

spectrum splitting. Various spectrum-splitting strategies have been proposed in literature. A detailed review on spectrum-splitting methods for solar applications has been presented in [2]. Recent advances in spectrum-splitting based efficiency improvement in photovoltaics have been discussed in [3].

Spectrum splitting techniques are usually based on refraction, interference or diffraction. One simple example of refraction-based splitting is the use of a prism [2]. A prism refracts the incident light into several bands. This spectrally dispersed light can then be directed onto absorbers with matching band-gaps. Dichroic mirrors [4] and conventional gratings facilitate spectrum splitting via interference and diffraction, respectively. Other examples of spectrum splitting are the use of a holographic solar concentrator [5] and thin-film interference filters [2,6]. Holographic solar concentrators can choose the useful bands of incident sunlight selectively and concentrate them simultaneously. In interference optical filters multiple thin layers of dielectric materials with high refractive index contrast are deposited on a transparent substrate to achieve the properties of band-stop, band pass or edge filters [2,6]. Although these approaches offer spectrum splitting and have potential to be incorporated into photovoltaic systems, they suffer from multiple drawbacks. One major disadvantage is the associated increase in cost. Other drawbacks are the inability to scale to large areas, low wavelength-averaged optical efficiencies, and poor control of the position, number and size of the spectral bands.

To overcome these limitations, we introduced broadband diffractive optics for spectrum splitting and concentration [7,8]. We refer to this diffractive optic as a "polychromat". Previously, we used the polychromat to increase the peak output power from two single-junction photovoltaic cells using 2-band spectrum splitting and

concentration [8,9]. Here, we report the extension of this approach to three bands and a consequent increase in system power of 35.5%.

2.3 Working Principle

The working principle of the polychromat can be understood from the configuration illustrated in Figure 2.1(a). For simplicity, we utilize 1D polychromat, *i.e.*, the polychromat is pixelated along the X direction and uniform along the Y direction. There are 5001 pixels along the X direction and each pixel is 3 µm wide. The height of each pixel is an integer multiple of 23.81 nm, varying from 0 to a maximum height of 1.5 µm spanning 64 discrete height levels. The polychromat diffracts the incident light in such a way that low, medium and high energy spectral bands of light are concentrated on the left, center and right portions of the image plane, respectively. Each spectral band thus occupies one third of the space in the image plane, resulting in a concentration factor of 3X for each band. GaInP, GaAs and Si single junction solar cells were used to absorb these three different bands at the image plane. These solar cells were first chosen due to their availability and the polychromat was designed to accommodate them.

The dimensions of the GaInP and the GaAs cells are 5mm×5mm while that of the Si cell is 5mm×20mm. In order to ensure that all three cells were fully illuminated, the polychromat was designed to be 15mm×20mm. In addition, this polychromat unit cell was repeated three times along the X direction to account for the periodic boundary conditions used during design [8,9]. As a result, the final device covers an area of 45mm×20mm. The distance between the polychromat and the image plane was chosen to ensure that the shortest wavelength can be diffracted into the appropriate solar cell and this was set to

20cm. Note that this distance can be readily made smaller (to a few mm) when the pixel width is scaled to ~1µm or smaller [9]. The height distribution of the polychromat was determined by applying a modified version of the direct-binary-search algorithm to a rigorous optoelectronic model [9]. The optimization algorithm aims to maximize the power boost, defined as:

$$PowerBoost = \left(\sum_{i=1}^{n} P_{poly,i} - \sum_{i=1}^{n} P_{ref,i} \right) / \sum_{i=1}^{n} P_{ref,i} \quad (2.1)$$

In Equation (2.1), n is the number of solar cells (or spectral bands), $P_{poly,i}$ and $P_{ref,i}$ are the peak output power densities of the ith cell with and without the polychromat, respectively. The final pixel-height distribution is shown in Figure 2.1(b). A magnified view of the left-most 100 µm of the polychromat shown in Figure 2.1(c) reveals the multiple pixel heights.

2.4 Fabrication of Micro-optic

The polychromat was patterned in photoresist atop a glass substrate via grayscale laser lithography. The laser power at each pixel location was adjusted such that the appropriate pixel height is obtained after exposure and development. Details of this procedure and the associated calibration experiments are the same those described in ref [9]. An optical micrograph of the fabricated polychromat is shown in Figure 2.2(a).

2.5 Optical Characterization

We first measured the spatial-spectral point-spread function, *i.e.*, the intensity distribution along X in the image plane as a function of wavelength. The output of a supercontinuum source (NKT Photonics) was collimated and illuminated the polychromat at normal incidence. The fiber input to a spectrometer (Ocean Optics Jazz) was scanned along the X-axis in the image plane. We also simulated the spatial-spectral point-spread function using scalar diffraction theory [7,8] as shown in Figure 2.2(b). The measured data plotted in Figure 2.2(c) agree very well with the simulation. We also calculated the optical efficiency as a function of wavelength, where the optical efficiency is defined as the ratio of power incident within the correct spectral band to the total incident power. The measured optical efficiency is shown as solid lines in Figure 2.2(d) and agrees well with the simulated optical efficiency, shown as dashed lines. Discrepancies in these plots are attributed to fabrication errors as described later. Note that the colors represent the three spectral bands (see Figure 2.1(a)).

Generally, better optical efficiency can potentially be achieved by shrinking the polychromat pixel width, increasing the maximum pixel height, augmenting the number of quantized pixel height levels, including more pixels in the polychromat design and increasing the gap between the polychromat and the solar cells [7]. Highly dispersive material can also increase the optical efficiency [9].

2.6 Electrical Characterization

For electrical characterization, the three solar cells were placed at appropriate locations in the image plane one at a time. Current density and power density were

measured for each device at different bias voltages with and without the polychromat. In order to normalize Fresnel reflections from the glass as well as residual light absorption within the photoresist, the reference measurements were taken with a glass substrate and unpatterned resist with the same thickness above the solar cells. Note that the beam was expanded to a diameter of ~45mm before illuminating the polychromat, and the beam size was maintained the same for measurements both with and without the polychromat. The resulting plots are shown in Figure 2.3. The blue and red curves correspond to the reference and the polychromat measurements, respectively. It is noted that the overall power densities are quite low due to the low illumination intensity, which was measured as 3.4mW/cm^2. This was limited by the power output from our supercontinuum source. Nevertheless, all the solar cells demonstrate an improvement in performance with the polychromat. The short-circuit current-density (j_{sc}) of the GaInP, GaAs and Si cells are increased by 43.33%, 32.52% and 27.29%, respectively. This can be attributed primarily to the concentration. The open-circuit voltages (v_{oc}) are increased by 5.77%, 1.3% and 10%, respectively. As a result, the peak output power-densities are increased by 43.63%, 30.84% and 30.86%, respectively. The combined power-density from all three cells resulted in an increase of 35.52% when compared to the case without spectrum-splitting and concentration.

These improvements can be explained with the help of the external quantum efficiency (EQE) plots of the three cells shown in Figure 2.4(a). For the GaInP cell, any light of wavelength > 700nm is not absorbed. Although wavelengths < 700nm are absorbed within GaAs and Si, these photons produce current at a lower voltage than their intrinsic energy should allow. This is due to the thermalization loss. Therefore, by allocating those

photons to the GaInP, one is able to minimize this loss. Similar arguments can be made for the GaAs cell as well. The overall effect is that the concentration of the appropriate spectral band by a factor of 3 results in an increase in the j_{sc} and a smaller increase in the v_{oc}. Minimization of the thermalization losses due to the appropriate spatial allocation of the photons also contributes to the increases in voc. Note that the best possible cells for spectrum-splitting exhibit nonoverlapping EQE spectra. In such a case, where we can optimize the EQE by appropriate materials growth, the expected improvement can be quite large and can be comparable to the best multijunction devices [10].

Note that the aforementioned improvement is based upon comparison to a reference of three solar cells of the same dimension without the polychromat. However, the total power density measured with the polychromat is lower than the case where the entire illumination aperture is filled with the best cell (GaAs here) without the polychromat. Our simulations confirm that this is primarily due to the poor performance of the specific Si solar cell that we used. It is clear from Figure 2.3(e) that the j_{sc} of the Si cell falls far below those of GaInP and GaAs. In addition, the v_{oc} is also smaller than commercial cells under AM1.5 illumination partially because of the limited photon flux of our illumination. According to the J-V curve, the Si cell also suffers from reduced fill factor. On the other hand, if we assume ideal solar cells with the external quantum efficiencies shown in Figure 2.4(a), our calculations indicate that this polychromat should enable an overall power density that is more than 3 times that produced by the best single-bandgap device of the same size as the polychromat aperture. Additionally, improving the optical efficiency (see Figure 2.2(d)) by minimizing fabrication errors, discussed in the following section, is also able to increase the total power density output of the presented scheme.

2.7 Error Analysis

Simulations predicted an increase of 61.79%, 70.55% and 39.79% in output power densities of GaInP, GaAs and Si solar cells, respectively. The predicted increase in combined power density is 55.04%. The discrepancies between simulated and measured results are primarily due to fabrication errors. The pixel-height distribution of the fabricated polychromat does not perfectly match with the design heights primarily due to laser-intensity variations during the grayscale lithography and calibration processes. We illustrate this effect by plotting the designed and measured pixel-heights for a 160 µm-long segment of the polychromat in Figure 2.4(b). By doing similar measurements over two more randomly selected segments, we estimated the pixel-height error to correspond to a standard deviation of 142nm.

To gain insight into the effect of pixel-height errors on the device performance, we performed a statistical simulation. First, height errors were randomly selected from a normal distribution of zero mean and given standard deviation. Then, we applied our optoelectronic model to calculate the resulting increase in the output power-density, what we refer to as the power boost (see Equation (2.1)). The power boost for each cell and the combined device (for all three cells) as a function of the standard deviation of the error distribution are shown in Figure 2.5(a). It may be noted that for a standard deviation of 150nm (equivalent to the observed fabrication error), the combined power boost is ~33%, close to the measured value of 35.5%. The corresponding impact on the optical efficiency is plotted in Figure 2.5(b). The curves (dot-dashed lines) corresponding to the standard deviation of 150nm is comparable to the experimentally obtained curves in Figure 2.2(d) (solid lines). From this analysis, we conclude that most of the discrepancy between the

measured and the simulated power boost of 35.5% and 55%, respectively, is due to pixel-height errors during fabrication. Our current effort is focused on reducing this error via optimization of the fabrication process.

Defocus or variation in the distance between the polychromat and the image plane can also affect performance. To investigate this effect, we simulated the power boost and the optical efficiencies at defocus distances from -50mm to 50mm centered on the designed focus of 20cm. As shown in Figure 2.5(c), for positive defocus, *i.e.*, as the image plane moves closer to the polychromat, the power boost of GaInP increases while that of Si decreases. This may be understood by appealing to the optical efficiency plots in Figure 2.5(d). The optical efficiency plots exhibit red-shift and blue-shift due to positive and negative defocus, respectively. The red-shift allows GaInP to absorb more photons. Also, for negative defocus, the blue shift allows more high energy photons to reach the Si cell increasing its power boost at the expense of the GaInP cell. The power boost of the GaAs cell decreases for both positive and negative defocus. As expected, the combined power boost is maximum at focus (zero defocus). Nevertheless, the depth-of-focus of this system defined as the defocus corresponding to a decrease in combined power boost of 20% is ~5mm. Note that this is consistent with the low numerical aperture of the polychromat (NA~0.06).

2.8 Conclusions

Achieving high efficiency in a cost-effective manner is very challenging in photovoltaics. In this work, we describe progress towards this goal by utilizing a planar micro-optical element (polychromat) to spectrally split and concentrate sunlight onto three

distinct solar cells, and measured an increase in output power of 35.5%. The polychromat

can be inexpensively manufactured via high-volume stamping techniques [11,12]. The

flexibility afforded by our approach can enable hybrid devices that combine multiple

spectral bands and different concentration factors to achieve the best possible efficiency to

cost ratios [9].

2.9 Supplementary Information

To understand the design principle of the polychromat, let us consider the

diffractive optical element (DOE) illustrated in Figure 2.6(a). The DOE is 1D, *i.e.*,

pixelated along the X direction with (M+1) pixels and uniform along the Y direction. Each

pixel has a width of Δx and the height is multiple of a step height Δh. The DOE's height

profile is given by:

$$h(\mathrm{x}) = \sum_m \Delta h p_m rect(\frac{x - m\Delta_x}{\Delta_x}) \quad (2.2)$$

In Equation (2.2), $\Delta h = H/N$, H is the maximum height, N is the number of levels;

$p_m \in [0,N] \cap Z$; rect() is the rectangle function; $m \in [-M/2, M/2]$ is the pixel index. The

transmission function of such DOE can be expressed as [8]:

$$T(\mathrm{x}; \lambda) = e^{i\varphi(\mathrm{x};\lambda)} = 1 + \sum_m rect(\frac{x - m\Delta_x}{\Delta_x})(e^{ia(\lambda)p_m} - 1) \quad (2.3)$$

Here, $a(\lambda) = k\Delta h(n(\lambda)-1)$, $n(\lambda)$ is the refractive index of the DOE material and $k = 2\pi/\lambda$

is the wave number. When a plane wave is normally incident upon the DOE, the diffracted field at the reconstruction plane for a particular wavelength λ is given by the Fresnel transformation [8]:

$$U(\mathrm{x}';\lambda) = \frac{e^{ikd}}{i\lambda d} \int g_{illum}(\mathrm{x};\lambda)\,\mathrm{T}(\mathrm{x};\lambda)\,e^{i\frac{k}{2d}(\mathrm{x}'-\mathrm{x})^2}\,\mathrm{dx} \quad (2.4)$$

In Equation (2.4), d is the distance between the DOE and the reconstruction plane (see Figure 2.6(b)) and $g_{illum}(\mathrm{x};\lambda)$ is the power spectrum of the incident light.

In case of the polychromat, M=5000, Δx=3um, H=1.5um, N=64, d=200mm. Minimum value of Δx and maximum values of H and N are constrained by the fabrication process. A super-continuum source (NKT Photonics) was used as the input light spectrum. Power spectra of this source is illustrated in Figure 2.6(c). Shipley 1813 photoresist was chosen as the polychromat material. Woollman Ellipsometer was used to measure the dispersion data of the photoresist. This is shown in Figure 2.6(d). As mentioned in the main article, the height profile of the optic was optimized by maximizing the figure of merit (FOM), defined in Equation (2.1), by means of a modified version of the direct binary search algorithm [2]. In this algorithm, an initial height profile is chosen at the beginning. As the convergence of the solution is sensitive to initial condition, it is chosen carefully. Details on choosing the initial condition have been presented in [8]. Based on the initial condition, the diffracted field is calculated with the aid of Equation (2.4). This is followed by calculating the short circuit current densities defined as [9]:

$$J_{sc,poly}^{cell,i} = \iint \frac{q\lambda}{hc} I_{poly}(\text{x},\lambda) EQE^{cell,i}(\lambda) dx d\lambda \quad (2.5)$$

$$J_{sc,ref}^{cell,i} = \iint \frac{q\lambda}{hc} I_{ref}(\text{x},\lambda) EQE^{cell,i}(\lambda) dx d\lambda \quad (2.6)$$

In Equation (2.5), $I_{poly}(x,\lambda)$ is the light intensity at point X of the image plane for wavelength λ in the case where the diffracted field is calculated at the presence of polychromat; $I_{ref}(x,\lambda)$ in Equation (2.6) is the reference intensity distribution, *i.e.*, when the array of the solar cells is illuminated directly, *i.e.*, the power spectrum of the source; cell,i is ith solar cell, specifically cell1, cell2 and cell3 represent GaInP, GaAs and Si solar cells, respectively; $EQE^{cell,i}$ is the external quantum efficiency of the ith solar cell; thus $J_{sc,,ref}$ and $J_{sc,poly}$ are the short circuit current densities when the solar cells are illuminated with and without the polychromat, respectively. From the short-circuit current densities, corresponding power densities are calculated as follows:

$$P_{poly,i} = J_{sc,poly}^{cell,i} V_{oc}^{cell,i} FF^{cell,i} \quad (2.7)$$

$$P_{ref,i} = J_{sc,ref}^{cell,i} V_{oc}^{cell,i} FF^{cell,i} \quad (2.8)$$

In Equations (2.7) and (2.8), V_{oc} and FF stand for open circuit voltage and fill factor, respectively. To calculate the open circuit voltage, the I-V characteristics of each cell was measured first under direct illumination from the source. The measured open circuit voltage was then scaled to obtain the value for simulation using the following equations:

$$V_{oc}^{cell,i} = \frac{n_i KT}{q} \ln\left(\frac{J_{sc,ref}^{cell,i}}{J_{sc,meas}^{cell,i}}\right) \quad (2.9)$$

Ideally, $J_{sc,,ref}$ and $J_{sc,meas}$ should be same. However, there is slight difference in the values of these two currents. One reason for the discrepancy can be attributed to the lower irradiance value of the light incident on the cells compared to the values used in the simulation. This is due to the fact that light is propagated over a long distance before illuminating the cells to ensure collimated input. Series and shunt resistance of the cells further lower the short circuit current density and open circuit voltage. Fill factor was also calculated from the measured I-V characteristics. Although spectrum splitting changes the open circuit voltage and fill factor slightly, this was neglected in the simulation and the same value was used in both Equations (2.7) and (2.8) for both parameters.

Thus figure of merit (FOM) is calculated for the initial height distribution utilizing Equations (2.3)-(2.9) and Equation (2.1). Once the initial FOM is calculated, the algorithm selects one pixel at a time and perturbs the initial height of that pixel by Δh. Then the FOM is evaluated for the updated height. If the new FOM is higher than the original one, the perturbation is accepted. Otherwise the height of the pixel is returned to its original value. In this manner every pixel of the polychromat is perturbed and a loop is completed. This process continues until none of the perturbation of the pixels results in improved FOM. The process can also terminate when the improvement in the FOM is less than a defined tolerance value.

Using this algorithm an optimized design of polychromat was obtained. The resulting improvements in short circuit current densities and peak output power densities are illustrated in Figure 2.7.

The polychromat was fabricated by patterning Shipley 1813 photoresist spin coated on a 3'' square glass substrate. The glass substrate was RCA cleaned first. The photoresist was then spin coated on the glass substrate at a speed of 2000 rpm for 60 seconds. This produced a film of thickness of about 1.6 µm. The sample was then baked in an oven at 110° C for 40 minutes. The photoresist was exposed by the MicroPG 101 pattern generator from Heidelberg Instruments. Before writing the polychromat design, calibration was done on a separate sample prepared in a same manner. Calibration results are shown in Figure 2.8(a). The design shown in Figure 2.8(b) was used for calibration. As the gray levels in the calibration design change from 0 to 99, the laser power incident on the photoresist increases accordingly, resulting in thinner residual film. This calibration was used to translate the polychromat height distribution obtained from simulation to gray scale values in the mask design. The polychromat design (Figure 2.6(c)) was then written on the photoresist with the same dose of the laser used for calibration. Finally, the sample was developed in 352 developer for 1 minute and a multilevel structure was left on the photoresist. The fabrication process flow is illustrated in Figure 2.8(d). To investigate the fabrication error, three segments, each consisting of 50 pixels, were chosen at three different locations along the X direction of the polychromat. Height of each pixel was measured using Tencor Profilometer. The error was calculated by subtracting the measured heights from the design heights. The mean of the error was ~10nm and the standard deviation was ~141nm.

The polychromat was optically characterized by measuring its spatial-spectral intensity distribution at the image plane. The spatial-spectral intensity distribution is defined as [9]:

$$S(\text{x}, \lambda) = \frac{I_{poly}(\text{x}, \lambda) - I_{dark}(\text{x}, \lambda)}{I_{ref}(\text{x}, \lambda) - I_{dark}(\text{x}, \lambda)} \quad (2.10)$$

In Equation (2.10), $I_{poly(\text{x},\lambda)}$ and $I_{ref(\text{x},\lambda)}$ represent the spatial-spectral intensity distribution at the image plane when the polychromat is illuminated through the patterned and unpatterned photoresist, respectively. This normalization is done due to the non-uniformity of the source spectrum. $I_{dark(\text{x},\lambda)}$ is the measurement at dark and represents any background noise associated with the measurement process. For optical characterization the setup in Figure 2.9 was used. A 109mW super-continuum source (SuperK COMPACT, NKT Photonics) was used for illumination. Light emanating from the source was guided to illuminate the polychromat design on the glass substrate which was mounted in such a way that the surface is perpendicular to the incident beam. A single mode fiber tip was placed at a distance of 200mm and mounted on a motorized stage. The other end of the fiber was connected to Ocean Optics Jaz Spectrometer. The tip was scanned across X direction at the imaging plane with 10 µm step. The measured data were normalized according to Equation (2.10) to generate the spectral-spatial map shown in Figure 2.2(c). The map demonstrates the splitting of the spectrum into three bands. The spectrum splitting can also be observed by placing a white screen at the reconstruction plane.

For electrical characterization, GaInP, GaAs and Si solar cells were used to absorb the three diffracted bands. A glass support was used to hold these cells. The glass support was placed at the same distance (200mm) at which the spatial-spectral map was measured. First the cells were visually aligned to the diffracted bands. Then the stage was moved laterally and I-V characteristics were measured for each cell at each position. The position

that gave the highest peak power was chosen for final measurement. I-V characteristic was measured using Keithley 2602A Source Meter. Figure 2.3 illustrates these measurements. The reference measurement was done in the same manner except the light was guided through the unpatterned region of the photoresist on the substrate instead of the design area.
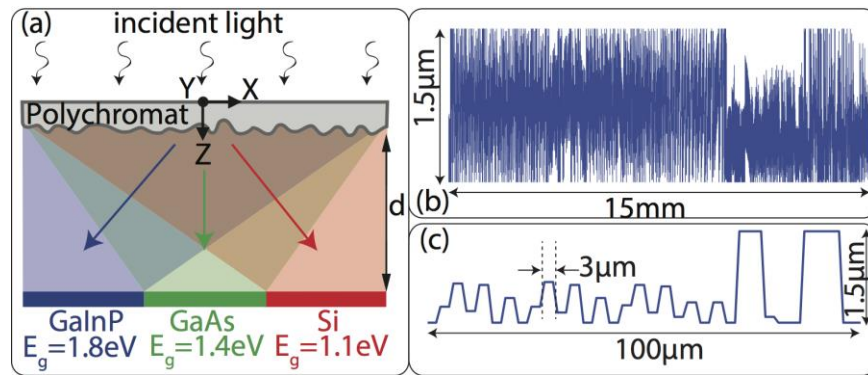
Figure 2.1. Details of the polychromat. (a) Schematic of the polychromat-solar cells configuration. (b) Height distribution of the designed polychromat. (c) Magnified view of the left-most 100 µm of the polychromat.
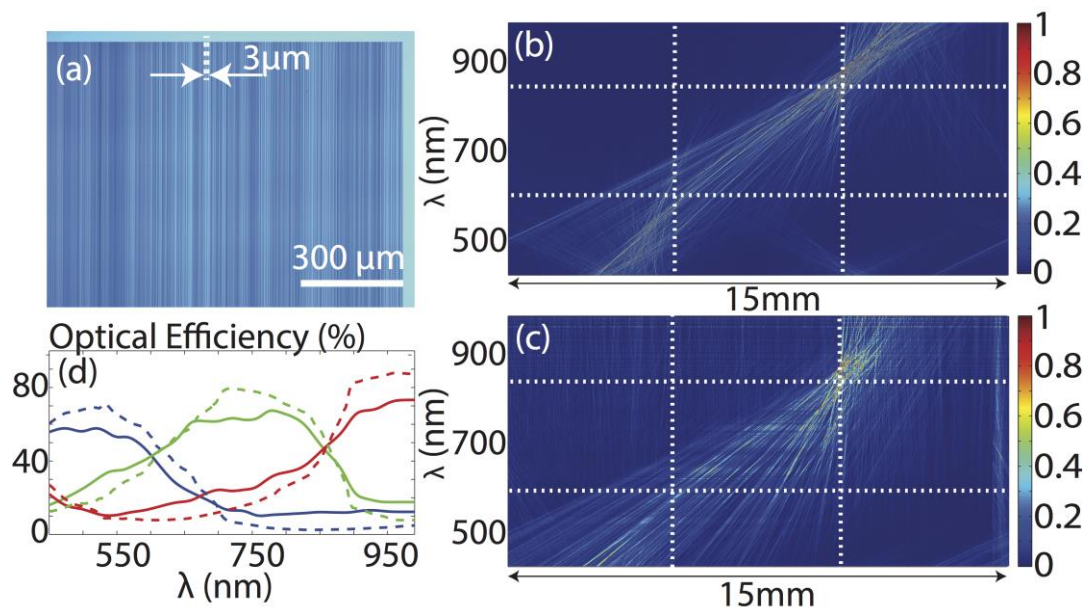
Figure 2.2. Optical characterization. (a) Optical micrograph of the fabricated polychromat. The spatial-spectral point-spread function of the polychromat: (b) simulated and (c) measured. White lines are shown to depict the boundaries of the 3 bands. (d) Optical efficiency as a function of wavelength: simulated (dashed lines), measured (solid lines).
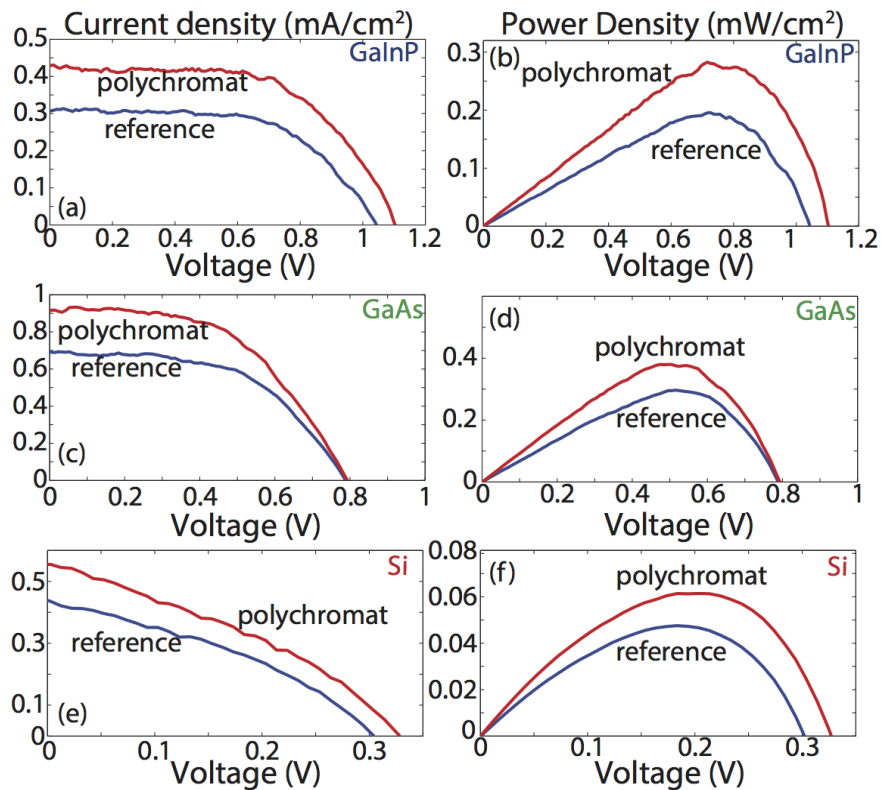
Figure 2.3. Electrical characterization. Current density vs voltage for (a) GaInP (c) GaAs and (e) Si cells. Power density vs voltage for (b) GaInP (d) GaAs and (f) Si cells. Reference measurements are shown in blue, while spectrum-split measurements are in red.
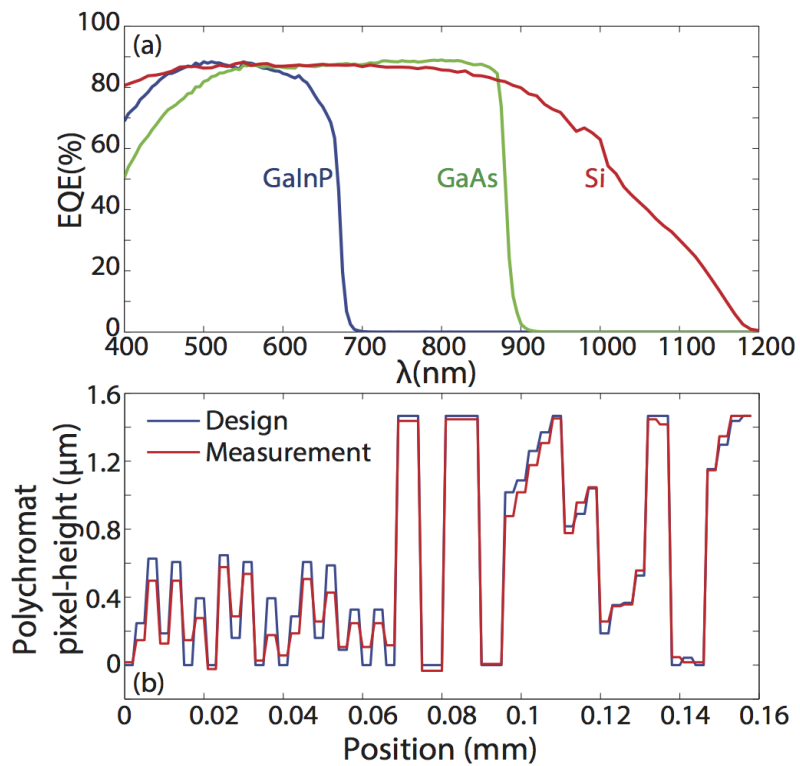
Figure 2.4. Effect of EQE and height errors on the polychromat performance. (a) Quantum efficiencies of GaInP, GaAs and Si cells. (b) Designed (blue) and measured (red) pixel-height distribution along the x direction of the polychromat.
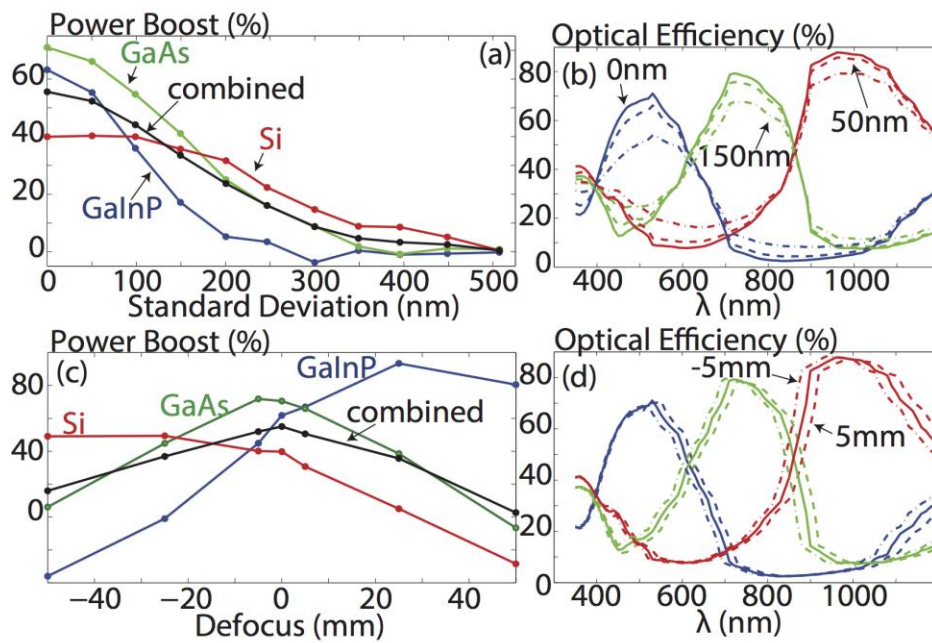
Figure 2.5. Effect of errors. Variation (a) of power boost and (b) of optical efficiencies as a function of standard deviation of the polychromat height errors. Variation (c) of power boost and (d) of optical efficiencies as a function of defocus error.
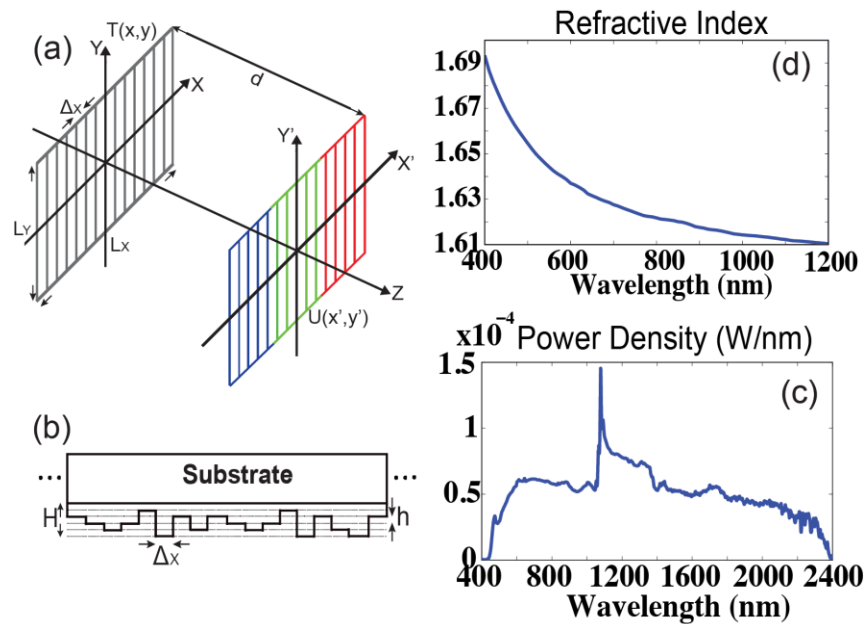
Figure 2.6. Design principle of the diffractive optical element (polychromat). (a) Spectrum-splitting model in the Fresnel domain (gray grids for the micro-optic; blue, green and red for GaInP, GaAs and Si cells, respectively). (b) Schematic representation of the polychromat (cross-section in the X-Y plane). (c) Measured refractive index as a function of wavelength. (d) Power spectra of the supercontinuum source used in optical and electrical characterization.
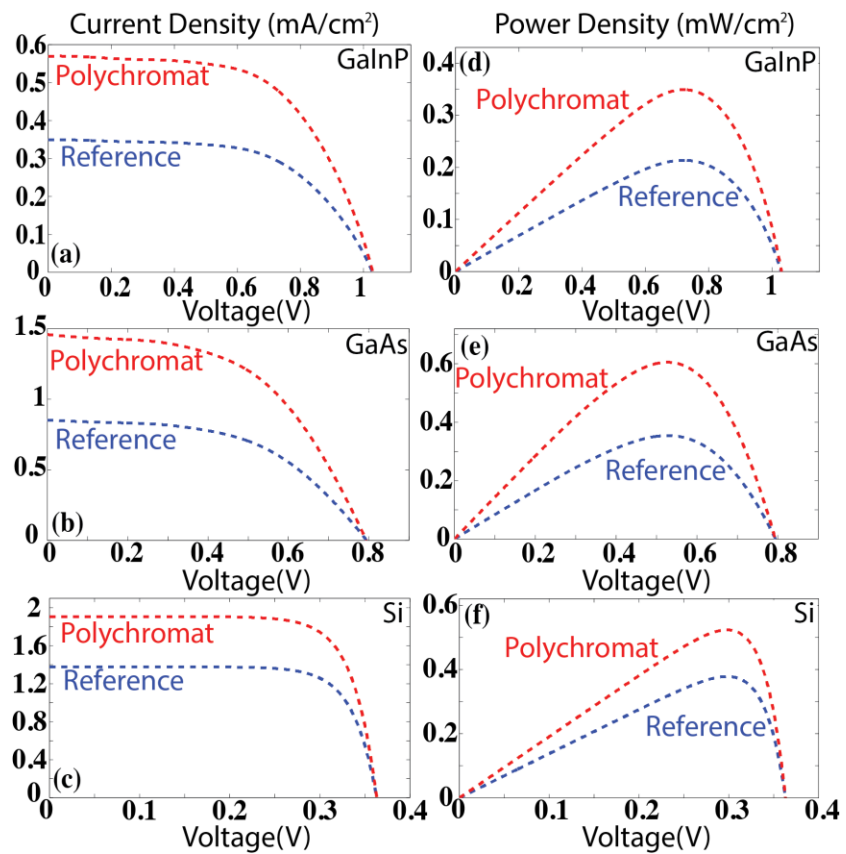
Figure 2.7. Simulation results. Current density vs. voltage for (a) GaInP (b) GaAs and (c) Si cells. Power density vs. voltage for (d) GaInP (e) GaAs and (f) Si cells. Reference results are shown in blue, while spectrum-split results are in red.
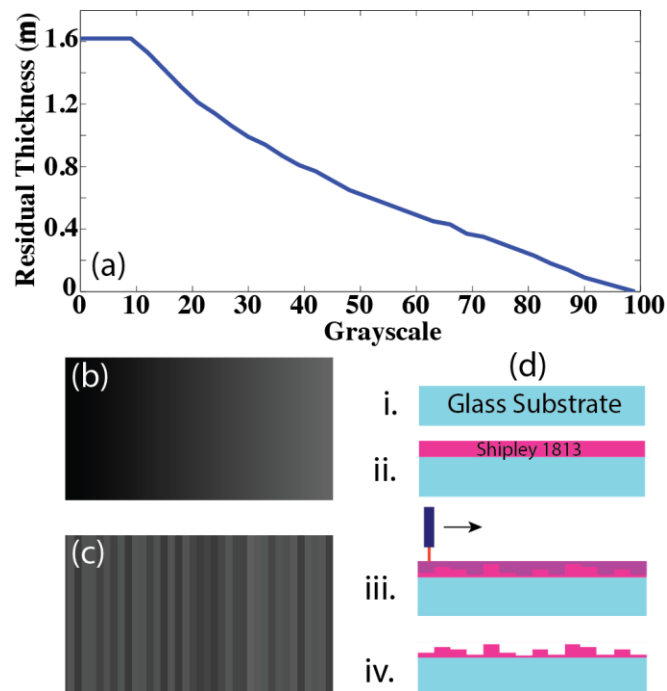
Figure 2.8. Fabrication of the polychromat. (a) Calibration measurements: residual thickness of the photoresist as a function of grayscale. (b) Design file for calibration. (c) A small segment of the polychromat design file. (d) Fabrication process flow: (i) RCA cleaned glass substrate, (ii) spin coating of Shipley 1813, (iii) exposing the photoresist using MicroPG 101 (laser power is modulated according to the gray levels in the design) and (iv) multilevel structure following development.
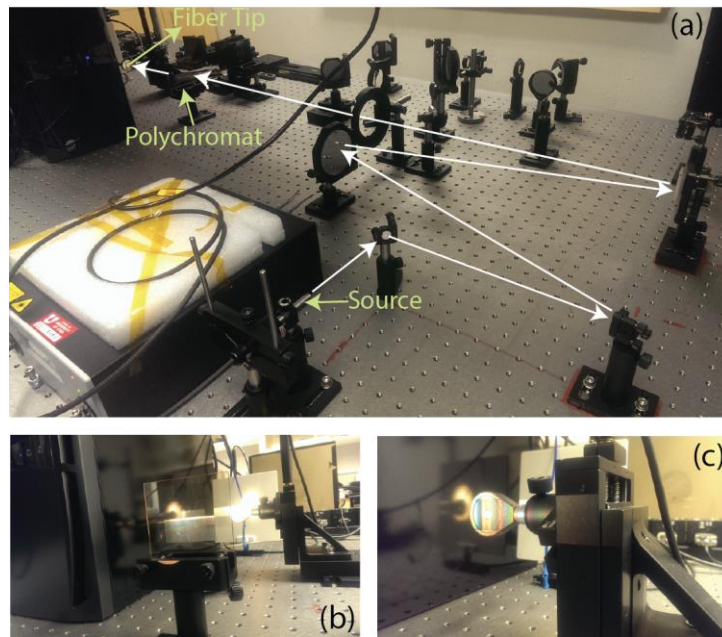
Figure 2.9. Experimental setup for optical and electrical characterization. (a) Optical setup for guiding light from source to the polychromat (Light path is showed by white arrows). (b) Polychromat mounted on a holder. (c) Fiber tip mounted on a motorized step.

2.10 References

[1] A. Polman, and H.A. Atwater, "Photonic design principles for ultrahigh-efficiency photovoltaics," Nat. Mater. **11**, 174-177 (2012).

[2] A. G. Imenes, and D. R. Mills, "Spectral beam splitting technology for increased conversion efficiency in solar concentrating systems: a review," Sol. Energ. Mater. Sol. C. **84**, 19-69 (2004).

[3] A. Mojiri, R. Taylor, E. Thomsen, and G. Rosengarten, "Spectral beam splitting for efficient conversion of solar energy—A review," Renew. Sust. Energ. Rev. **28**, 654-663 (2013).

[4] B. Mitchell, G. Peharz, G. Siefer, M. Peters, T. Gandy, J. C. Goldschmidt, J. Benick, S. W. Glunz, A. W. Bett, and F. Dimroth, "Four-junction spectral beam-splitting photovoltaic receiver with high optical efficiency," Prog. Photovolt: Res. Appl. **19**, 61-72 (2011).

[5] R. K. Kostuk, and G. Rosenberg, "Analysis and design of holographic solar concentrators," Proc. SPIE **7043**, 70430I (2008).

[6] H. A. Macleod, *Thin-film Optical Filters* (CRC Press, 2001).

[7] G. Kim, J-A. Domínguez-Caballero, and R. Menon, "Design and analysis of multi-wavelength diffractive optics," Opt. Express **20**, 2814-2823 (2012).

[8] G. Kim, J-A. Dominguez-Caballero, H. Lee, D. J. Friedman, and R. Menon, "Increased photovoltaic power output via diffractive spectrum separation," Phys. Rev. Lett. **110**, 123901 (2013).

[9] P. Wang, J-A. Dominguez-Caballero, D. Friedman, and R. Menon, "A new class of multi-bandgap high efficiency photovoltaics enabled by broadband diffractive optics," Prog. Photovolt: Res. Appl. **23**, 1073-1079.

[10] M. S. Leite, R. L. Woo, J. N. Munday, W. D. Hong, S. Mesropian, D. C. Law, and H. A. Atwater, "Towards an optimized all lattice-matched InAlAs/InGaAsP/InGaAs multijunction solar cell with efficiency >50%," Appl. Phys. Lett. **102**, 033901 (2013).

[11] L. Guo, "Recent progress in nanoimprint technology and its applications," J. Phys. D: Appl. Phys. **37**, R123–R141 (2004).

[12] C. Battaglia, J. Escarre, K. Soderstrom, L. Erni, L. Ding, G. Bugnon, A. Billet, M. Boccard, L. Barraud, S. D. Wolf, F. Haug, M. Despeisse, and C. Ballif, "Nanoimprint lithography for high-efficiency thin-film silicon solar cells," Nano Lett. **11**, 661–665 (2011)

CHAPTER 3

OUTDOOR MEASUREMENTS OF A POLYCHROMAT-

PHOTOVOLTAIC SYSTEM

This chapter is adapted with permission from the author's previous publication: N. Mohammad, M. Schulz, P. Wang, and R. Menon, "Outdoor measurements of a photovoltaic system using diffractive spectrum-splitting and concentration," AIP Advances **6**, 095311 (2016).

3.1 Abstract

In a single-bandgap absorber, photons having energy less than the bandgap are not absorbed, while those having energy larger than the bandgap lose the excess energy via thermalization. We present outdoor measurements of a photovoltaic system that overcomes these losses via spectrum splitting and concentration using a planar diffractive optic. The system was comprised of the diffractive optic coupled with GaInP and CIGS solar cells. The optic provides a geometric concentration of 3X for each solar cell. It is easily fabricated by single-step grayscale lithography and it is ultrathin with a maximum thickness of only 2.5μm. Electrical measurements under direct sunlight demonstrated an increase of ~25% in total output power compared to the reference case without spectrum splitting and concentration. Since different bandgaps are in the same plane, the proposed photovoltaic system successfully circumvents the lattice-matching and current-matching issues in conventional tandem multijunction solar cells. This system is also tolerant to solar spectrum variation and fill-factor degradation of constitutive solar cells.

3.2 Introduction

Despite the wide spectral content of sunlight (with most of the power in the range of ~350 nm to ~2000 nm), efficiency of single-junction solar cells is limited due to thermalization and nonabsorption losses [1,2]. Photons that have energy below the bandgap of the absorber are not absorbed. This is termed as the nonabsorption loss. On the other hand, if the photon energy is higher than the absorber bandgap, the excess energy is lost to heat (referred to as the thermalization loss). According to Polman and Atwater [2], thermalization and nonabsorption account for at least 40% of the drop in efficiency. One

way to overcome these loss mechanisms is to use multijunction solar cells [3-5]. In a traditional multijunction configuration, solar cells of different bandgaps are stacked on top of each other in descending order of bandgaps, *i.e.*, the highest bandgap device on the top and the lowest at the bottom. As a result, light first strikes the highest bandgap device, which absorbs the high-energy photons and the low-energy photons are absorbed in the subsequent low bandgap cells. Multijunction solar cells require lattice-matched growth, which limits the choice of materials. Furthermore, since the subcells are connected in series, performance of the device is limited by the subcell generating the lowest current. Multijunction architecture can also be realized by mechanical stacking, for example, by physical wafer bonding [6,7] or by using organic adhesives [8]. Performance of these devices is constrained by the current-matching requirement. Use of insulating organic adhesive can somewhat mitigate this issue but bring other disadvantages such as poor optical transmission and thermal conduction between the subcells [9].

An alternative is to use spectral-splitting optical elements to split the incident sunlight spatially and to use separate cells with bandgaps matched to the spectral bands [10-11]. This technique allows the independent operation of subcells, and eliminates the lattice-matching and current-matching requirements. Several spectrum-splitting techniques have been presented in the literature for photovoltaic application [12-29]. The most common approach is to use dichroic filters which allow certain bandwidth of incident light to pass while reflecting the rest thus splitting the spectrum into two spectral bands [12-21]. These dichroic mirrors can be arranged in different configurations to achieve spectrum splitting. A photovoltaic (PV) system consisting of two tandem cells (GaInP/GaAs and GaInAsP/GaInAs) and a single junction cell (Si) along with dichroic prism, lens array and

concentrators was described by Barnett et al. [13]. An efficiency of 42.7% was reported for this system considering ideal dichroic splitting optics. Another architecture consisting of dichroic mirrors, lenses and concentrators with two tandem cells (GaInP/GaAs and GaInAsP/GaInAs) achieved 38.5% module efficiency [14]. An efficiency of 34% was demonstrated for a system in which one tandem cell (GaInP/GaAs) and two single junction cells (Si and GaSb) with dichroic filters on top of them were arranged in parallelepiped configuration [15]. Polyhedral specular reflector design was proposed for ultrahigh efficiency modules [16]. In this design, seven subcells can be arranged in a parallelepiped configuration. With moderate concentration, these designs can lead to >50% module efficiency. Holographic elements have also been a popular choice for photovoltaic spectrum splitting [22-25]. Holographic elements can be designed to diffract incident light at particular angle depending on the wavelengths thus in effect achieving spectrum splitting. A PV module consisting of reflection holograms with GaAs and Si cells has been proposed [23]. Overall system efficiency was calculated 27.94% with the holographic filter. Another design consisting of a set of twelve volume holographic gratings with four subcells predicted module efficiency of 37.1% at 672X concentration [24]. Spectrum splitting using prisms has also been implemented [26,27]. In this case, dispersion causes incident lights to bend at different angles leading to spectrum splitting. Polycarbonate based prismatic lens has been demonstrated to simultaneously concentrate and split incident spectrum [26,27].

Spectrum splitting techniques are particularly useful for space photovoltaics [10]. A concentrating-spectrum splitting system for orbital power generation was proposed by Onffroy et al. [28]. The design consisted of several dichroic mirrors to achieve multiple

spectral bands. Michel et al. presented a blazed diffraction grating based spectrum splitting technique for space applications [29]. An important consideration is that the spectrum splitting components need to be simple (preferably planar), compact and lightweight so that they can be transported and assembled easily. Furthermore, the improved performance offered by these additional components should be commensurate with the additional cost. This implies that the components should be inexpensive to manufacture and have high broadband efficiency. These conditions are more stringent when spectrum splitting approaches are to be incorporated in terrestrial applications, since space applications usually allow higher cost compared to terrestrial ones.

As discussed above, the concept of using spectrum splitting optics in photovoltaic system is not novel, and there have been several design proposals and demonstrations in the literature. However, all these approaches suffer from one or more drawbacks causing their incorporation into the photovoltaic systems to be somewhat impractical. For example, dichroic filters are expensive. Furthermore, in order to achieve multiple spectral bands, the solar cells and the dichroic filters need to be arranged in a complex configuration which is undesirable for a PV system. The number of spectral bands are also limited due to the Fresnel reflection losses from multiple surfaces. Holographic diffractive elements offer a relatively cheap solution, but they suffer from low diffraction efficiencies and the specific positions of the spectral bands are challenging to achieve. Multiple holographic elements are required to achieve efficient broadband spectrum splitting. Refraction based spectrum splitting systems suffer from multiple drawbacks such as inability to scale to large areas, low efficiency, lack of controlling spatial position and band edges of spectral bands.

We previously demonstrated a planar, broadband diffractive-optical element

(termed a polychromat) that performs simultaneous spectrum-splitting and concentration [30,31]. We experimentally demonstrated increase in peak power density of 20% and 36% with of two- and three-band spectrum-splitting and concentration, respectively [31,32]. However, these systems were designed for and the experiments were performed with artificial light sources. Here, we present experimental demonstration of a system that achieves two-band spectrum splitting and 3X geometric concentration under the standard AM1.5 spectrum. The solar cells were made of GaInP and CIGS. Our system was assembled and tested under direct sunlight in Salt Lake City, Utah over three separate days in September 2015. We measured an increase of ~25% in the peak power density compared to the case without spectrum-splitting and concentration. As far as we are aware, this is the first demonstration of efficient diffractive spectrum-splitting and concentration under ambient sunlight resulting in an increase in the overall PV power output.

3.3 Design

The geometry of our system is illustrated in Figure 3.1(a). The polychromat diffracts the incident sunlight in such a way that high-energy photons are directed towards the GaInP cell, while the low-energy photons are incident upon the CIGS (labeled C3847) cell. The polychromat also concentrates the light as indicated. The polychromat is pixelated along the X direction and uniform along the Y direction. Thus, spectrum splitting and concentration occur only along the X direction. The width of each pixel is 3µm, while the height varies from 0 to 2.5µm with up to 61 levels in between (Figure 3.1(b)). These values are constrained primarily by the grayscale process used to fabricate the polychromat. The height profile was optimized to maximize the output power of the solar cells. This was

done using a modified version of the direct-binary-search (DBS) algorithm combined with a scalar diffraction formulation and an optoelectronic model [30,31]. DBS is an iterative method and it perturbs the pixels of the polychromat before a metric of overall electrical power output is evaluated. The optimized height profile is shown in Figure 3.1(c). A magnified view of the leftmost 100µm of the polychromat is illustrated in Figure 3.1(d). Details of the design process have been described in our previous works [31,32].

The solar cells were selected due to their optimal bandgaps and availability. GaInP cell has a bandgap of 1.8eV, while the bandgap of C3847 cell is 1.13eV. The measured external quantum efficiencies (EQE) of these cells confirm that the absorption of GaInP cell is mainly in the visible region, while that of C3847 extends into the infrared region. Figure 3.2 shows the measured EQE plots of the solar cells along with the AM1.5 spectrum. The GaInP cell is 5 mm × 5 mm and the C3847 cell is 4.75 mm × 9 mm. The overall size of one period of the polychromat is 14.25 mm × 9 mm. This period is repeated three times during the fabrication to satisfy the periodic-boundary condition assumed during design.

3.4 Fabrication

Grayscale lithography was used to fabricate the polychromat. In this process, a commercially available photoresist, Shipley 1813 was first spin-coated on a 3" × 3" RCA-cleaned glass substrate at 1000 rpm for 60s followed by soft baking in an oven at 110°C for 30 minutes. The optimized design height profile (see Figure 3.1(c)) was converted to a grayscale map using grayscale-calibration data. This grayscale map was used to expose the sample using the Heidelberg µPG 101 pattern generator, which works by direct-laser-writing. The sample was then developed in AZ 1:1 developer for 90s. In grayscale

patterning of positive photoresist, larger exposure dose (or larger grayscale) leads to shallower features after development. An optical micrograph of the polychromat is shown in Figure 3.3(a). To estimate the fabrication errors, a surface profiler (Tencor P20h) was used to measure heights along the X direction of the polychromat. Comparison between the design and measured heights shows an average error of ~50 nm, which is sufficient to generate excellent optical performance based on our previous study of fabrication-error tolerance [31,32]. In the future, the polychromat can be readily replicated by imprinting techniques with high fidelity for mass production [33].

3.5 Optical Characterization

The optimized polychromat is meant to efficiently manipulate the sunlight intensity distribution in the spatial-spectral domain. Therefore, it is essential to measure the spatial-spectral response of the polychromat. We first illuminated the polychromat by a collimated beam from a broadband supercontinuum source (NKT Photonics). A multimode fiber was placed at the image plane of the polychromat, which was at a distance d =163 mm (see Figure 3.1(a)). The fiber tip was mounted on a motorized stage and the other end was connected to a spectrometer (Ocean optics Jazz). The fiber tip was scanned for 14.25mm along the X direction in the image plane and the spectrum was stored at each location. These measurements were used to create the spatial-spectral intensity map shown in Figure 3.3(b). We also simulated the spatial-spectral map of the designed polychromat at the same distance d, shown in Figure 3.3(c). Excellent agreement between measurement and simulation is noted. The optical efficiency of a particular band can be defined as the ratio of the integrated power incident upon that band to the total incident power from the sun.

Measured and simulated optical efficiencies as a function of wavelength are shown in Figure 3.3(d). They match quite well. The decrease of optical efficiency in measurement is primarily due to fabrication error of the polychromat (~50nm) and the finite aperture of the multimode filter tip used in measurement. Nevertheless, this fabrication error poses trivial impact on the ultimate performance of the system, as described below.

3.6 Electrical Measurements

Electrical measurements were performed under ambient sunlight on three separate days with mostly clear skies: September 18, 20 and 23, 2015. Figure 3.4(a) shows a photograph of the measurement setup. An optical rail was placed on an adjustable mount. Two filter holders were used to hold the polychromat and the solar cells. To make the incident light normal to the polychromat, a simple alignment procedure was developed using a square-array mask and a target screen as shown in Figure 3.4(b). The shadow of the mask pattern was aligned to the target pattern on the screen. After alignment, the solar cells were placed at a distance of 163mm from the polychromat. The solar cells were positioned at appropriate bands of the image plane. Current-voltage characteristics were measured for each cell with and without the polychromat. For the reference, we used the measurements without the polychromat, but with the light passing through unpatterned glass substrate to account for any Fresnel reflections. The results obtained on September 18 are plotted in Figure 3.5. Short-circuit current densities of GaInP and C3847 cells were increased by 36.79% and 13.46%, respectively. Open circuit voltages were increased by 1.11% and 0.25%, respectively. Power densities were also calculated from the current voltage measurements. Increase in peak power densities were 39.46% and 12.84%,

respectively. The overall increase was 25.80% compared to the performance without the polychromat. Measurements from all three days are summarized in Table 3.1. The principle of power density enhancement in this photovoltaic system primarily comes from two factors: (1) more photons over a broader spectrum are harnessed due to the introduction of the lower bandgap, which essentially increases current; (2) utilization rate of photon energy is increased due to the introduction of higher bandgap, which increases output voltage. These two factors effectively mitigate the aforementioned nonabsorption loss and thermalization loss, respectively.

3.7 Analysis

It is important that the solar cells are aligned with the appropriate bands in the image plane of the polychromat as accurately as possible. To investigate the effect of relative shift between the solar cells and corresponding spectral bands on the power boost, we performed a simulation study that is summarized in Figures 3.6(a) and (b). Positive alignment errors were defined as the shift of the solar cells to the right (+X direction) with respect to the corresponding spectral bands (Figure 3.6(a)). Net power boost decreases for shifts in both direction (Figure 3.6(b)). Power boost reduces to zero at ~3.75 mm and ~3 mm for positive and negative shifts, respectively.

Another important consideration is the impact of the angle of incidence of sunlight on the polychromat. The polychromat was designed assuming normal incidence. To investigate the impact of oblique incidence, we considered incident angles (from normal) of -1.4° to 1.1° and calculated the diffracted field and the corresponding power boost of the solar cells for each angle. Figure 3.6(c) illustrates the percent change in power boosts

for different incident angles. Net power boost reduces to zero at ~1.35° and ~1.05°. Note that the results look similar to the ones presented in Figure 3.6(b). This is due to the fact that with the change of the angle of incidence, the diffraction pattern undergoes a lateral shift (in X direction), which is equivalent to misalignment of solar cells with respect to the spectral bands. The angle of incidence can be approximately related to the lateral misalignment Δx by $\theta = \Delta x/d$, where d is the gap between the polychromat and the solar cell plane (see Figure 3.1(a)). In general, such polychromat based spectrum splitting system would require solar tracking (in this case single axis tracking) to maintain high power boost. By reducing the distance, d, it is possible to reduce the required precision of tracking. In order to reduce d, while maintaining concentration, we will require higher diffractive power, which in turn requires smaller polychromat pixels. This can be improved in the future with better manufacturing processes.

The polychromat was designed for the standard AM1.5 spectrum [34]. However it is important to know the effect of variation in spectral irradiance on the performance of the system. We firstly obtained spectral irradiance data (1) for different hours of two separate days (21st of June and December, 2015) and (2) for hour 12, day 15 of each month over a year using the solar spectrum calculator developed by PV Lighthouse [35]. Input parameters for this calculator are given in Table 3.2. We simulated the net power boost of GaInP-C3847 configuration for each spectrum keeping all other parameters the same as were used for designing the original polychromat for the AM1.5 spectrum. Although the open circuit voltages and fill factors of the two cells change with spectrum, we neglected this in our simulation for simplicity. The results are shown in Figure 3.7. The change in net power boost, compared with the reference case without spectrum-splitting and

concentration, varies by less than 2% over the course of the daylight hours for both days considered (Figures 3.7(d), (e), (g), (h)). Over the course of the year, the power boost from the CIGS cell changes by up to 10% (Figure 3.7(f)). However, the net power boost of the system is dominated by the GaInP cell, which does not change much. As a result, the change in the net power boost (at hour 12, day 15 of the month) over the course of the year is less than 1% (Figure 3.7(i)). These results indicate that the polychromat-based spectrum splitting is robust to small changes in the incident spectrum over time.

It has been found that degradation in CIGS cells primarily results from increase in series resistance [36,37]. This, in turn reduces the fill factor. To analyze the effect of fill factor loss on polychromat performance, we reduced the fill factors of GaInP and CIGS cells by 0 to 10% and calculated the net power boost for each fill-factor combination. The results are summarized in Figure 3.8. No change in net power boost was found if the fill factor of both cells reduced by same amount (along the diagonal line in Figure 3.8). Net power boost increases if the fill factor of only the CIGS cell reduces and that of the GaInP cell remains unchanged. The opposite happens, if fill factor of GaInP reduces, *i.e.*, net power boost decreases. The net power boost changes by as much as +/- 2% as a result of the degradation of the fill factors.

3.8 Conclusions

Here, we show that one can increase the output power from a photovoltaic device by spectrally separating sunlight into two bands and concentrating these bands onto two single-junction solar cells positioned in the same plane via a broadband, planar diffractive optic. Such configuration successfully circumvents the issues of current- and lattice-

matching present in traditional multijunction photovoltaics. Specifically, we used GaInP and CIGS cells with a geometric concentration of 3X. It was experimentally demonstrated an increase in output power of about 25% under ambient sunlight. Our numerical calculation indicates that this power boost is insusceptible to daily and annual variation of solar spectrum. Fill-factor degradation also brings negligible effect on its performances. The principle can clearly be extended to more bands and higher concentrations in order to achieve ultrahigh efficiency photovoltaics [31]. Furthermore, since the polychromat is an ultrathin planar optic, it can be inexpensively manufactured using imprinting techniques over large areas [33].
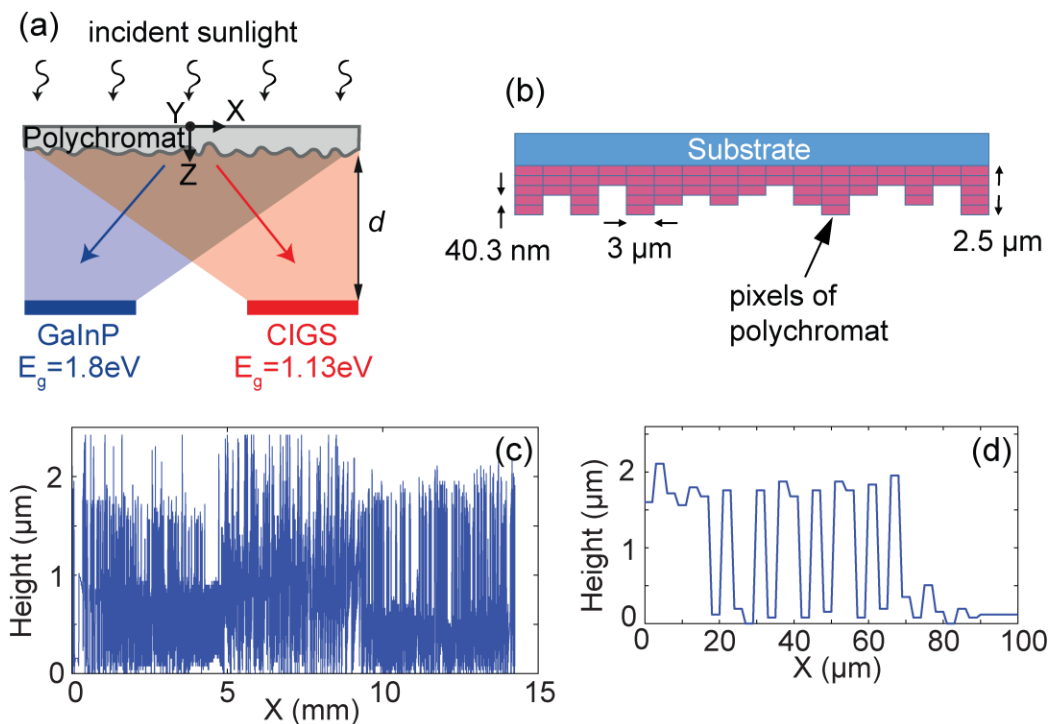
Figure 3.1. Details of the polychromat. a) Schematic of polychromat-solar cells configuration showing the spectrum splitting incident sunlight into two bands with 3X concentration. (b) Schematic illustration of a short segment of the polychromat (X-Z cross-section). Discrete pixels of various heights are clearly shown. (c) Optimized height profile of the polychromat. (d) Height distribution of left-most 100μm of the optimized polychromat in (c).
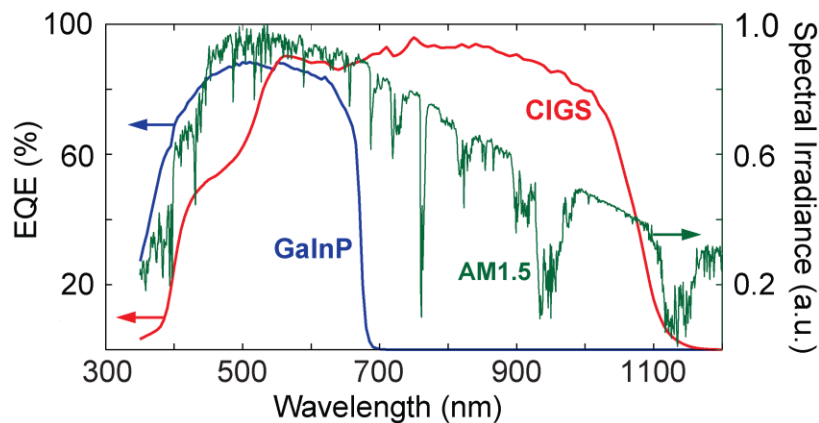
Figure 3.2. EQEs of GaInP (blue line) and CIGS (red line) cells and normalized spectral irradiance of the standard AM 1.5 spectrum (green line).
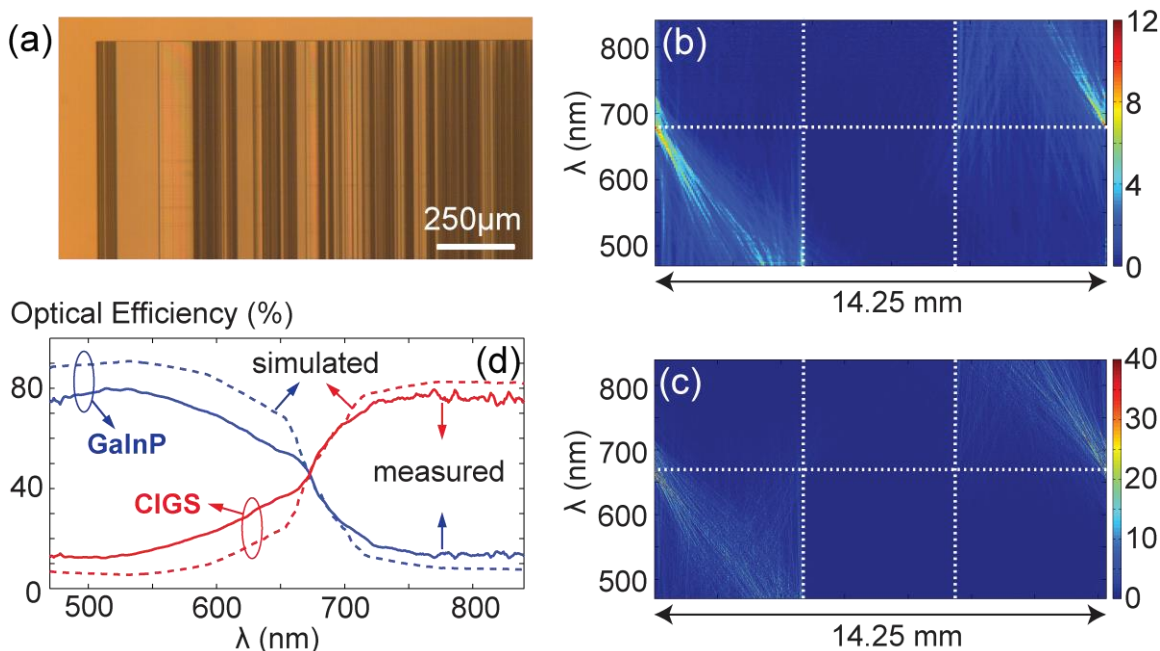
Figure 3.3. Optical characterization. a) Micrograph of the one corner of the fabricated polychromat. Measured (b) and simulated (c) spatial-spectral intensity maps in the image plane of the optimized polychromat. (d) Optical-efficiency spectra of the two bands. (Blue line for GaInP and red line for CIGS).
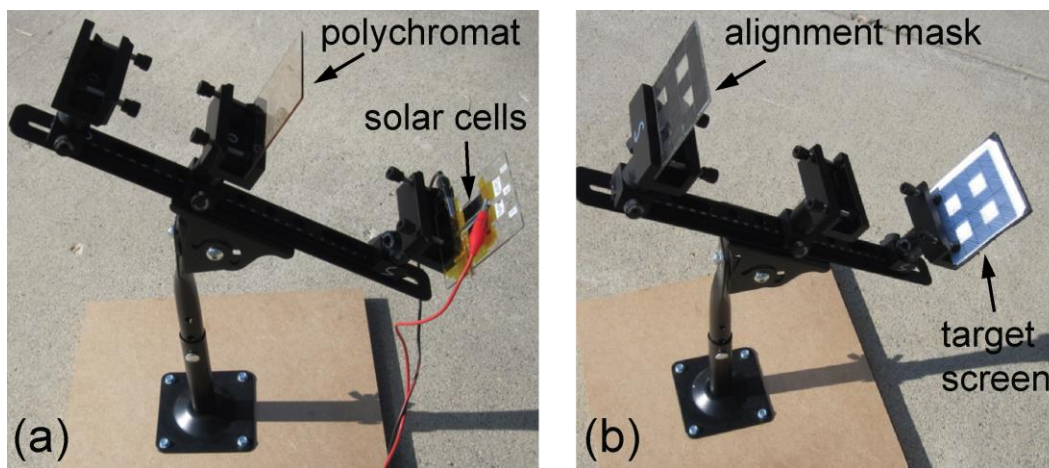
Figure 3.4. Electrical characterization. (a) Experimental setup for outdoor electrical measurements. Holder on top-left is used for the polychromat, while that at the bottom-right is used to hold the solar cells. (b) To ensure that the incident sunlight is normal to the polychromat, first an alignment mask (left) is placed such that its shadow lines up with a target screen (right). The mask and target correspond to the positions of the polychromat and the solar cells, respectively.
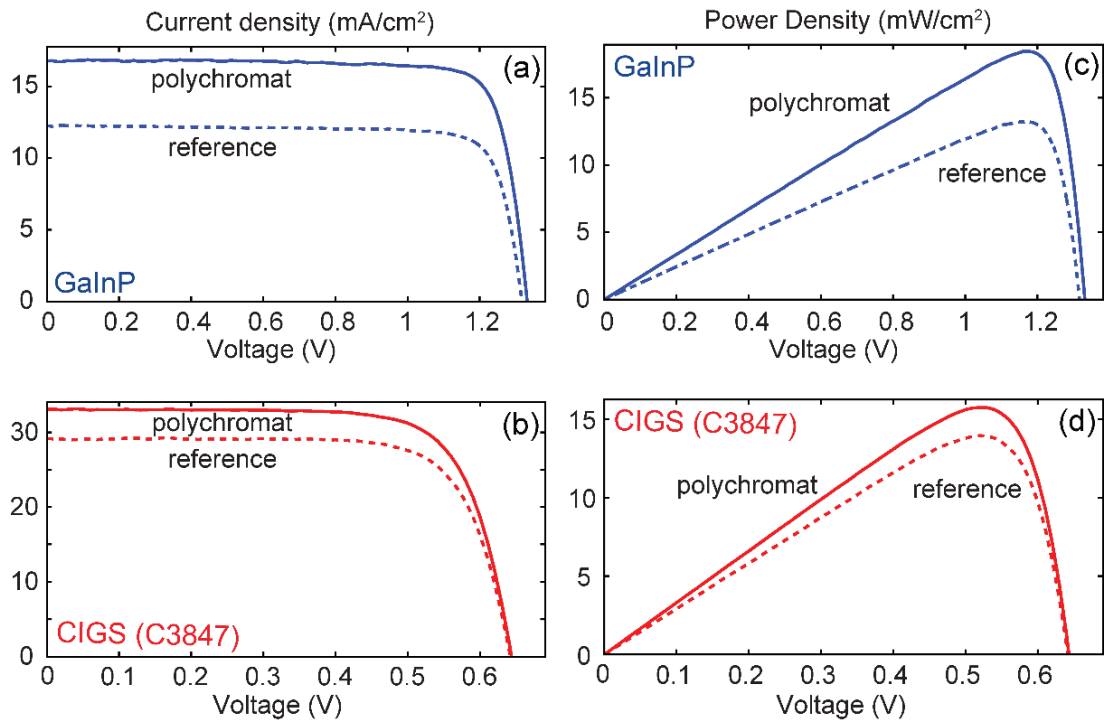
Figure 3.5. Electrical measurements of the solar cells. Current-voltage plots of (a) GaInP and (b) CIGS cells. Power density vs. voltage plots of (c) GaInP and (d) CIGS cells.
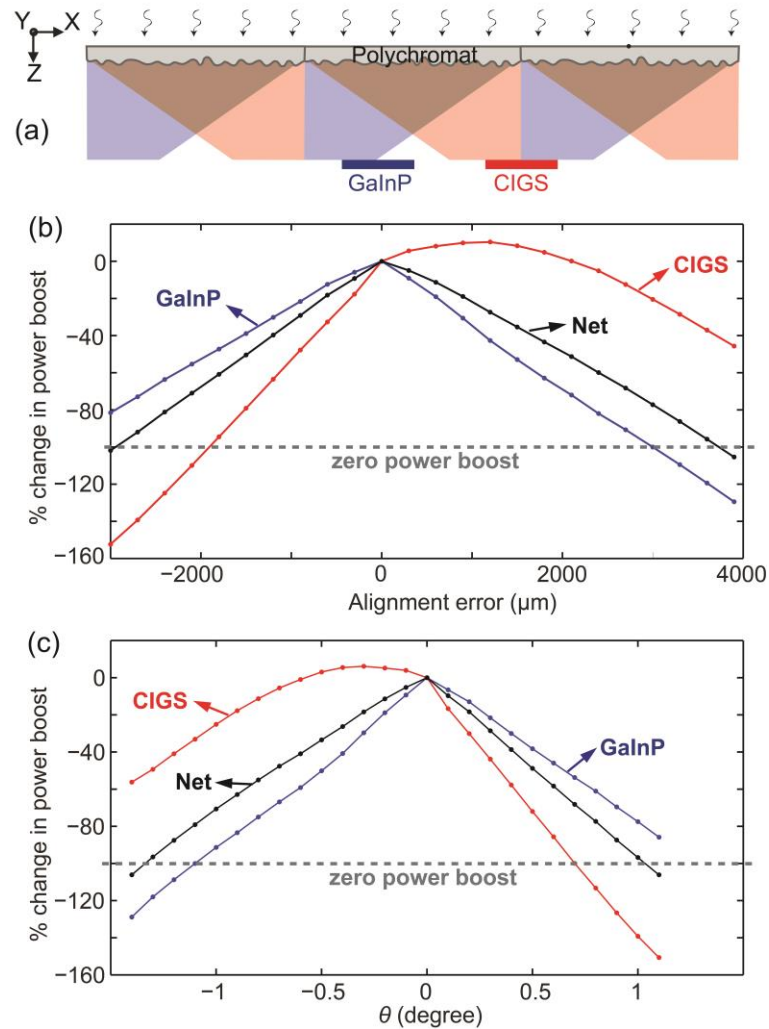
Figure 3.6. . Impact of alignment error and angle of incidence on power boost. (a) An example of positive alignment error: both solar cells were shifted to the right with respect to the corresponding spectral bands. (b) % change in power boost of GaInP (blue), CIGS (red) and overall system (black). (c) % change in power boost of GaInP (blue), CIGS (red) and overall system (black) as a function of angle of incidence. Gray dashed line represents zero power boost in (b) and (c).
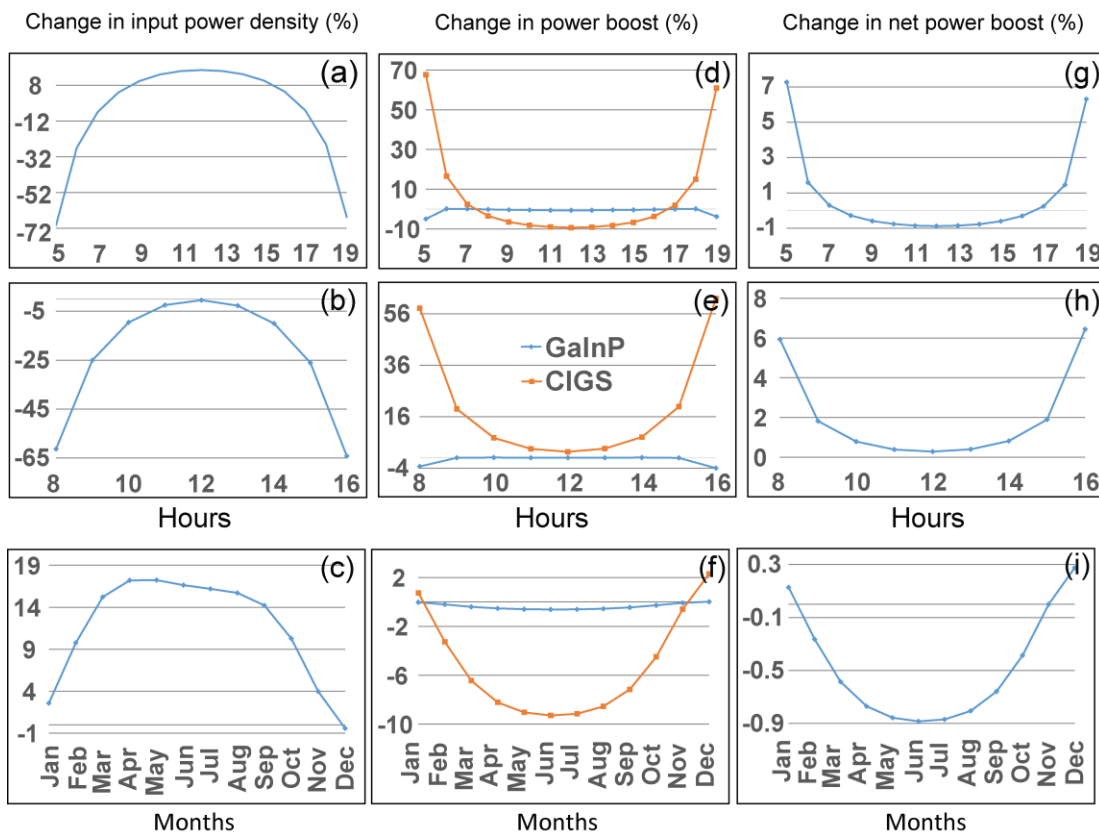
Figure 3.7. Impact of the spectral variation on polychromat-photovoltaic performance. (a)-(c) Incident power density, (d)-(f) percentage change in power boost of GaInP (blue) and CIGS (red), (g)-(i) percentage change in net power boost at different times. (a), (d), (g) are for different hours of June 21, 2015; (b), (e), (h) are for different hours of December 21, 2015; (c), (f), (i) are for hour 12, day 15 for different months.
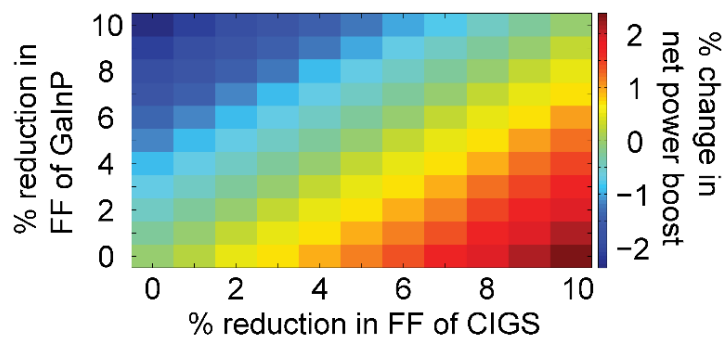
Figure 3.8. Impact of the degradation of the fill-factor on power boost.

Table 3.1 Electrical measurements of the GaInP and CIGS solar cells with and without

polychromat under AM1.5 spectrum illumination on three separate days

	September 18		September 20		September 23	
Solar cell	GaInP	CIGS	GaInP	CIGS	GaInP	CIGS
J_{sc_ref} (mA/cm^2)	12.2449	29.1655	12.5052	29.8216	12.2224	28.8350
J_{sc_poly} (mA/cm^2)	16.7494	33.0904	16.8665	33.1984	16.4275	31.2514
V_{oc_ref} (V)	1.3167	0.6418	1.3174	0.6300	1.2882	0.6110
V_{oc_poly} (V)	1.3314	0.6434	1.3309	0.6500	1.3060	0.6200
FF_{ref}	0.8211	0.7455	0.8229	0.7470	0.8183	0.7416
FF_{poly}	0.8279	0.7396	0.8231	0.7454	0.8228	0.7516
P_{max_ref} (mW/cm^2)	13.2393	13.9544	13.5574	14.0335	12.8845	13.0440
P_{max_poly} (mW/cm^2)	18.4629	15.7468	18.4758	15.8377	17.6449	14.5629
Power Boost (%)	39.4553	12.8446	36.2785	12.8560	36.9470	11.6446
Net Power Boost (%)	25.80		24.37		24.22	

Table 3.2 Input parameters for solar spectrum calculator

Inputs	Value
Incident spectrum	AM0
Transmission model	SPCTRAL2 [Bir86]
Atmospheric pressure	1013.25 mb
Turbidity at 500 nm	0.084
Water vapor absorption	1.4164 cm
Ozone	0.3438 atm-cm
Albedo	0.1
Latitude	40.768998°
Longitude	-111.846667°
Minimum wavelength	280 nm
Maximum wavelength	4000 nm
Wavelength interval	10 nm

3.9 References

[1] W. Shockley, and H. J. Queisser, "Detailed balance limit of efficiency of p-n junction solar cells," J. Appl. Phys. **32**, 510 (1961).

[2] A. Polman, and H.A. Atwater, "Photonic design principles for ultrahigh-efficiency photovoltaics," Nat. Mater. **11**, 174 (2012).

[3] A. Luque, "Will we exceed 50% efficiency in photovoltaics?" J. Appl. Phys. **110**, 031301 (2011).

[4] R. R. King, D. C. Law, K. M. Edmondson, C. M. Fetzer, G. S. Kinsey, H. Yoon, R. A. Sherif and N. H. Karam, "40% efficient metamorphic GaInP∕ GaInAs∕ Ge multijunction solar cells," Appl. Phys. Lett. **90**, 183516 (2007).

[5] S. M. Leite, R. L. Woo, J. N. Munday, W. D. Hong, S. Mesropian, D. C. Law, and H. A. Atwater, "Towards an optimized all lattice-matched InAlAs/InGaAsP/InGaAs multijunction solar cell with efficiency> 50%," Appl. Phys. Lett. **102**, 033901 (2013).

[6] K. Derendorf, S. Essig, E. Oliva, V. Klinger, T. Roesener, S. P. Philipps, J. Benick, M. Hermle, M. Schachtner, G. Siefer, and W. Jäger, "Fabrication of GaInP/GaAs//Si solar cells by surface activated direct wafer bonding," IEEE J. Photovolt. **3**, 1423 (2013).

[7] F. Dimroth, M. Grave, P. Beutel, U. Fiedeler, C. Karcher, T. ND Tibbits, E. Oliva, G. Siefer, M. Schachtner, A. Wekkeli, and A. W. Bett, "Wafer bonded four-junction GaInP/GaAs//GaInAsP/GaInAs concentrator solar cells with 44.7% efficiency," Prog. Photovolt.: Res. Appl. **22**, 277 (2014).

[8] L. Fraas, J. Avery, V. Sundaram, V. Dinh, T. Davenport, J. Yerkes, J. Gee, and K. Emery, "Over 35% efficient GaAs/GaSb stacked concentrator cell assemblies for terrestrial applications," in Proceedings of IEEE Photovoltaic Specialists Conference, (1990), pp. 190-195.

[9] X. Sheng, C. A. Bower, S. Bonafede, J. W. Wilson, B. Fisher, M. Meitl, H. Yuen, S. Wang, L. Shen, A. R. Banks, and C. J. Corcoran, "Printing-based assembly of quadruple-junction four-terminal microscale solar cells and their use in high-efficiency modules," Nat. Mater. **13**, 593 (2014).

[10] A. G. Imenes, and D. R. Mills, "Spectral beam splitting technology for increased conversion efficiency in solar concentrating systems: a review," Sol. Energ. Mater. Sol. C. **84**, 19 (2004).

[11] A. Mojiri, R. Taylor, E. Thomsen, and G. Rosengarten, "Spectral beam splitting for efficient conversion of solar energy—A review," Renew. Sust. Energ. Rev. **28**, 654 (2013).

[12] H. A. Macleod, *Thin-film Optical Filters* (CRC Press, New York, 2001).

[13] A. Barnett, D. Kirkpatrick, C. Honsberg, D. Moore, M. Wanlass, K. Emery, R. Schwartz, D. Carlson, S. Bowden, D. Aiken, and A. Gray, "Very high efficiency solar cell modules," Prog. Photovolt.: Res. Appl. **17**, 75 (2009).

[14] J. D. McCambridge, M. A. Steiner, B. L. Unger, K. A. Emery, E. L. Christensen, M. W. Wanlass, A. L. Gray, L. Takacs, R. Buelow, T. A. McCollum, and J. W. Ashmead, "Compact spectrum splitting photovoltaic module with high efficiency," Prog. Photovolt.: Res. Appl. **19**, 352 (2011).

[15] B. Mitchell, G. Peharz, G. Siefer, M. Peters, T. Gandy, J. C. Goldschmidt, J. Benick, S. W. Glunz, A. W. Bett, and F. Dimroth, "Compact spectrum splitting photovoltaic module with high efficiency," Prog. Photovolt.: Res. Appl. **19**, 61 (2011).

[16] C. N. Eisler, E. D. Kosten, E. C. Warmann, and H. A. Atwater, "Spectrum splitting photovoltaics: Polyhedral specular reflector design for ultra-high efficiency modules," in Proceedings of IEEE Photovoltaic Specialists Conference, (2013), pp. 1848-1851.

[17] X. Wang, N. Waite, P. Murcia, K. Emery, M. Steiner, F. Kiamilev, K. Goossen, C. Honsberg, and A. Barnett, "Lateral spectrum splitting concentrator photovoltaics: direct measurement of component and submodule efficiency," Prog. Photovolt.: Res. Appl. **20**, 149 (2012).

[18] A. Dorodnyy, V. Shklover, L. Braginsky, C. Hafner, and J. Leuthold, "High-efficiency spectrum splitting for solar photovoltaics," Sol. Energ. Mater. Sol. C **136**, 120 (2015).

[19] T. Kinoshita, K. Nonomura, N. J. Jeon, F. Giordano, A. Abate, S. Uchida, T. Kubo, S. I. Seok, M. K. Nazeeruddin, A. Hagfeldt, and M. Grätzel, "Spectral splitting photovoltaics using perovskite and wideband dye-sensitized solar cells." Nat. Commun. **6**, 8834 (2015).

[20] S. Rühle, A. Segal, A. Vilan, S. R. Kurtz, L. Grinis, A. Zaban, I. Lubomirsky, and D. Cahen, "A two junction, four terminal photovoltaic device for enhanced light to electric power conversion using a low-cost dichroic mirror," J. Renew. Sust. Energ. **1**, 013106 (2009).

[21] K. Xiong, S. Lu, J. Dong, T. Zhou, D. Jiang, R. Wang, and H. Yang, "Light-splitting photovoltaic system utilizing two dual-junction solar cells," Sol. Energ. **84**, 1975 (2010).

[22] R. K. Kostuk, and G. Rosenberg, "Analysis and design of holographic solar concentrators," Proc. SPIE **7043**, 70430I (2008).

[23] D. Zhang, M. Gordon, J. M. Russo, S. Vorndran, M. Escarra, H. Atwater, and R. K. Kostuk, "Reflection hologram solar spectrum-splitting filters," Proc. SPIE **8468**, 846807 (2012).

[24] M. D. Escarra, S. Darbe, E. C. Warmann, and H. A. Atwater, "Spectrum-splitting photovoltaics: Holographic spectrum splitting in eight-junction, ultra-high efficiency module," in Proceedings of IEEE Photovoltaic Specialists Conference, (2013), pp. 1852-1855.

[25] G. B. Ingersoll, D. Lin, and J. R. Leger, "Experimental verification of spectral grating interference in multiplexed volume holograms employed as broadband dispersive elements for solar concentrators," Proc. SPIE **8821**, 882107 (2013).

[26] M. Stefancich, A. Zayan, M. Chiesa, S. Rampino, D. Roncati, L. Kimerling, and J. Michel, "Single element spectral splitting solar concentrator for multiple cells CPV system," Opt. Express **20**, 9004 (2012).

[27] C. Maragliano, M. Chiesa, and M. Stefancich, "Point-focus spectral splitting solar concentrator for multiple cells concentrating photovoltaic system," J. Opt. **17**, 105901 (2015).

[28] J. R. Onffroy, D. E. Stoltzmann, R. J. H. Lin, and G. R. Knowles, "High-efficiency concentration/multi-solar-cell system for orbital power generation" in Proceedings of the 15th Intersociety Energy Conversion Engineering Conference, (1980), pp. 371–376.

[29] C. Michel, J. Loicq, F. Languy, and S. Habraken, "Optical study of a solar concentrator for space applications based on a diffractive/refractive optical combination," Sol. Energ. Mater. Sol. C. **120**, 183 (2014).

[30] G. Kim, J-A. Domínguez-Caballero, and R. Menon, "Design and analysis of multi-wavelength diffractive optics," Opt. Express **20**, 2814 (2012).

[31] P. Wang, J-A. Dominguez-Caballero, D. Friedman, and R. Menon, "A new class of multi-bandgap high-efficiency photovoltaics enabled by broadband diffractive optics," Prog. Photovolt.: Res. Appl. **23**, 1073 (2015).

[32] N. Mohammad, P. Wang, D. J. Friedman, and R. Menon, "Enhancing photovoltaic output power by 3-band spectrum-splitting and concentration using a diffractive micro-optic," Opt. Express **22**, A1519 (2014).

[33] N. Mohammad, P. Wang, D. J. Friedman, K. Ramanathan, L. Mansfield and R. Menon, "Microphotonic spectrum-splitting & concentration for high-efficiency photovoltaics," in CLEO: Applications and Technology, San Jose, U.S.A., (2015), pp. ATu2J.2.

[34] See http://rredc.nrel.gov/solar/spectra/am1.5/

[35] See https://www.pvlighthouse.com.au/calculators

[36] D. C. Jordan, and S. R. Kurtz, "Photovoltaic degradation rates—an analytical review," Prog. Photovolt.: Res. Appl. **21**, 12 (2013).

[37] J. A. del Cueto, S. Rummel, B. Kroposki, C. Osterwald, and A. Anderberg, "Stability of CIS/CIGS modules at the outdoor test facility over two decades" in Proceedings of IEEE Photovoltaic Specialists Conference, (2008), pp. 1-6.

CHAPTER 4

CHROMATIC ABERRATION CORRECTED DIFFRACTIVE LENS

This chapter is adapted with permission from the author's previous publication: P. Wang,

N. Mohammad and R. Menon, "Chromatic-aberration-corrected diffractive lenses for ultra-

broadband focusing," Sci. Rep. **6**, 21545 (2016).

4.1 Abstract

We exploit the inherent dispersion in diffractive optics to demonstrate planar chromatic-aberration-corrected lenses. Specifically, we designed, fabricated and characterized cylindrical diffractive lenses that efficiently focus the entire visible band (450nm to 700nm) onto a single line. These devices are essentially pixelated, multilevel microstructures. Experiments confirm an average optical efficiency of 25% for a three-wavelength apochromatic lens whose chromatic focus shift is only 1.3μm and 25μm in the lateral and axial directions. Super-achromatic performance over the continuous visible band is also demonstrated with averaged lateral and axial focus shifts of only 1.65μm and 73.6μm, respectively. These lenses are easy to fabricate using single-step grayscale lithography and can be inexpensively replicated. Furthermore, these devices are thin (< 3μm), error tolerant, has low aspect ratio (< 1:1) and offer polarization-insensitive focusing, all significant advantages compared to alternatives that rely on metasurfaces. Our design methodology offers high design flexibility in numerical aperture and focal length, and is readily extended to 2D.

4.2 Introduction

Recent work has suggested the use of metalenses for broadband achromatic focusing [1]. Here, we show that it is not necessary to invoke concepts of metasurfaces or metalenses to enable such focusing. Scalar diffractive optics, when designed appropriately, can readily enable ultrabroadband achromatic focusing. Such diffractive optics can be far simpler to manufacture and can allow for polarization-independent focusing. An ideal lens focuses one point in the object space to one point in the image space [2]. Almost all imaging

systems suffer from chromatic aberrations, which means that light of different wavelengths generate focal spots at different spatial locations [2]. This phenomenon deteriorates the performance of both imaging [3,4] and nonimaging [5] systems under broadband illumination. For instance, a color camera without chromatic-aberration correction will form spatially displaced and defocused images of the blue, green and red channels.

Chromatic aberration is due to either the dispersion properties of the material or the structure of the optic. For refractive lenses, longer wavelengths focus at a farther distance, since in most dielectric materials, the refractive index decreases at longer wavelengths. Figure 4.1(a) illustrates the simple example of a biconvex glass lens and the corresponding shift of its focus, calculated by the Lensmaker's equation [2]. The conventional diffractive lens (zone-plate), on the other hand, exhibits opposite chromatic aberration (Figure 4.1(b)) [6-8]. Diffraction angle is proportional to wavelength [2], and thus longer wavelengths are focused closer than shorter ones.

Chromatic aberration can be corrected approximately by using materials that exhibit complementary dispersion, as in an achromatic doublet and triplet [9-11]. However, this technique is cumbersome, since the number of materials equals the number of wavelengths where the chromatic aberrations are minimized [10,11]. The extra alignment makes these lenses expensive and bulky. Hybrid refractive-diffractive lenses perform slightly better, but their complexity is even higher [12-14]. Such designs that work for more than three wavelengths are seldom studied. An alternative approach is to use a phase-coded aperture [15], but this requires precise polishing of the glass surface. In all these cases, it is challenging to make such corrected lenses with microscale thickness.

Metasurfaces exploit surface plasmonic or nanophotonic phenomena to locally

impart abrupt phase shift so as to purposely manipulate the diffraction pattern [16,17]. Previous studies showed its potential in anomalous reflection and refraction, and complex beam generation [16,18,19]. Here, we emphasize that metasurfaces are excellent, when the vector properties of light must be manipulated as in the case of a high-efficiency polarizer [20], but they are not required to manipulate the scalar properties of light. Diffractive optics is a better alternative. The fabrication requirements for metasurfaces are far more stringent in terms of both resolution and precision compared to diffractive optics. Furthermore, metasurfaces are by nature polarization sensitive [1,16-20]. Here, we reiterate that diffractive optics can readily enable broadband focusing, while still maintaining the planar architecture. Previously, we have functionalized diffractive optics as a solar spectrum splitter/concentrator [21], multicolor encoder [22], phase masks for 3D lithography [23] and dispersion elements in computational spectroscopy [24].

Here, we extend the concept of broadband diffractive optics to super-achromatic focusing. Specifically, we designed, fabricated and characterized 4 different planar cylindrical chromatic-aberration-corrected lenses. Each lens has a maximum thickness of 3μm and a minimum feature size of 3μm. All the devices can be readily patterned using grayscale lithography and inexpensively replicated for mass-production using imprint lithography [25,26]. The aberration-correction capabilities of our lenses are on par with or better than commercial doublets. Two types of lenses were constructed. One was designed for three discrete wavelengths, and the other for continuous broadband illumination.

4.3 Working Principle

The cross-sectional schematic of our chromatic-aberration-corrected diffractive lens (CACDL) is illustrated in Figure 4.2(a). The CACDL is composed of pixels that can be square (2D) or linear grooves (1D). In the devices described here, the grooves are of width, Δ=3µm and height, h_i is assigned to the ith groove. Each groove imparts a relative phase shift given by $\varphi_i = \frac{2\pi}{\lambda} h_i (n(\lambda) - 1)$, where n($\lambda$) is the refractive index of device material at wavelength λ [22]. For simplicity, we utilize a positive-tone photoresist, SC1827 deposited on a soda-lime glass substrate as the device material. A commercial grayscale lithography tool was employed to rapidly pattern the device in a single step [21-24]. The width, Δ is dictated by the resolution of this tool.

In order to achieve super-achromatic performance, we applied a modified direct-binary-search (DBS) algorithm to optimize the distribution of groove heights, h_i [21-24,27]. It is a perturbation-based iterative method. Details of the design algorithm are included in the Supplementary Materials. The target point-spread function (PSF) is defined as a diffraction-limited Gaussian with full-width-at-half-maximum (FWHM) determined by $w = \frac{\lambda}{2NA}$. The numerical aperture (NA) is given by $\sin\left(\tan^{-1}(\frac{2f}{L})\right)$ in which L=NΔ is the total length of the lens, N is the total number of grooves, and f is the design focal length. Compared to other optimization algorithms for multi-wavelength diffractive optics [28,29], our technique is applicable generally [20-24] and our approach is the first experimental demonstration of super-achromatic and continuous broadband focusing using diffractive optics.

The diffraction pattern in the focal plane is determined by the phase acquired by

light transmitting the diffractive lens (Figure 4.2(c)) and that acquired via the optical path length in air (Figure 4.2(b)). For chromatic-aberration-corrected focusing at x', three or more wavelengths must diffract from location, x such that they interfere constructively at the focus, x'. Our method for designing the diffractive lens realizes an optimal height distribution that can approximate such constructive interference. In our lens, there are N grooves, and each groove can occupy P discrete height levels. Therefore, the total degrees-of-freedom can be enormous, P^N. This allows extreme design flexibility as illustrated later. We designed and fabricated four CACDLs (see Figure 4.2(d)). For each device, we assumed periodic boundaries during design and fabricated 7 periods, each of length L=8.4mm. The optical micrographs, profilometer measurements of the topography and the scanning-electron micrographs of exemplary devices are shown in Figures 4.2(e), (f) and (g), respectively. The cross-sectional micrographs of a cleaved sample (Figure 4.2(g)) indicate that the grooves are rounded due to the resolution limitations of our lithography tool. Nevertheless, the average height within each groove was within 100nm of the design value. It is noteworthy that the maximum aspect ratio is 1:1, which is much smaller than that of the metalenses [1,30]. Furthermore, the lithographic resolution required for our CACDLs is only 3µm (5λ for λ=600nm) compared to ~100nm (0.065λ for λ=1550nm) for the metalenses [1]. To achieve broadband focusing in the visible region with the metalenses, one would require features of size 39nm and aspect ratios of over 3:1.

4.4 Experiment and Results

To experimentally demonstrate chromatic-aberration-corrected focusing, we illuminated each CACDL using a spatially collimated beam from a super-continuum source

(SuperK EXTREME EXW-6) that was first conditioned using a reconfigurable band-pass filter (SuperK VARIA). The filter allowed us to illuminate the CACDL with one discrete wavelength at a time (minimum bandwidth 10nm). Then, a single-mode fiber (SMF, core diameter ~8µm) connected to a spectrometer (Ocean Optics Jaz) was placed in the vicinity of the designed focus. The fiber was scanned using a motorized 2-axis stage with 3µm and 10µm steps along the X' and Z axes, respectively. The transmitted spectra were collected at each location. The final results were derived after subtracting the dark spectrum from the raw data and dividing by the reference spectrum (that transmitted through the unpatterned photoresist).

First, we consider the CACDLs designed for three discrete wavelengths (460nm, 540nm and 620nm). To demonstrate the flexibility of our approach, we designed 3 different lenses with the following parameters: number of grooves, N = 2800, 2800, 280; focal length, f = 120mm, 25mm and 10mm, which correspond to numerical aperture, NA = 0.035, 0.166 and 0.042, respectively. Figures 4.3(a)-(i) summarize the simulated and measured light-intensity distributions in the focal plane at the 3 design wavelengths. As expected all 3 lenses exhibit clear apochromatic focusing. Scalar-diffraction simulations predict average optical efficiencies of 30.0%, 30.4% and 39.0% for the 3 designs. The corresponding measured average optical efficiencies are 24.9%, 23.0% and 21.5%, much higher than those of previously reported achromatic lenses [13]. In theory, non-ideal efficiency (<100%) is primarily due to lack of perfect interference (constructive at focus and destructive in the background). Generally speaking, this efficiency dictates the contrast or resolution in an optical system. Here, we define the optical efficiency as the ratio of power within the region defined by the first zero to the total incident power. We can also

quantify the achromaticity of the CACDLs by measuring the lateral and axial focus shifts as a function of wavelength. These can be calculated by comparing the 2D PSF (X'Z plane) at each wavelength to that at the center wavelength, 540nm. The lateral and axial focus shifts for the first design were 0.32μm, 6.7μm (simulation) and 1.3μm, 25μm (experiment), respectively. These are better than what can be achieved using conventional refractive lens combinations [9].

Due to the finite diameter of the SMF core, the measured PSFs are wider than the actual distributions. This is especially obvious in the CACDL with the highest NA (Figures 4.3(d)-(f)). Fabrication errors as well as the limited acceptance angle of the SMF contribute to the reduction of optical efficiencies. The 2D PSFs (X'Z) of the first design at five wavelengths (460nm, 500nm, 540nm, 580nm and 620nm) are plotted in Figures 4.3(j)-(n) (simulation) and Figures 4.3(o)-(s) (measurement). The scalar-diffraction simulation has resolution of 0.2μm and 2.5μm in X' and Z directions. The measured plots are numerically interpolated into the same grid for visual comparison. At the vicinity of the nominal focal plane (white-dashed lines), focusing is clearly observed for only the design wavelengths (460nm, 540nm and 620nm). No focusing is found at the other wavelengths (Figures 4.3(k), (p), (m) and (r)). Another simple evidence of apochromatic focusing is seen via the images captured at the focal plane using a monochrome sensor (DMM22BUC03-ML, The Imaging Source) with illumination wavelength selected by the VARIA filter, shown as insets in Figures 4.3(o)-(s). Note that the SMF-spectrometer scheme was used to accurately measure PSFs (Figures 4.3(a)-(i) and (o)-(s)), since the spectrometer has higher spectral resolution (0.4nm) than the VARIA filter and larger dynamic range (16-bit) than the sensor (8-bit).

Next, we extended our CACDL to focus continuous broadband illumination across the visible spectrum (450nm – 690nm, super-achromatic). This is achieved by increasing the wavelength sampling to 5nm during design. It was designed with N=2500, focal length, f=280mm, and NA=0.013. The simulated and measured 1D PSFs in the design focal plane as a function of wavelength are plotted in Figures 4.4(a) and (b), respectively. Note that the plots are normalized to the peak at each wavelength to account for the spectrum of the source. The white dots (left) and crosses (right) indicate the lateral (Δx) and axial (Δf) focal-spot shifts in each figure. These shifts were obtained from the 2D (X'Z) PSFs. The simulated and measured 2D PSFs at 3 wavelengths are illustrated in Figures. 4.4(d)-(f) and Figures 4.4(g)-(i), respectively. Again, the measurements were interpolated into the same resolution as the simulations. The lateral shift averaged over all wavelengths, $\overline{|\Delta x|}$ is 0.47μm (simulation) and 1.65μm (experiment). The axial shift averaged over all wavelengths, $\overline{|\Delta f|}$ is 23.5μm (simulation) and 73.6μm (experiment). The maximum axial-focus shift, Δf, is comparable to that of commercial achromatic doublets [9]. However, our CACDL is thin (planar), inexpensive and comprised of only a single material. The optical-efficiency spectrum is plotted in Figure 4.4(c). The discrepancies between the simulated and measured curves are primarily due to fabrication errors in the CACDL height profile. The efficiency drops at longer wavelengths. This can be prospectively compensated by appropriately weighting the efficiencies of different wavelengths during design [21] and by optimizing the patterning process. As before, monochrome images illuminated by the 3 wavelengths (selected by the VARIA) are shown as insets in Figures 4.4(g)-(i).

4.5 Discussions

The CACDLs are insensitive to the polarization state of the incident light. This is a strong advantage over metalenses, since most imaging systems require polarization-independent focusing. To prove this, we illuminated the first CACDL design (from Figure 4.2(a)) with linearly polarized light and observed the focus while the polarization was rotated by 90 degrees. In our nomenclature, the transverse magnetic (TM) refers to electric field polarized along the degenerate direction Y of the CACDL, while the transverse electric (TE) refers to that polarized along the X direction (see inset of Figure 4.5(a)). The measured PSFs for the 3 design wavelengths (Figures 4.5(a)-(c)) are identical for the orthogonal polarizations. Furthermore, finite-difference-time-domain (FDTD) simulations of diffraction by a single groove (Figure 4.5(d)) confirm that both amplitude and phase of the diffracted light are identical for both polarizations. This is expected since the smallest period of the CACDL is 6µm, much larger than the wavelengths of interest.

In all micro-optics, fabrication errors pose an important impact on the optical efficiencies. We numerically analyzed this impact by adding random errors with various standard deviations to the design-height distribution. The results plotted in Figure 4.5(e) indicate that the CACDLs are robust to height errors of up to ~100nm, which, in turn, corresponds to two height levels ($\Delta h=H/(P-1)=50nm$). Therefore, our device is relatively tolerant to fabrication errors, which is consistent with previous devices designed using related techniques [20-24]. As expected, the efficiency decreases with increasing errors (left Y axis in Figure 4.5(e)) and the device with fewer grooves (CACDL#3) is more susceptible to fabrication errors [21,22]. This is because constructive interference gradually breaks down when the phase distribution deviates from the optimal design. Moreover, the

wavelength-averaged axial-focus shift, $\overline{|\Delta f|}$ increases with errors (right Y axis in Figure 4.5(e)). For CACDL#1, $\overline{|\Delta f|}$ is maintained small when the error is less than 100nm, while that of the CACDL#4, it deteriorates rapidly. This is likely a consequence of the fact that broadband super-achromatic focusing requires a more stringent phase matching compared to the case of focusing only 3 wavelengths.

We also simulated the impact of oblique incidence (Figure 4.5(f)). The wavelength-averaged focus shifts both laterally and axially with change in incident angle, θ. Hence, the wavelength-averaged optical efficiency drops with off-normal incidence (top panel). Nevertheless, both studied CACDLs maintain their efficiencies over θ~±4°. The wavelength-averaged lateral-focus shift, $\overline{|\Delta x|}$ (middle panel) and axial-focus shift, $\overline{|\Delta f|}$ (bottom panel) increase nonlinearly with θ. However, both designs preserve reasonable chromatic aberrations over θ~±4°. Note that even though we assumed periodic boundaries during design, experiments suggest that this is not strictly necessary. Finally, although our devices were 1D, they can be readily extended to 2D [20,22,23] and also to almost any electromagnetic spectrum.

4.6 Author Contributions

P.W. and R.M. conceived and designed the experiments. P.W. modeled, optimized and characterized the devices. N.M. fabricated the devices. P.W. performed the experiments and numerical analysis. P.W. and R.M. analyzed the data and wrote the paper.
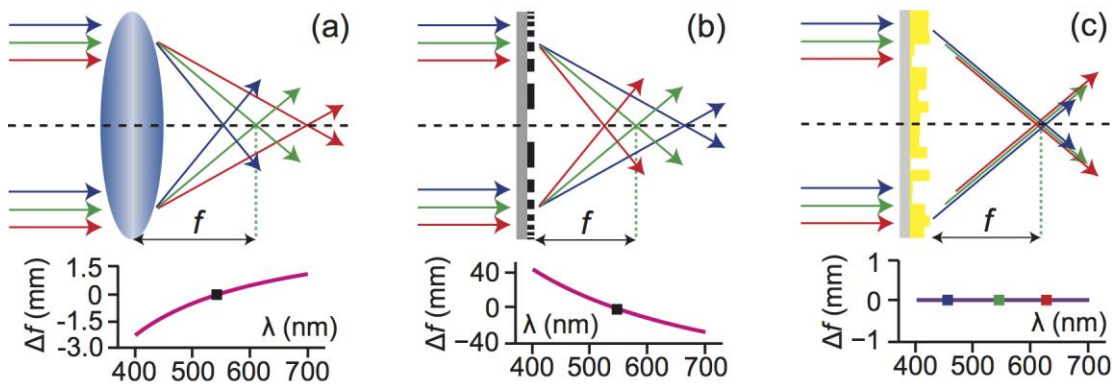
Figure 4.1. Focusing optics with nominal focal length f=120mm at λ=540nm (top row) and their calculated axial chromatic aberration Δf (bottom row). Normally incident uniform illumination is assumed. (a) Biconvex refractive lens (BK7 glass). (b) Amplitude (binary) zone-plate. (c) Schematic explanation of the super-achromatic diffractive lens. Ideally focus shift over the entire spectrum remains zero.
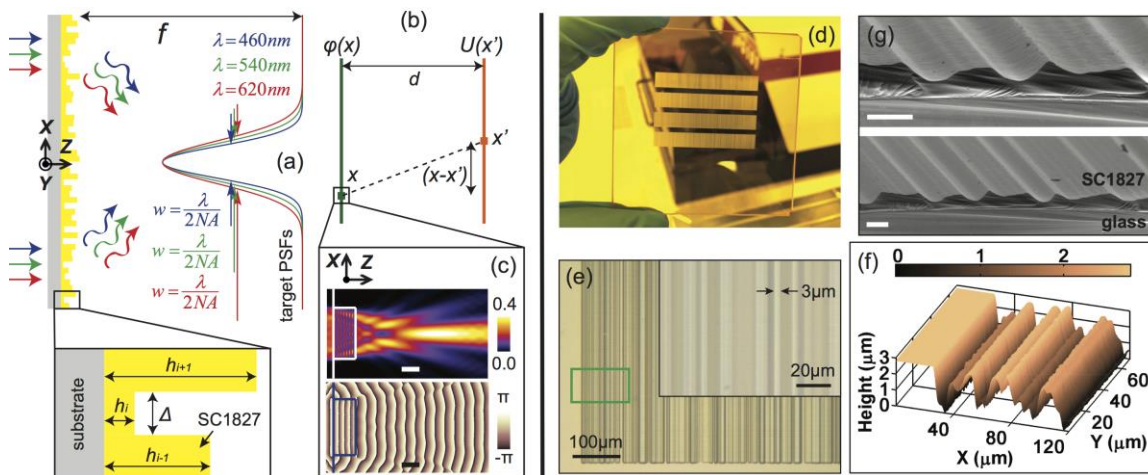

Figure 4.2. Structure and operation of the chromatic-aberration-corrected diffractive lens (CACDL) (a) Schematic of the CACDL with focal length, f. Our first set of CACDLs were designed to focus λ=460nm, 540nm and 620nm. The desired light-intensity distributions in the focal plane (or the point-spread functions or PSFs) are dictated by diffraction. This 1D CACDL is comprised of linear grooves with a designed height, h_i. SC1827 is the photoresist used for fabricating the CACDL. (b) Illustration of transformation from a CACDL point, x to the focus, x'. (c) Intensity (top) and phase (bottom) distributions of light (λ=540nm) diffracted by a single groove (width = 3μm, height = 1.2μm, scale bars: 1μm) simulated using FDTD. Linear polarization along X was assumed. (d) Photograph of four CACDLs patterned on a glass substrate. (e) Optical micrograph of a corner of one CACDL. Inset: magnified view. (f) Profilometer image of the region in the green box in (e). The maximum height is ~3μm. (g) Scanning-electron-microscopy images of the cross-sections of two CACDLs (scale bars: 5μm).
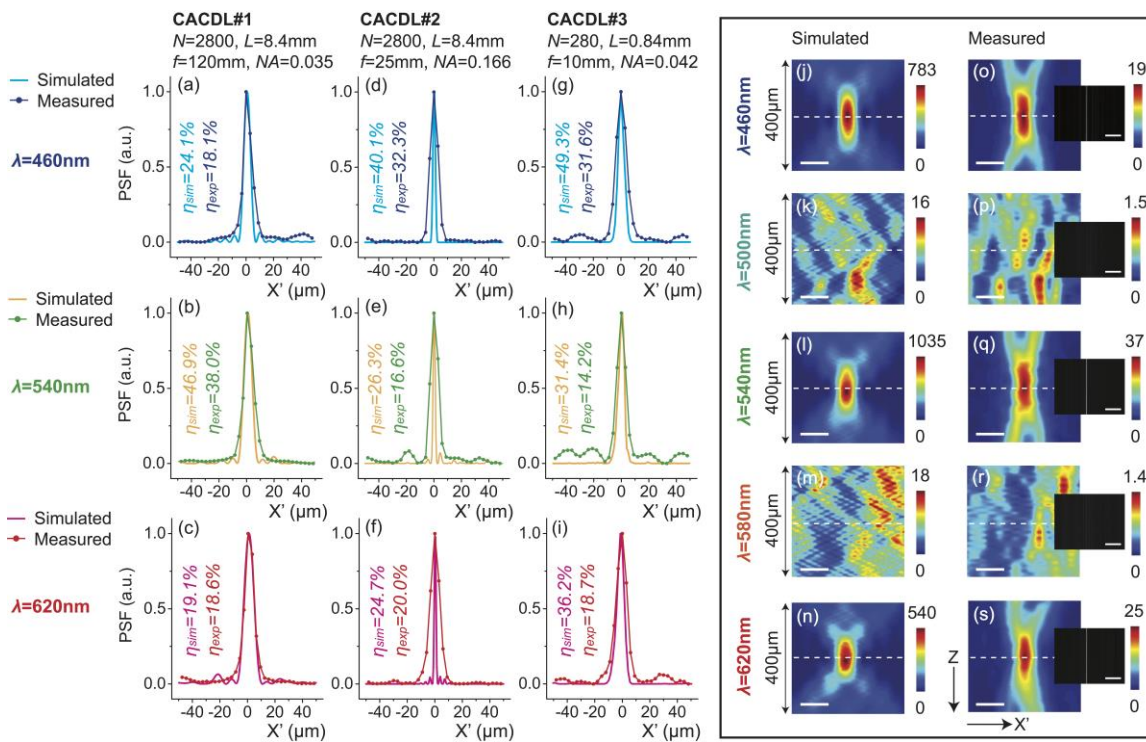
Figure 4.3. CACDLs for 3 discrete wavelengths (apochromats). The simulated and measured point-spread functions (PSFs) at λ=460nm ((a), (d) and (g)), λ=540nm ((b), (e) and (h)) and λ=620nm ((c), (f) and (i)). Each column represents one CACDL. Simulated ((j)-(n)) and measured ((o)-(s)) 2D PSFs of the first design for λ=460nm ((j) and (o)), 500nm ((k) and (p)), 540nm ((l) and (q)), 580nm ((m) and (r)) and 620nm ((n) and (s)) (scale bars: 20µm). Dashed-white lines denote the focal plane. Insets: grayscale images of the focal plane captured by a monochrome CMOS camera when illuminated by the discrete wavelengths from the VARIA filter (scale bars: 1mm, exposure time =3ms).
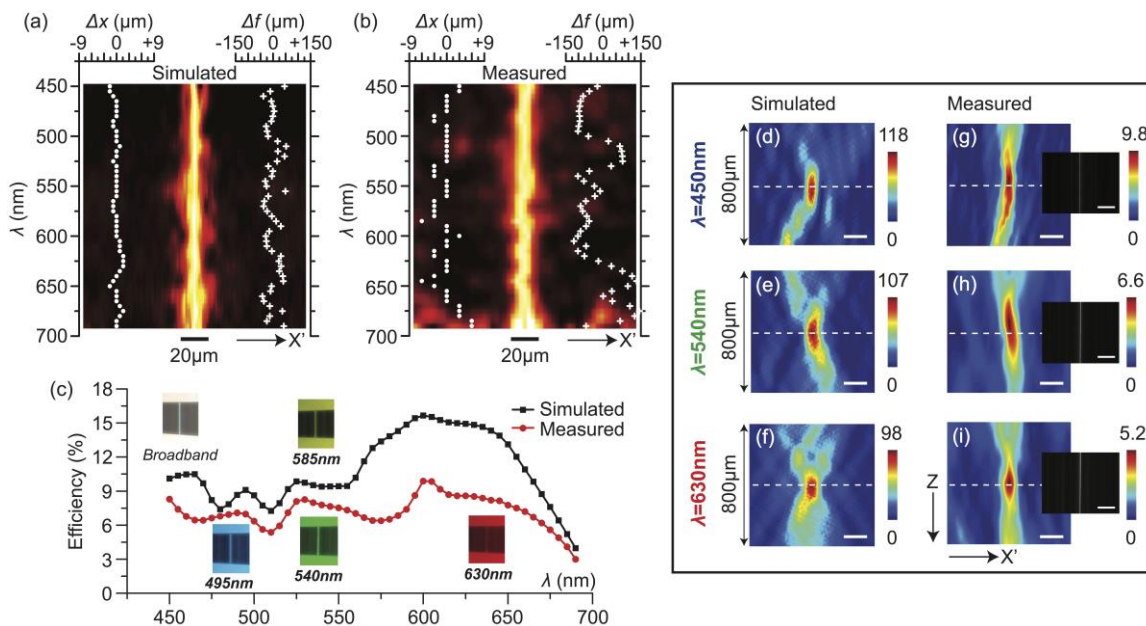
Figure 4.4. CACDL for broadband (450nm to 690nm) focusing (super-achromat). (a) Simulated and (b) measured 1D PSFs as a function of wavelength. Left insets: lateral-focus shift, Δx versus wavelength (white dots). Right insets: axial-focus shift, Δf versus wavelength (white crosses). (c) Simulated (black) and measured (red) optical efficiency as a function of wavelength. Insets: photographs of the focus on a white observation screen at various wavelengths. Simulated ((d)-(f)) and measured ((g)-(i)) 2D PSFs for λ=450nm ((d) and (g)), λ=540nm ((e) and (h)) and λ=630nm ((f) and (i)) (scale bars: 30µm). Dashed-white lines delineate the focus. Insets: images of the focus captured by a monochrome sensor (scale bars: 1mm). Exposure time t=4ms.
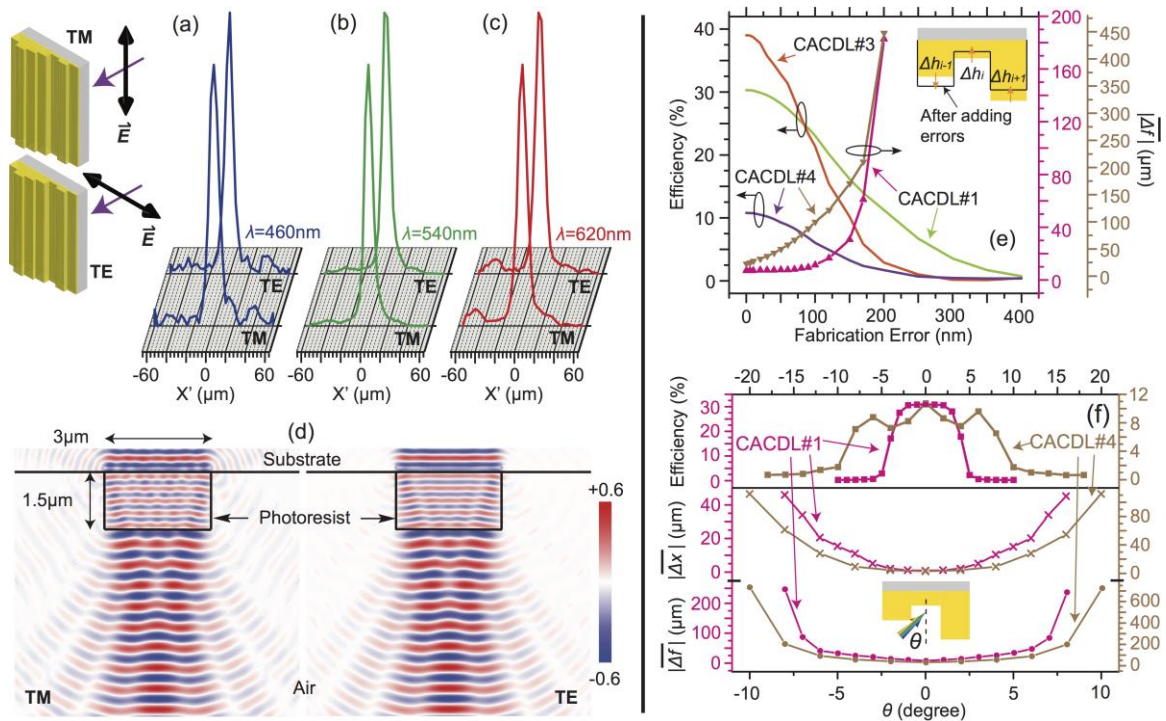
Figure 4.5. Impact of polarization, fabrication errors and oblique incidence. Measured PSFs of the CACDL#1 at the orthogonal polarizations for (a) λ=460nm, (b) λ=540nm and (c) λ=620nm. Inset: definitions of the incident polarization states. (d) Simulated electric-field distribution of light diffracted from one 3µm-wide and 1.5µm-high photoresist groove for TM (left) and TE (right) polarizations using FDTD. (e) Simulated wavelength-averaged optical efficiency (left Y-axis) and wavelength-averaged axial-focus shift (right Y-axis) as a function of fabrication errors. Inset: schematic showing how fabrication errors are applied. (f) Simulated wavelength-averaged optical efficiency (top) and wavelength-averaged lateral-focus shift (middle) and axial-focus shift (bottom) of two CACDLs as a function of the angle of incidence, θ. Middle and bottom panels share the same X coordinates. Inset: definition of θ.

4.7 References

[1] F. Aieta, M. A. Kats, P. Genevet, and F. Capasso, "Multiwavelength achromatic metasurfaces by dispersive phase compensation," Science **347**, 1342-1345 (2015).

[2] M. Born, and E. Wolf, *Principles of Optics: Electromagnetic Theory of Propagation, Interference and Diffraction of Light* (Cambridge University Press, 1999).

[3] F. W. Campbell, and R. W. Gubisch, "The effect of chromatic aberration on visual acuity," J. Physiol. **192**, 345-358 (1967).

[4] P. Ruffieux, T. Scharf, H. P. Herzig, R. Volkel, and K. J. Weible, "On the chromatic aberration of microlenses," Opt. Express **14**, 4687-4694 (2006).

[5] E. Lorenzo, "Chromatic aberration effect on solar energy systems using Fresnel lenses," Appl. Opt. **20**, 3729-3732 (1981).

[6] R. Menon, A. Patel, D. Gil, and H. I. Smith, "Maskless lithography," Materials Today **8**, 26-33 (2005).

[7] H-Y. Tsai, H. I. Smith, and R. Menon, "Reduction of focal-spot size using dichromats in absorbance modulation," Opt. Lett. **33**, 2916-2918 (2008).

[8] X. Wan, B. Shen, and R. Menon, "Diffractive lens design for optimized focusing," J. Opt. Soc. Am. A **31**, B27-B33 (2014).

[9] Thorlabs, Unmounted Achromatic Doublets, AR Coated: 400-700nm. (2015) Available at: http://www.thorlabs.us/newgrouppage9.cfm?objectgroup_id=120 .95

[10] A. Miks, and J. Novak, "Superachromatic air-spaced triplet," Appl. Opt. **53**, 6930-6937 (2014).

[11] Y-C. Fang, C-M. Tsai, J. MacDonald, and Y-C. Pai, "Eliminating chromatic aberration in Gauss-type lens design using a novel genetic algorithm," Appl. Opt. **48**, 2401-2410 (2007).

[12] N. Davidson, A. A. Friesem, and E. Hasman, "Analytic design of hybrid diffractive-refractive achromats," Appl. Opt. **32**, 4770-4774 (1993).

[13] A. Flores, M. R. Wang, and J. J. Yang, "Achromatic hybrid refractive-diffractive lens with extended depth of focus," Appl. Opt. **43**, 5618-5630 (2004).

[14] P. Valley, N. Savidis, J. Schwiegerling, M. R. Dodge, G. Peyman, and N. Peyghambarian, "Adjustable hybrid diffractive/refractive achromatic lens," Opt. Express **19**, 7468-7479 (2011).

[15] H. B. Wach, E. R. Dowski, and W. T. Cathey, "Control of chromatic focal shift through wave-front coding," Appl. Opt. **37**, 5359-5367 (1998).

[16] N. Yu, P. Genevet, M. A. Kats, F. Aieta, J-P. Tetienne, F. Capasso, and Z. Gaburro, "Light propagation with phase discontinuities: generalized laws of reflection and refraction," Science **334**, 333-337 (2011).

[17] A. V. Kildishev, A. Boltasseva, and V. M. Shalaev, "Planar photonics with metasurfaces," Science **339**, 1232009 (2013).

[18] F. Aieta, P. Genevet, N. Yu, M. A. Kats, Z. Gaburro, and F. Capasso, "Out-of-plane reflection and refraction of light by anisotropic optical antenna metasurfaces with phase discontinuities," Nano Lett. **12**, 1702-1706 (2012).

[19] X. Ni, A. V. Kildishev, and V. M. Shalaev, "Metasurface holograms for visible light," Nat. Commun. **4**:2807 1-6 (2013).

[20] B. Shen, P. Wang, R. Polson, and R. Menon, "An ultra-high efficiency metamaterial polarizer," Optica **1**, 356-360 (2014).

[21] P. Wang, J. A. Dominguez-Caballero, D. J. Friedman, and R. Menon, "A new class of multi-bandgap high-efficiency photovoltaics enabled by broadband diffractive optics," Prog. Photovolt: Res. Appl. **23**, 1073-1079 (2015).

[22] G. Kim, J. A. Dominguez-Caballero, and R. Menon, "Design and analysis of multi-wavelength diffractive optics," Opt. Express **20**, 2814-2823 (2012).

[23] P. Wang, and R. Menon, "Optical microlithography on oblique and multiplane surfaces using diffractive phase masks," J. Micro/Nanolith. MEMS MOEMS **14**, 02350796 (2015).

[24] P. Wang, and R. Menon, "Computational spectrometer based on a broadband diffractive optic," Opt. Express **22**, 14575-14587 (2014).

[25] M. D. Galus, E. Moon, H. I. Smith, and R. Menon, "Replication of diffractiveoptical arrays via photocurable nanoimprint lithography," J. Vac. Sci. Technol. B **24**, 2960-2963 (2006).

[26] L. J. Guo, "Recent progress in nanoimprint technology and its applications," J. Phys. D: Appl. Phys. **37**, R123-R141 (2004).

[27] P. Wang, and R. Menon, "Optimization of periodic nanostructures for enhanced light-trapping in ultra-thin photovoltaics," Opt. Express **21**, 6274-6285 (2013).

[28] W. H. Welch, J. E. Morris, and M. R. Feldman, "Iterative discrete on-axis encoding of radially symmetric computer-generated holograms," J. Opt. Soc. Am. A **10**, 1729-1738 (1993).

[29] T. R. M. Sales, and D. H. Raguin, "Multiwavelength operation with thin diffractive elements," Appl. Opt. **38**, 3012-3018 (1999).

[30] S. W. Kim, K. J. Yee, M. Abashin, L. Pang, and Y. Fainman, "Composite dielectric metasurfaces for phase control of vector field," Opt. Lett. **40**, 2453-2456 (2015).

CHAPTER 5

BROADBAND IMAGING WITH A DIFFRACTIVE LENS

This chapter is adapted from the following manuscript in preparation: Nabil Mohammad,

Xiaowen Wan, Peng Wang, and Rajesh Menon, "Broadband imaging with a single high

efficiency planar diffractive lens".

5.1 Abstract

We demonstrate imaging over the entire visible and near-IR spectrum using a single planar diffractive lens. This is enabled via multilevel diffractive optics with minimum feature width of 3µm and aspect ratio less than 0.5:1. We experimentally demonstrate focusing efficiency as high as 96%, operating bandwidth as high as 400nm (spanning visible and NIR bands), polarization insensitivity, and close to diffraction-limited performance. These planar diffractive lenses can be cost-effectively manufactured over large areas and, thereby, can enable the wide adoption of these thin, low-cost lenses for a variety of imaging applications.

5.2 Introduction

Refractive lenses are bulky and often challenging to incorporate into imaging systems that have restricted form factors. Diffractive optics, on the other hand, may be planar and lightweight [1]. However, conventional diffractive optics are not typically used for imaging because of significant off-axis and chromatic aberrations [2,3] as well as low broadband focusing efficiencies. Recently, planar metalenses have been used for imaging [4,5]. Unfortunately, metalenses require subwavelength features and large aspect ratios, making them impractical for low-cost manufacturing over large areas. In addition, they usually suffer from polarization sensitivity [6-8] and possess significant chromatic aberrations [9-13]. Here, we demonstrate that metalenses are not required for imaging light intensities, a scalar property of the electromagnetic field. Diffractive optics with super-wavelength features and relatively low aspect ratios, which are far simpler to fabricate, are sufficient for imaging light intensities. However, we note that metasurfaces are required to

manipulate vector properties of light such as polarization [14].

Previously, we utilized the concept of broadband diffractive optics to design broadband holograms [15] and to demonstrate broadband spectrum splitting and concentration [16,17], phase masks for 3D lithography [18] and cylindrical lenses with super-achromatic performance over the entire visible band [19]. Here, we design, fabricate and characterize broadband diffractive optics as planar lenses for imaging. We specifically created separate diffractive lenses with design wavelengths of $\lambda = 450$nm, 538nm, 610nm, 780nm and 850 nm. Each lens is comprised of square pixels of width $= 3\mu$m and the height of each pixel is varied between 0 and 1.4μm (see Figure 5.1(a)). For ease of fabrication, we decided to use lenses with 198 X 198 pixels (594μm x 594μm). The focal length, f and the numerical aperture (NA) of the lenses were f=2.9mm, NA=0.1 for design $\lambda = 450$nm, 538nm, 610nm, and f=2.2mm and NA=0.13 for design $\lambda = 780$nm, 850 nm. All design parameters are summarized in the supplementary information (Table 5.1). Recently, broadband diffractive lenses have been applied to imaging [20]. However, due to very low resolution of these lenses, significant image blurring is observed, which requires complex computational techniques to obtain sharp images. In contrast, our approach is able to maintain the quality of the images comparable to that achievable with more complex systems of lenses as evidenced by the point-spread function (PSF), the modulation-transfer function (MTF) and the exemplary images described below.

5.3 Principle of Operation

The diffractive lens can be accurately modeled by scalar diffraction theory in the regime of Fresnel approximation [21,22]. We utilized a modified version of direct-binary

search to optimize the height profile of each lens. Details of the design process have been described elsewhere [19]. The on-axis focusing efficiency is used as the metric for optimization. Nevertheless, the off-axis performance of these lenses is sufficient to form good quality images.

The optimized height profile for one of the lenses (design $\lambda = 450$nm) is shown in Figure 5.1(b). Grayscale lithography was used to fabricate the lenses in a positive photoresist (Shipley 1813) spin coated on a glass substrate. The lens was fabricated in an array fashion (10X8). Details of the design and fabrication process are described in the supplementary information. Optical micrographs of the fabricated lens are shown in Figure 5.1(c) (where a 3 X 3 lens array is visible), in Figure 5.1(d) (one lens) and in Figure 5.1(e), where an atomic-force micrograph of a small region is shown. Details of the remaining four lenses including designs and micrographs are included in the supplementary information. Figure 5.1(f) shows a schematic of our setup to characterize the lenses. For each lens, we image an object, the US AirForce target with a diffuser onto a monochrome sensor (The Imaging Source, DMM 27UP031-ML).

5.4 Experiments and Results

To experimentally demonstrate the focusing performance of each lens, we first illuminated each lens using a spatially collimated beam from a super-continuum source equipped with a tunable band-pass filter. Details of this illumination setup have been described previously [19]. Note that the illumination is randomly polarized. The light distribution at the focus for each lens was then magnified by an objective-tube lens system and recorded on a monochrome sensor (see supplementary information for details). For

each lens, the center wavelength of the illumination corresponded to the design wavelength and the bandwidth was varied from 10nm to 200nm. The incident spectra for these bandwidths are included in the supplementary information. The simulated and measured focal spots for the lens designed for λ=450nm are shown in Figure 5.2. Excellent agreement between simulation and measurement is obtained. The focusing efficiency, defined as the ratio of the integrated power over a circular aperture with diameter 3 times full-width at half-maximum (FWHM) in the focal plane to the total power over the sensor area is also measured and simulated. Details are included in the supplementary information. As expected, increasing the illumination bandwidth decreases focusing efficiency and increases the FWHM. Results for bandwidth equal to 200nm are included in the supplementary information. In some cases, the measured efficiency is slightly higher than the simulated one. This is because the experimental focal spot is not perfectly centered on the sensor and the sensor area is slightly smaller than the lens aperture. The measured FWHM at bandwidth of 10nm is about 3.3µm, which is close to the diffraction limited simulated value. Similar good agreement between simulation and experiments are observed for the other four lenses as well and these results are included in the supplementary information.

The modulation-transfer function (MTF) of each lens can then be computed as the absolute value of the Fourier transform of the measured point-spread function (PSF). The MTF is plotted for the 4 illumination bandwidths in Figure 5.2(m) for X and in Figure 5.2(n) for Y directions, respectively. The resolution typically defined as the spatial frequency at 10% MTF is plotted as a function of illumination bandwidth in Figure 5.2(o). The resolution decreases with bandwidth as expected, but still maintains a value of about

200 cycles/mm even with a bandwidth of 200nm.

From this analysis, we expect each of our lenses to be able to image over the entire visible range even though it was designed for one wavelength. To demonstrate this imaging capability, we used a standard test chart (USAF 1951) with a diffuser behind it as the object and imaged it onto the same monochrome sensor using each flat lens as illustrated earlier in Figure 5.1(f). The object distance, d_0 and the image distance, d_i were 104mm and 2.98mm for lenses designed for λ=450nm, 538nm and 610nm, and 93mm and 2.2mm for lenses designed for λ=780nm and 850nm, respectively. This follows the simple imaging relation, $1/d_0+1/d_i=1/f$. Note that only a single flat lens is used. This is in contrast to previous work, where a pair of metalenses was used to correct for chromatic aberrations [4].

We used the same illumination source as was used for focal spot characterization. In order to demonstrate broadband imaging, we first kept the illumination bandwidth at 10nm and varied the center wavelength from λ_d-50nm to λ_d+50nm for each lens, where λ_d is the corresponding design wavelength. The results are summarized in Figure 5.3(a). Each lens is able to form good quality images over the entire wavelength range. Note that our optics does not transmit light beyond about 850nm, and therefore illumination beyond 850nm was not possible. We also note that the illumination intensity for wavelengths below 410nm is quite low, which explains the low brightness in the first two images for lens designed for 450nm. Next, we illuminated each lens with spectra of increasing bandwidth from 10nm to 400nm with the center wavelength equal to the corresponding design wavelength. The corresponding incident spectra are included in the supplementary information. All lenses except the one designed for 850nm perform well even at a

bandwidth of 400nm, which was the largest bandwidth that we could test. All the corresponding incident spectra are included in the supplementary information. Note that no postprocessing algorithms, such as denoising or distortion-correction, are applied to these raw images.

Finally, we performed a test using a halogen lamp to illuminate the target to demonstrate imaging over the entire visible and near-IR range. The image was obtained with the lens designed for 538nm and the results are summarized in Figure 5.3(b). The spectrum of the illumination is shown on the left and the image of the target region is shown next to it. These results clearly demonstrate good quality imaging with a single planar diffractive lens over the visible and near-IR spectral range. It is possible to improve the performance of this single lens by imposing designing the lens for full-spectrum (broadband) focusing [15,19,22].

The diffractive lens is also polarization-insensitive [19]. Finite-difference-time-domain (FDTD) simulations of a single pixel show that the intensity is the same for illumination at either of two orthogonal linear polarization states (see supplementary information). This ensures that the lenses perform equally well for any polarization input, which is important for general imaging applications. Furthermore, all experiments reported here were conducted with randomly polarized incident light.

5.5 Conclusions

We show here that planar diffractive lenses, when designed properly, are sufficient for broadband imaging. For ease of fabrication, we chose to demonstrate lenses with relatively low numerical aperture (NA) or large F/# and a small aperture. It is possible to

overcome these limitations with improved fabrication processes. In a diffractive lens, the maximum achievable NA is determined by $\lambda/(2*w)$, where w is the minimum pixel width (constrained by fabrication). In order to achieve NA comparable to that of a mobile-phone camera (NA~0.3), one needs w ~0.83µm. We can expect the maximum pixel height to be similar to what we have used here, 1.4µm. This means that for many photography applications, a diffractive lens would need an aspect ratio of only 1.7. This is considerably simpler to fabricate than a visible-wavelength metalens, where feature widths of <50nm and aspect ratios>15 are required [5]. By extending the fabrication process to industry-relevant lithographic scales and large area replication via nanoimprinting, [23] it is possible to envision planar lenses enabling imaging with very thin form factors, low weights and low costs.

5.6 Supplementary Information

5.6.1 Design Parameters

These lenses are essentially pixelated structures in both X and Y directions (Figure 5.1(a)). Each pixel has a width of 3 µm and the height is quantized into multiple levels. The maximum height is 1.4µm. Each lens has 198 pixels X 198 pixels leading to a dimension of 594µm x 594µm. All the design and geometric parameters of five lenses are summarized in Table 5.1. Design heights of the four lens designs (538nm, 610nm, 780nm and 850nm) and optical micrographs of the corresponding fabricated lenses are shown in Figure 5.4.

5.6.2 Fabrication

In grayscale lithography, the laser intensity is modulated as it is scanned across the surface of a photoresist [24]. This leads to multilevel structures after development. This involves three steps: calibration, conversion of design heights into grayscale map and fabrication of final device. The purpose of calibration is to correlate the gray levels (which modulates the exposure dose) with the exposed depths. For calibration, a 3 inch X 3 inch glass substrate was RCA cleaned. A positive photoresist Shipley 1813 [25] was spin coated on the glass substrate at 1000 rpm. The sample was then baked in an oven at 110° C for 30 minutes. A calibration design was exposed on the sample using the Heidelberg Micro Pattern Generator 101 tool [26]. A stylus profilometer was used to measure the exposed depths at different gray levels. The calibration data were then used to convert the design heights into a grayscale map. This grayscale map was finally used to write the final device.

5.6.3 Focal Spot Characterization Setup

The flat lenses were illuminated with expanded and collimated beam from a SuperK EXTREME EXW-6 source and the SuperK VARIA filter. The wavelength and bandwidth can be changed using the VARIA filter. The focal plane of the flat lenses were magnified using an objective (RMS20X-PF, Thorlabs) and tube lens (ITL200, Thorlabs) and imaged onto a monochrome sensor (DMM 27UP031-ML, Imaging Source). The setup is shown in Figure 5.5. Here, f represents the focal length of the flat lens and w.d. (roughly 2mm) is the working distance of the objective. The gap between objective and tube lens was ~90 mm and that between the sensor and the backside of tube lens was about 148mm. The magnification of the objective-tube lens was 22.22X.

To experimentally determine the focusing efficiency, from the PSF images captured by the sensor, the ratio of the intensity integrated over the circular aperture (centered at the peak of the psf and diameter equal to 3*FWHM) to the intensity integrated over the full sensor area was calculated. Note that the sensor area does not cover magnified image corresponding to the full lens aperture. Another limitation is the 8 bit dynamic range of the sensor, which is discussed below.

5.6.4 Calculation of Focusing Efficiency

Note that a correction step is required to calculate efficiency in simulation, to account for the quantization error in digital semiconductor sensors. For instance, simulation gives average background values of 0.00001 (normalized to peak) all over the 2D simulation space. For an 8-bit sensor with maximum 256 grayscale levels, this background is well below its detection limit ($1/256 = 0.0039$), and therefore doesn't contribute to total energy in efficiency calculation. As a result, the simulated intensity distributions are first quantized to 256 grayscale levels and then their efficiencies are calculated based on the definition above. Moreover, since the FOV of the sensor used in experimental measurements is 256.63um X 192.48um, which is smaller than the 0.594 mm $\times$ 0.594 mm (Table 5.1), only the integrated power within the 256.63um X 192.48um center area is accounted for the denominator in efficiency calculation. That means, lens aperture is reduced due to the limited FOV of the sensor. Efficiencies calculated with these corrections considered are given in Figure 5.2. The simulation results for focusing by the five lenses are summarized in Tables 5.2 and 5.3 below.

5.6.5 Imaging Setup

For imaging experiment, the 1951 USAF resolution test chart (R3L3S1N, Thorlabs) was used as the object. The flat lenses were used for imaging the object on to the sensor. A diffuser was placed behind the USAF target. Since the each design was fabricated in an array (10X8) and the field of view was small, only a part of the USAF target was used for imaging at a time. Figure 5.6 shows the imaging setup. For all imaging experiments, gain was zero. For imaging at the design wavelength, same exposure time was used for all parts of USAF target. For imaging at different bandwidths and wavelengths, different exposure times were used to ensure that the images do not get saturated.

5.6.6 Illumination Spectra of the Super-continuum Source

The incident spectra centered at the five design wavelengths are shown in Figures 5.8-5.12 for bandwidths of 10nm, 50nm, 100nm, 200nm, 300nm and 400nm. Wavelengths from 350nm to 850 nm are available from the VARIA filter. To accommodate the specific bandwidth of the illumination spectra, the center wavelengths were shifted in the cases where the design wavelengths are close to the bandwidth limit of the VARIA filter. For example, in case of lens with 450nm design wavelength, the center wavelength in the illumination spectra was set to 550nm to obtain 400nm bandwidth.

5.6.7 Focal Spots at Different Bandwidths

Light intensity distribution at focus for lens designs 538nm, 610nm, 780nm and 850 nm are shown in Figures 5.13-5.17.

5.6.8 Images of the USAF Target at the Design Wavelengths

For this experiment, each flat lens design was used to image the USAF target. The target was illuminated with the corresponding design wavelength of light with 10nm bandwidth. The results are shown in Figures 5.18-5.22. The patterns of the USAF target are categorized into ten groups (-2,-1,0,1,2,3,4,5,6,7). Each group has six elements. The images below are labeled with the corresponding group number followed by the element number. Each image in the top row consist of a single element of group 2. The images in the middle row corresponds to group 1. In this case, some images consist of multiple elements. The label on top of the images corresponds to the central patterns. The rest of the groups with corresponding elements are shown in the bottom row.

5.6.9 Polarization Independence

In order to demonstrate that our diffractive lens is polarization-insensitive, we simulated the diffraction field of one single square pixel by 3D finite-difference-time-domain (FDTD). The pixel has dimension of 3µm × 3µm × 1µm (width in X direction, width in Y direction and height in Z direction). Its refractive index is extracted from the dispersion of Shipley 1813 photoresist measured by Ellipsometer. The substrate is assumed BK7 glass. Two wavelengths 538nm and 850nm are simulated. Two linear polarizations, along X and Y directions, respectively, are simulated. Light propagates in Z direction and Z=0 is the front pixel-air interface. Figure 5.23 summarizes the FDTD results. As expected, two polarization states (Ex and Ey) show very close electric fields for two wavelengths at two cross-section planes. This demonstrates that our diffractive lens is indeed polarization-insensitive.

5.7 Author Contributions

R.M., P.W. and N.M. conceived and designed the experiments. P.W. modeled, optimized and characterized the devices. X.W. did the simulations. N.M. fabricated the devices, performed the experiments and numerical analysis. N.M. and R.M. analyzed the data and wrote the paper.
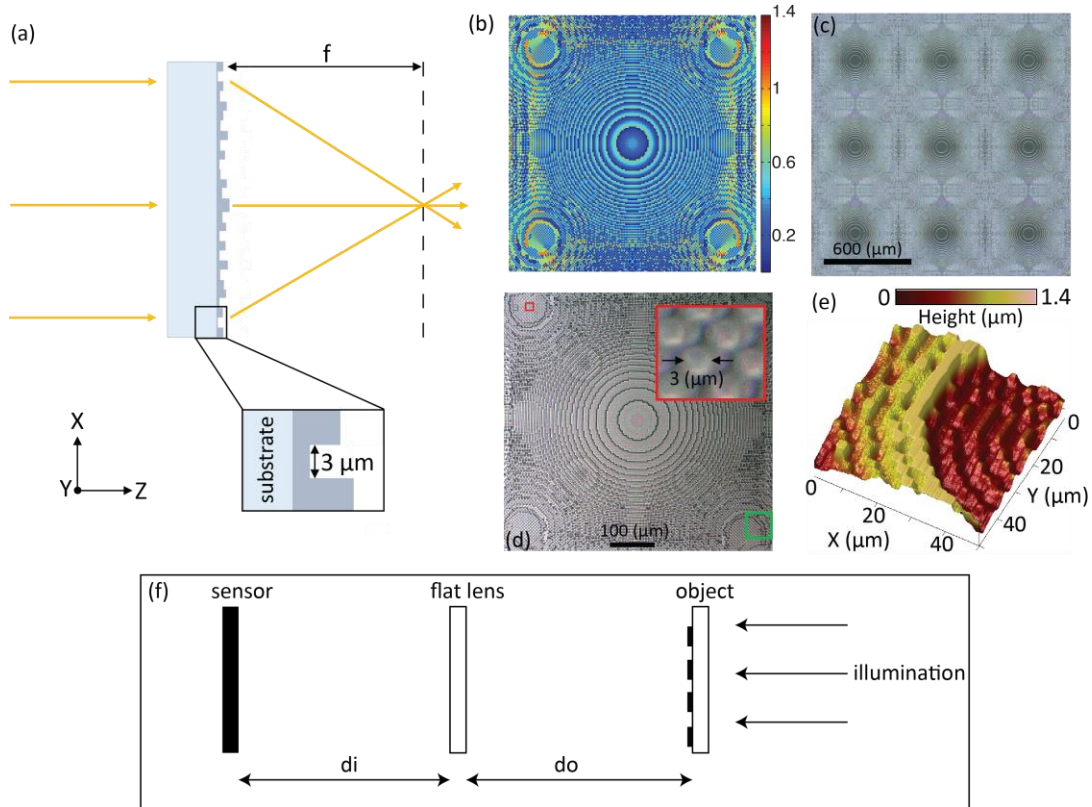
Figure 5.1. Structure and operation of the flat-lens. (a) Schematic of a flat-lens design. The structure is pixilated in both X and Y directions. For simplicity, a cross-section in the X-Z plane is shown. (b) Height profile of the lens designed for λ=450 nm. The height varies from 0 to 1.4µm. (c) An optical micrograph of a 3X3 array of lenses. (d) Optical micrograph of one lens. Inset: magnified view of the region indicated by the red square. (e) AFM measurements of a 50µm X 50µm area (green square in Fig. 1d). (f) Schematic of our imaging experiment. The USAF target with a diffuser is used as the object in transmission.
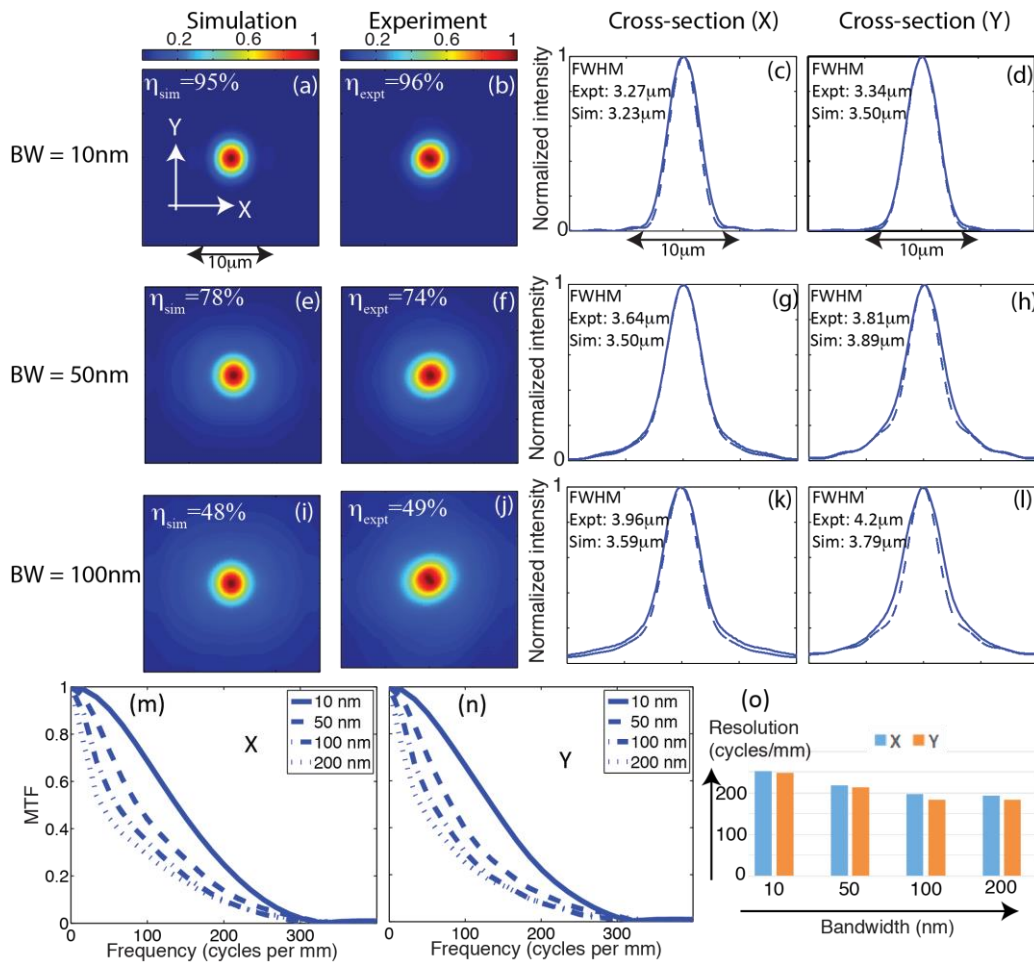
Figure 5.2. Light intensity distribution at focus (or point-spread function) for lens with design λ= 450nm. (a) Simulated focal spot.Fi (b) Measured focal spot. Cross-section through focal spot in (c) X and (d) Y directions (simulation is shown with dashed lines). The illumination bandwidth is 10nm. The corresponding results for bandwidths of 50nm and 100nm are shown in (e)-(l). Modulation-transfer function (MTF) in (m) X and (n) Y directions for various illumination bandwidths. (o) The resolution obtained at 10% contrast is plotted as a function of illumination bandwidth.
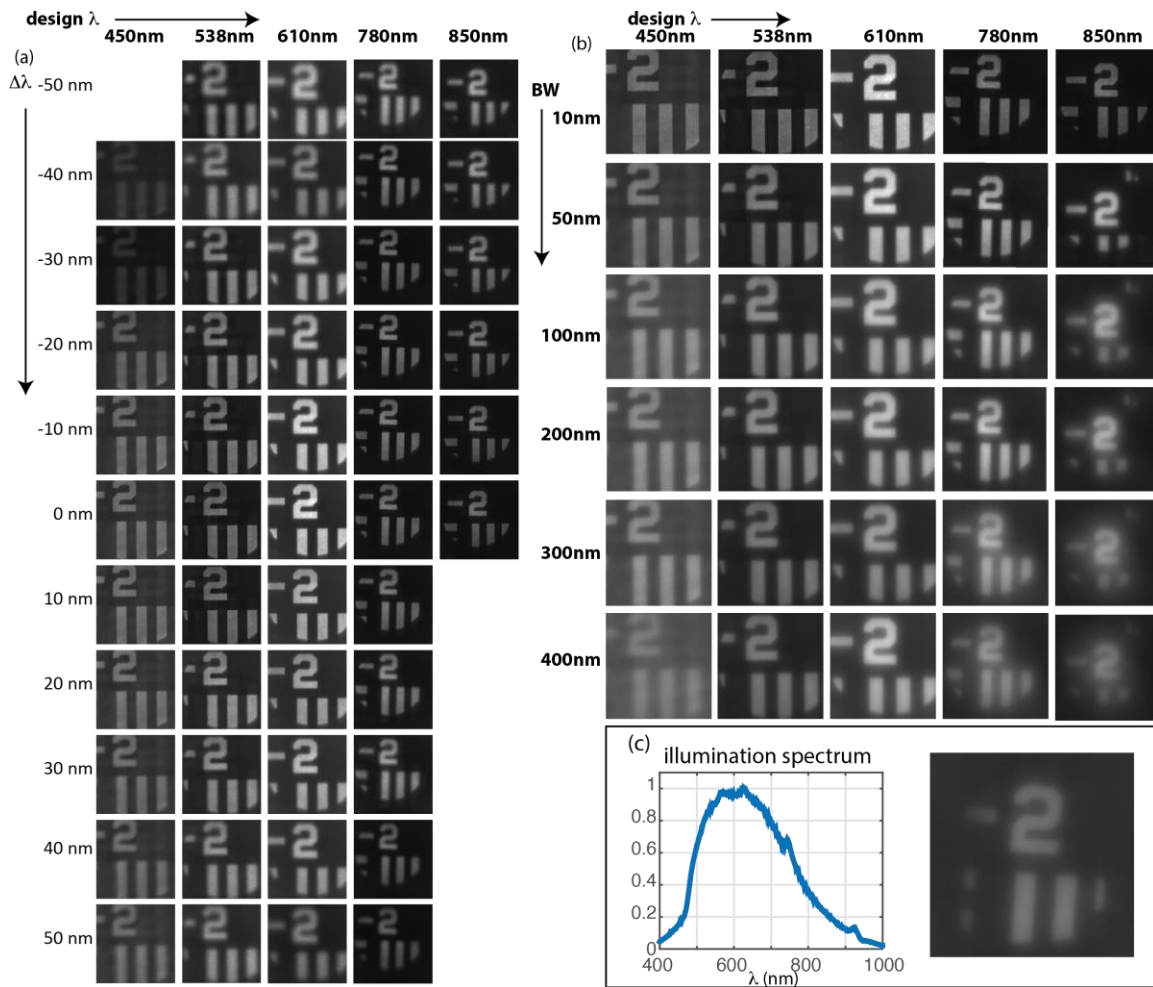
Figure 5.3. Imaging with the flat lenses. (a) Imaging wavelengths different from the design wavelength. Δλ is the shift between the illumination center and the design wavelengths. The bandwidth is 10nm. (b) Imaging with broadband illumination. The center wavelength is the design wavelength (except for design λ=850nm) and bandwidth is indicated on the left column. The center wavelength was shifted to accommodate the full spectrum for the bandwidths equal to 300nm and 400nm in the case of design λ=850nm. (c) Imaging with visible and near-IR spectrum from a halogen lamp. Left: Measured incident spectrum. Right: Image of target region.
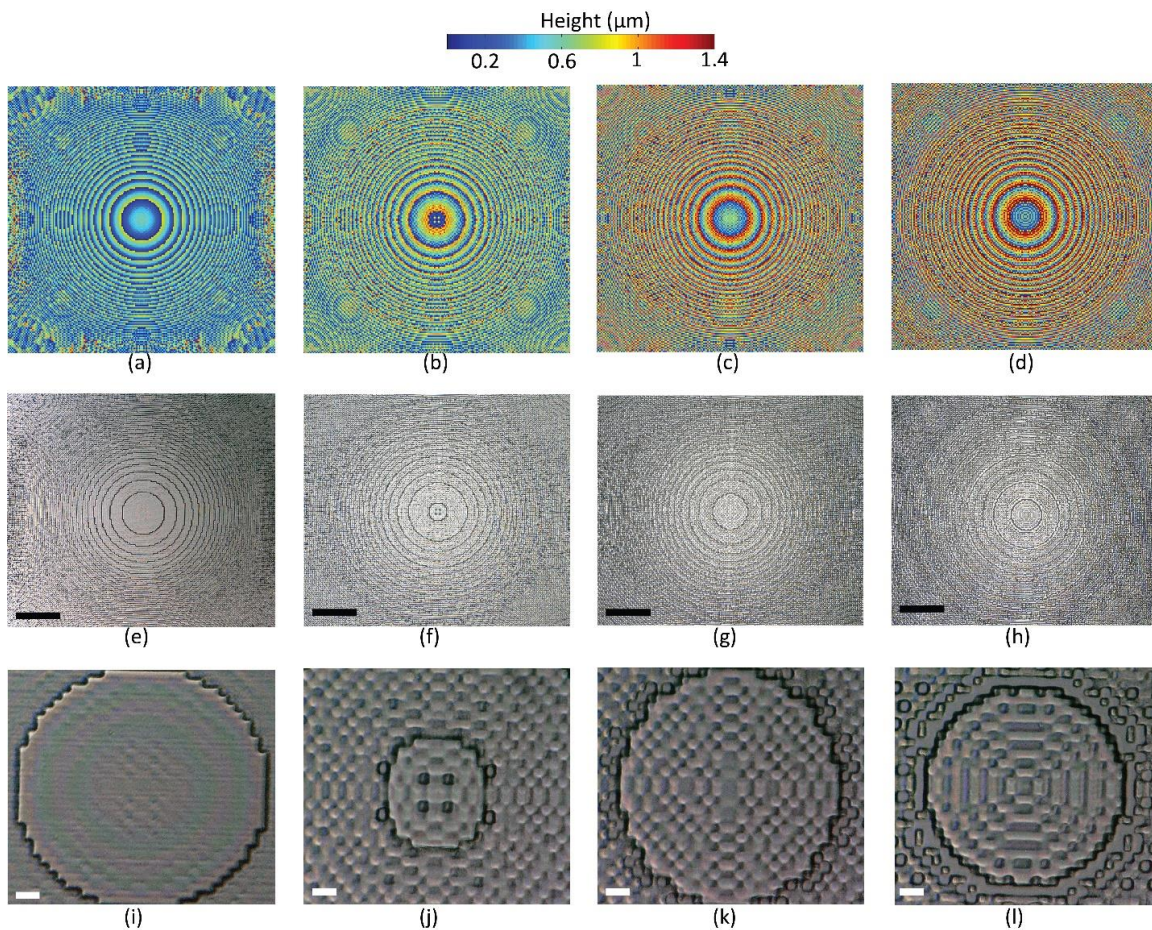
Figure 5.4. Height profile and optical micrographs of the lenses. (a)-(d) Height profile of four lens designs (L2, L3, L4, L5). The color bar for all 4 designs are shown on the top. The height varies from 0 to 1.4 µm. (e)-(h) Corresponding optical micrographs of the fabricated designs. Scale bar: 100 µm. (i)-(l) Magnified optical micrographs of the central regions of (e)-(h). Scale bar: 10 µm.
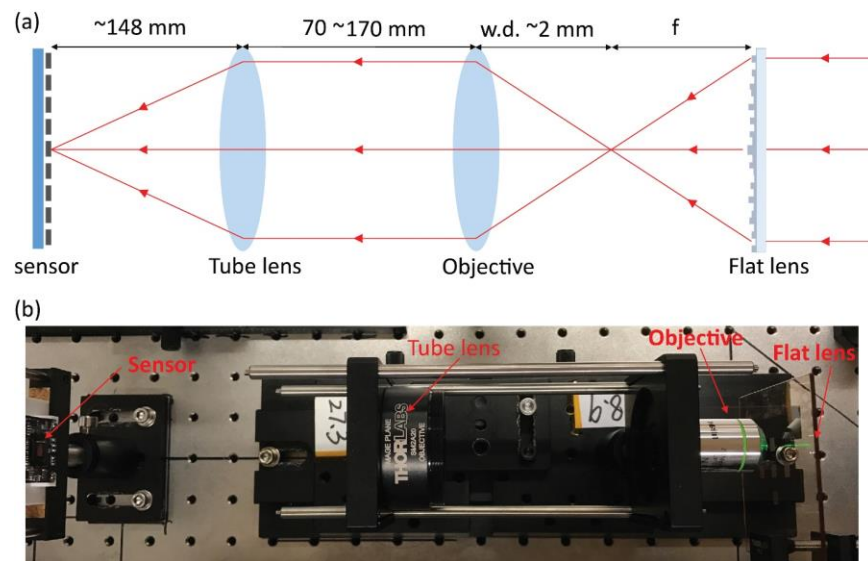
Figure 5.5. Experimental setup for focal spot characterization. (a) Schematic of the setup. (b) Photograph of the setup.
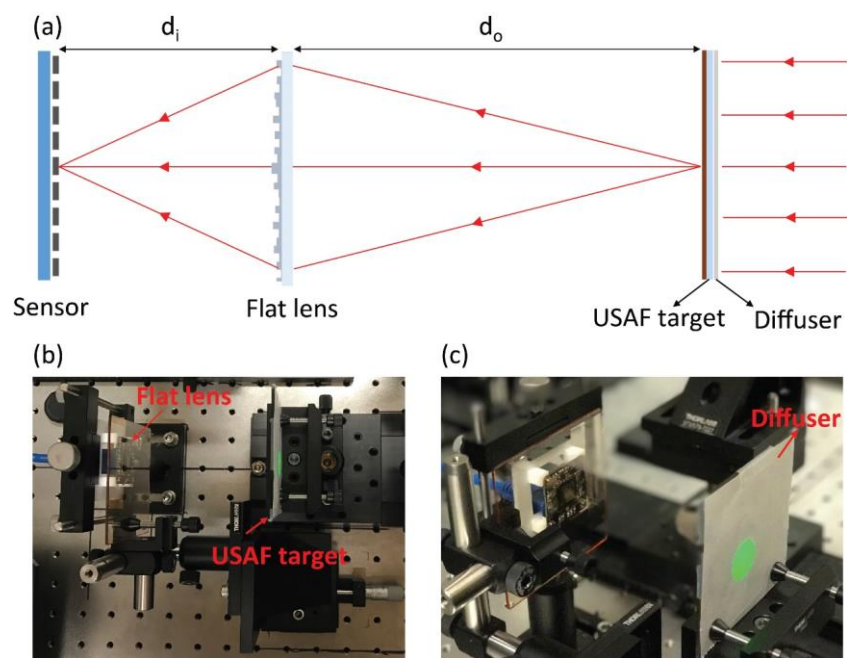

Figure 5.6. Experimental setup for imaging. (a) Schematic of the setup. (b) and (c) Photographs of the setup.

Figure 5.7 Photograph of 1951 USAF test resolution chart (R3L3S1N) from Thorlabs [27].
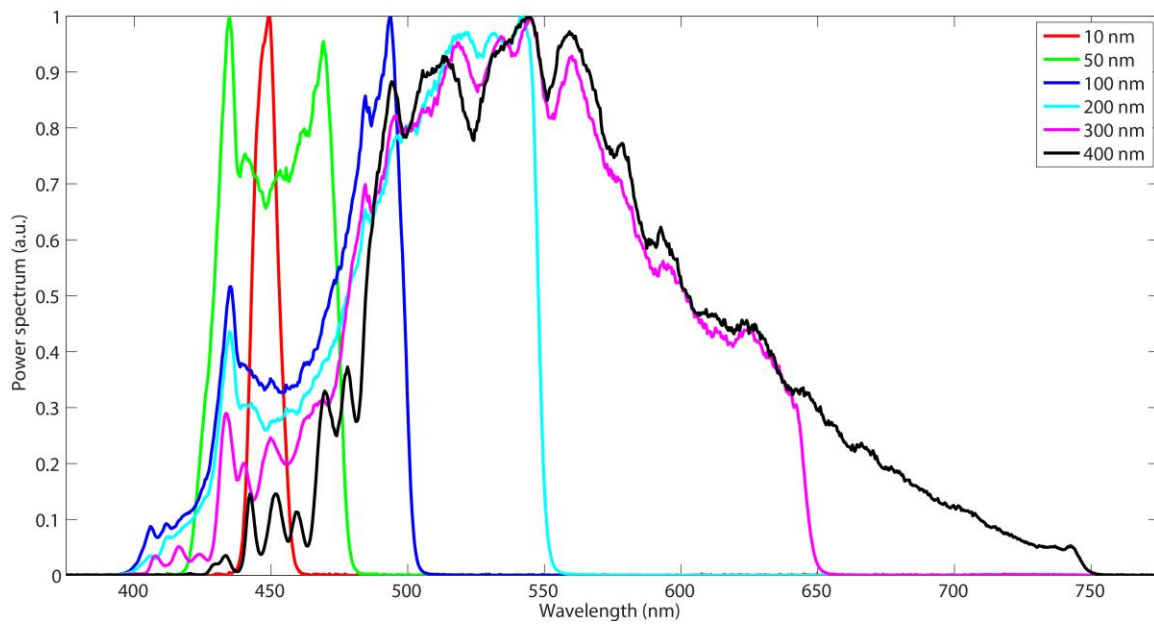

Figure 5.8. Illumination spectra for lens designed for 450nm.
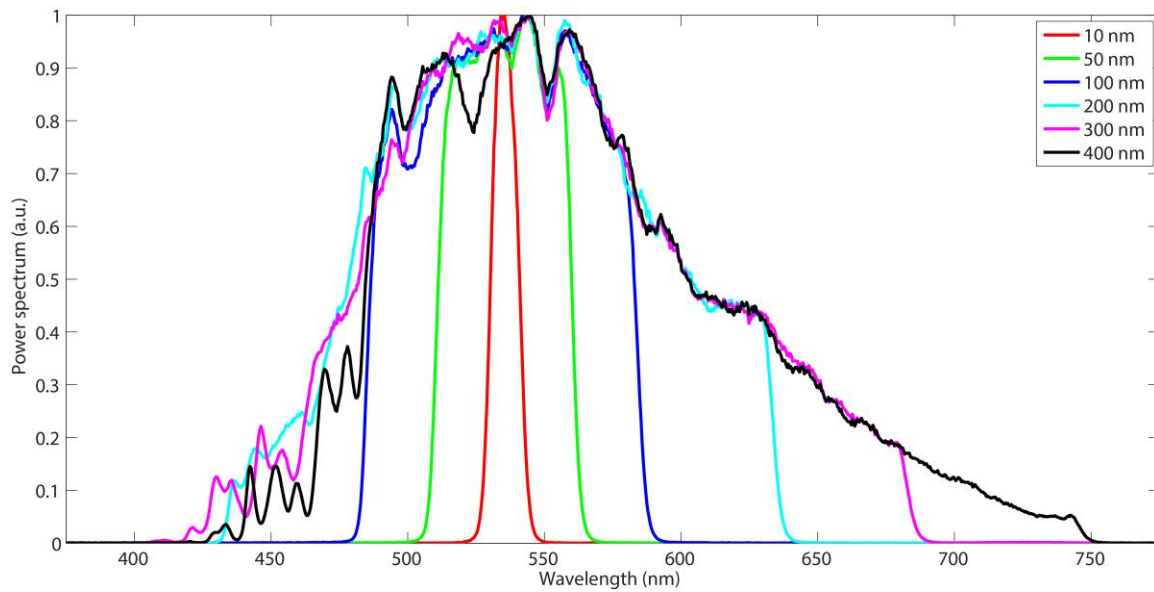
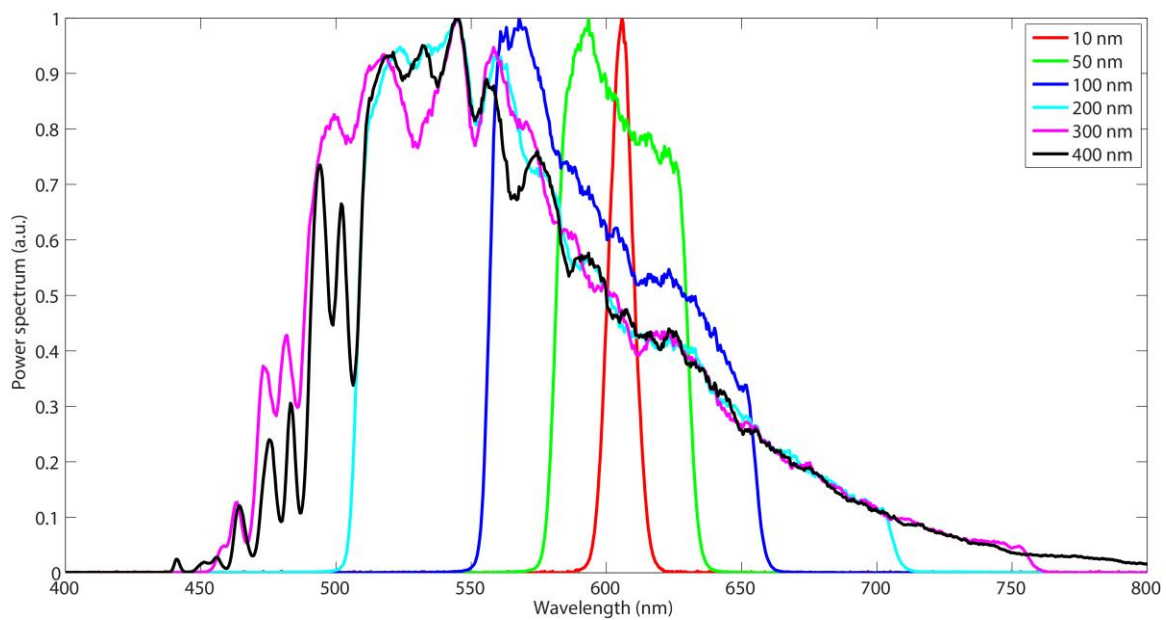Figure 5.9. Illumination spectra for lens designed for 538nm.

Figure 5.10. Illumination spectra for lens designed for 610nm.
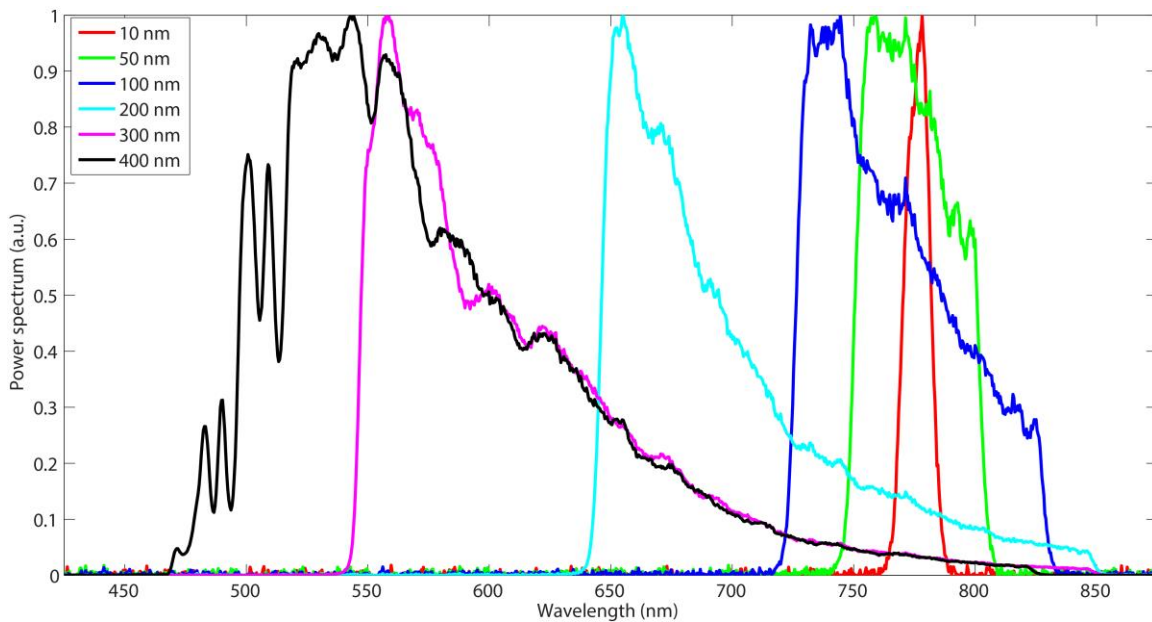
Figure 5.11. Illumination spectra for lens designed for 780nm.
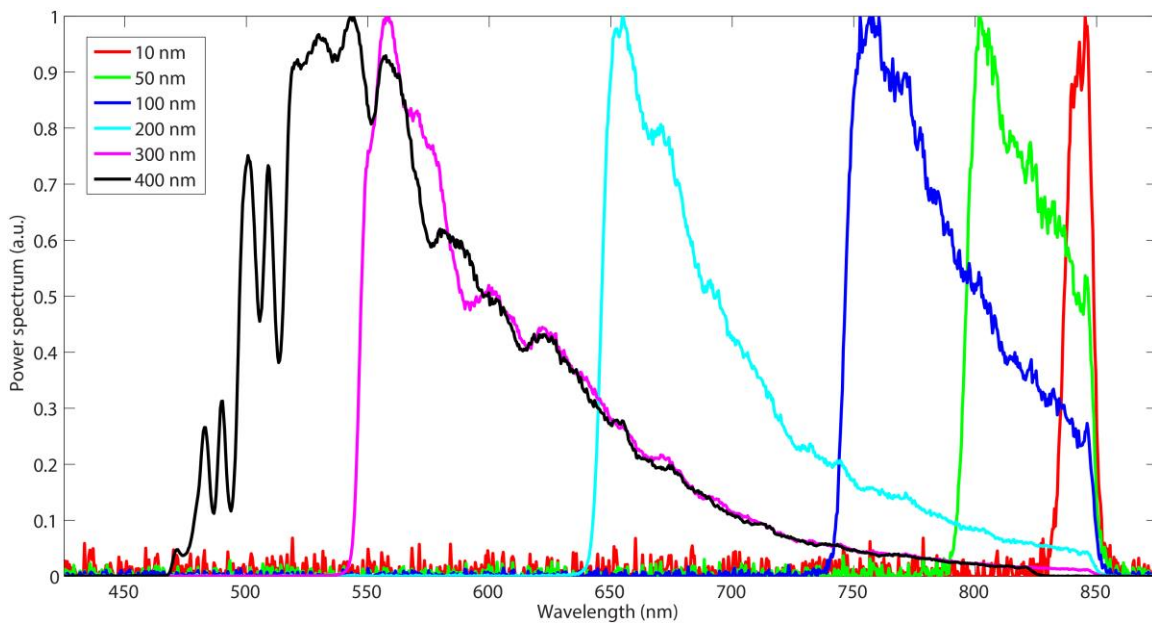
Figure 5.12. Illumination spectra for lens designed for 850nm.

Figure 5.13. : Light intensity distribution at focus (or point-spread function) for lens with design λ = 538nm. (a) Simulated focal spot. (b) Measured focal spot. Cross-section through focal spot in (c) X and (d) Y directions (simulation is shown with dashed lines). The illumination bandwidth is 10nm. The corresponding results for bandwidths of 50nm and 100nm are shown in (e)-(l).
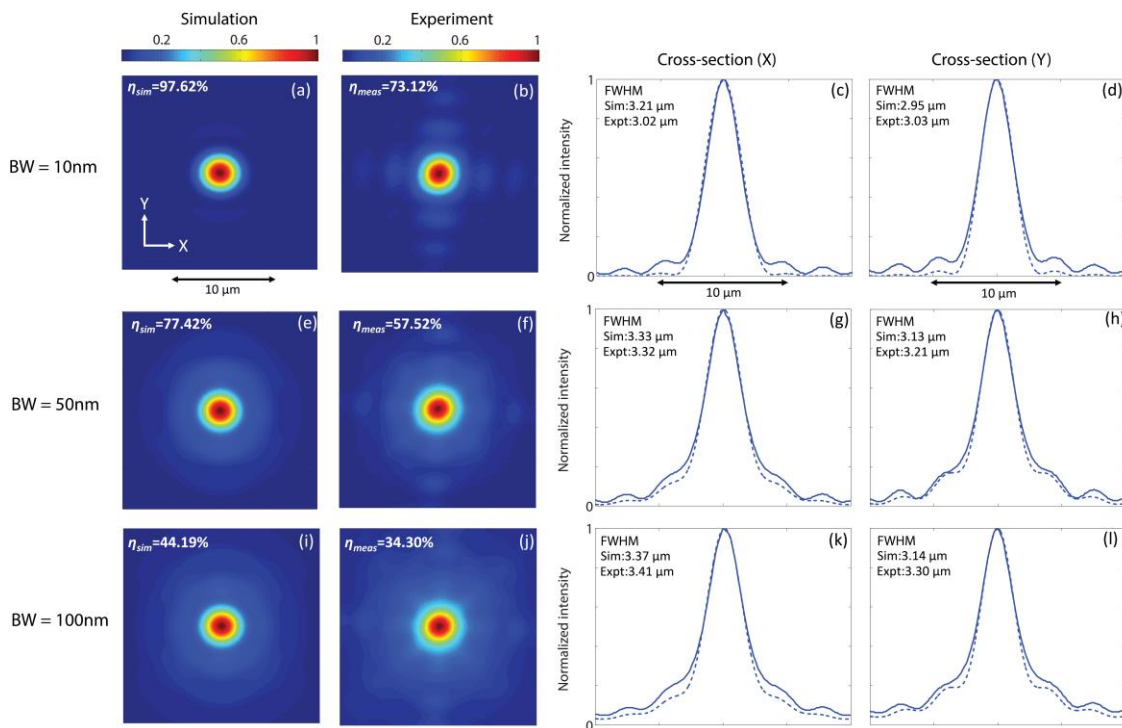
Figure 5.14. Light intensity distribution at focus (or point-spread function) for lens with design λ = 610nm. (a) Simulated focal spot. (b) Measured focal spot. Cross-section through focal spot in (c) X and (d) Y directions (simulation is shown with dashed lines). The illumination bandwidth is 10nm. The corresponding results for bandwidths of 50nm and 100nm are shown in (e)-(l).
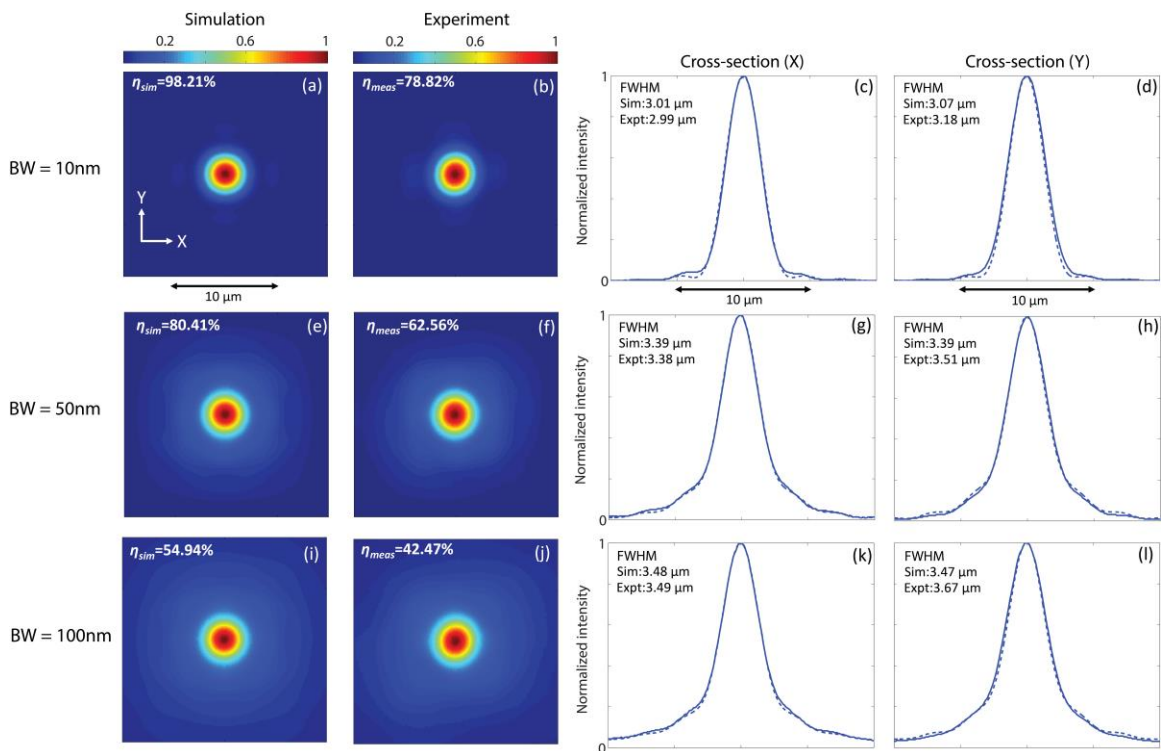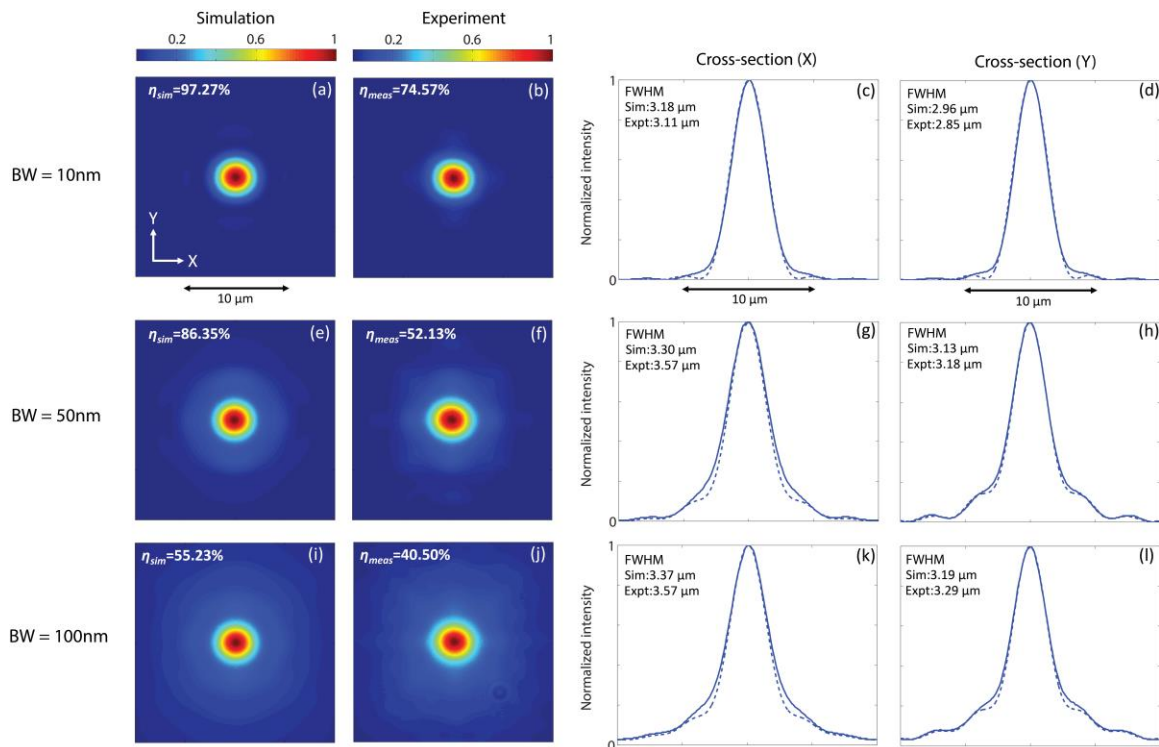
Figure 5.15. Light intensity distribution at focus (or point-spread function) for lens with design λ = 780nm. (a) Simulated focal spot. (b) Measured focal spot. Cross-section through focal spot in (c) X and (d) Y directions (simulation is shown with dashed lines). The illumination bandwidth is 10nm. The corresponding results for bandwidths of 50nm and 100nm are shown in (e)-(l).
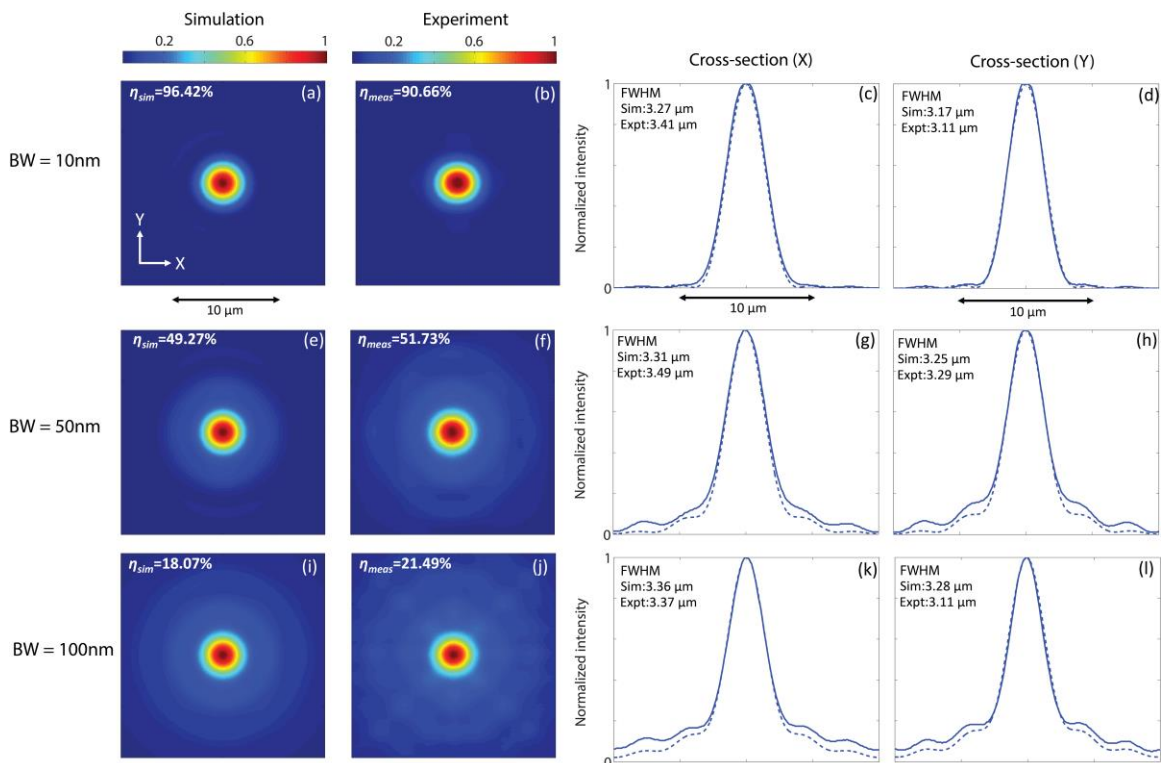
Figure 5.16. Light intensity distribution at focus (or point-spread function) for lens with design λ = 850nm. (a) Simulated focal spot. (b) Measured focal spot. Cross-section through focal spot in (c) X and (d) Y directions (simulation is shown with dashed lines). The illumination bandwidth is 10nm. The corresponding results for bandwidths of 50nm and 100nm are shown in (e)-(l).

- FWHM in x: 3.5 μm
- FWHM in y: 3.7 μm
- Efficiency: 29%
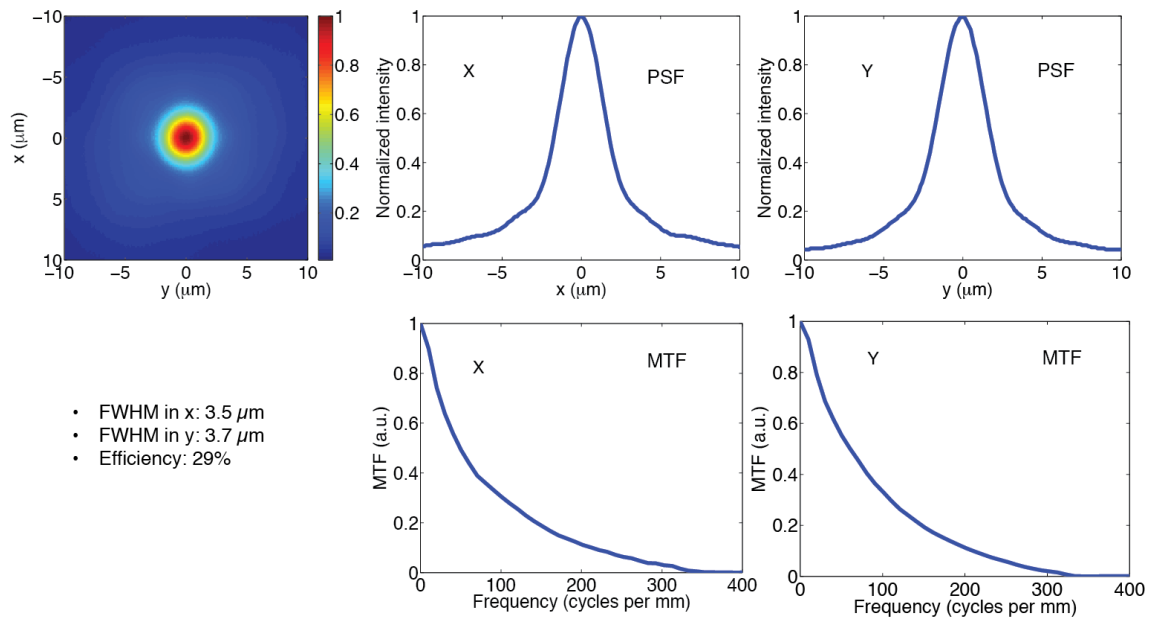
Figure 5.17. Experimental results of focusing with lens design for 538nm with illumination bandwidth of 200nm. This is a continuation of the results presented in Figure 5.2 of the main text.
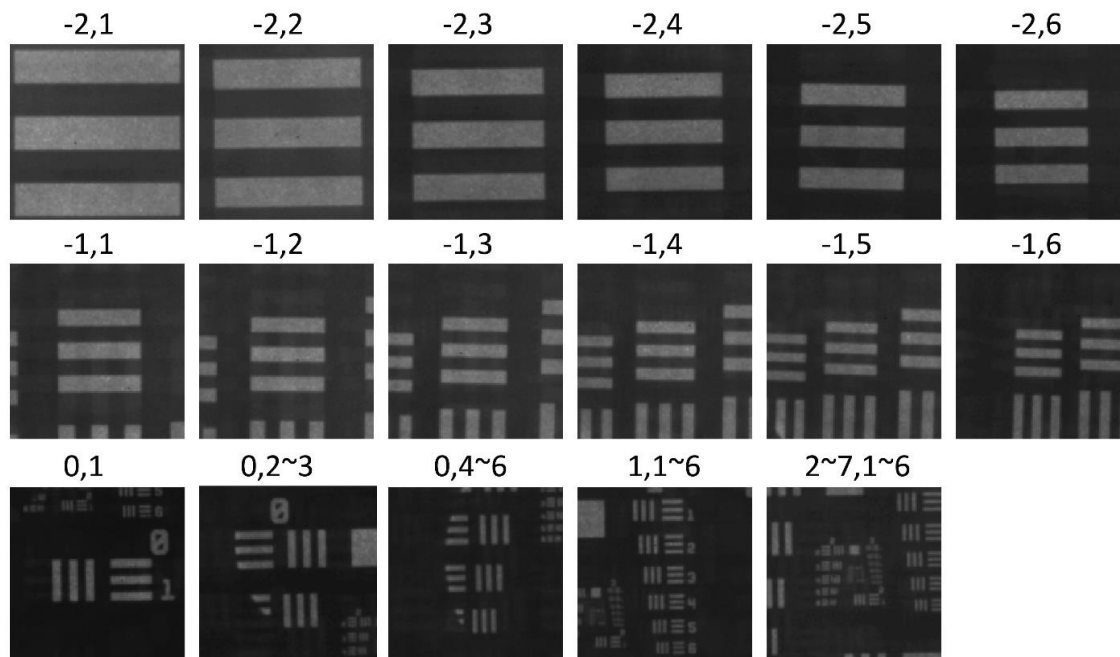
Figure 5.18. Lens design: L1, design wavelength: 450 nm, illumination wavelength: 450 nm and bandwidth: 10 nm.
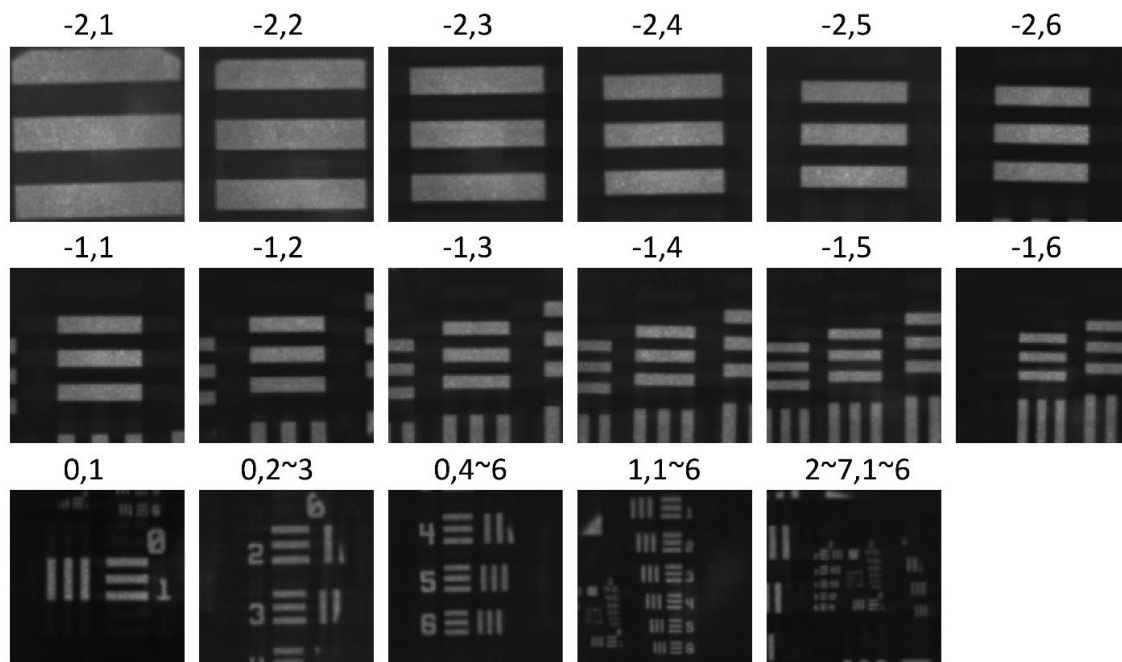
Figure 5.19. Lens design: L2, design wavelength: 538 nm, illumination wavelength: 538 nm and bandwidth: 10 nm.
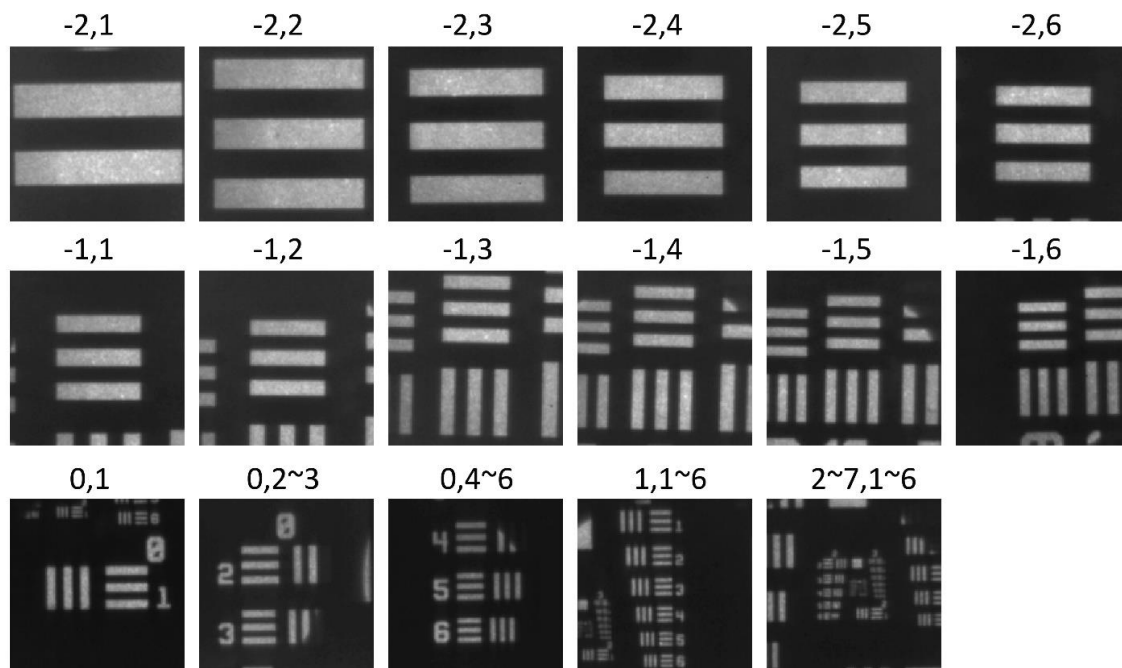
Figure 5.20. Lens design: L3, design wavelength: 610 nm, illumination wavelength: 610 nm and bandwidth: 10 nm.
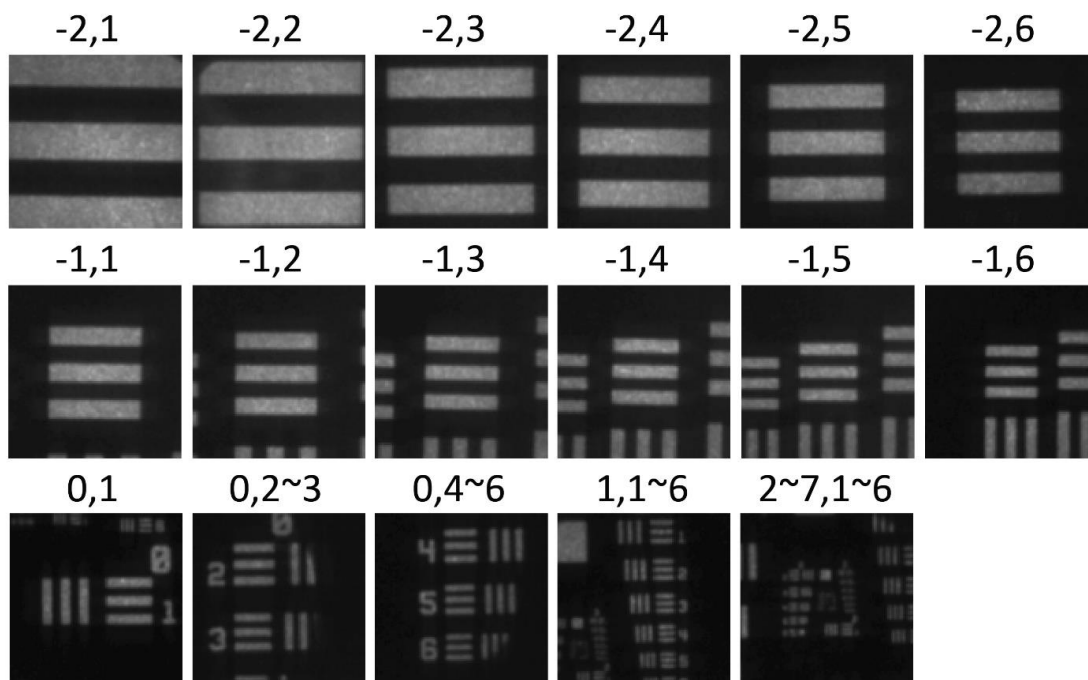
Figure 5.21. Lens design: L4, design wavelength: 780 nm, illumination wavelength: 780 nm and bandwidth: 10 nm.
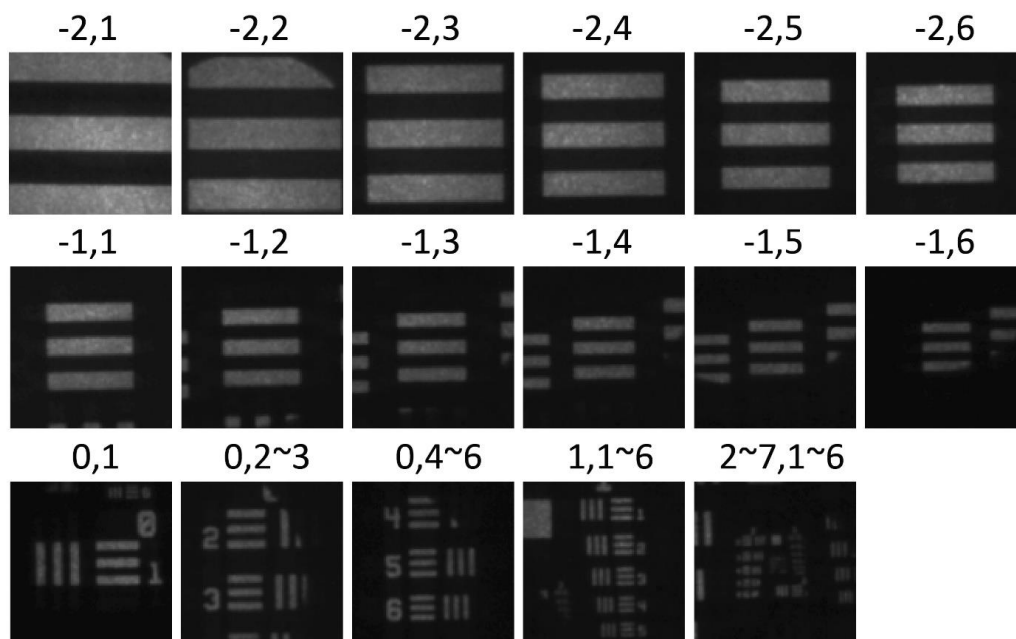
Figure 5.22. Lens design: L5, design wavelength: 850 nm, illumination wavelength: 845 nm and bandwidth: 10 nm.
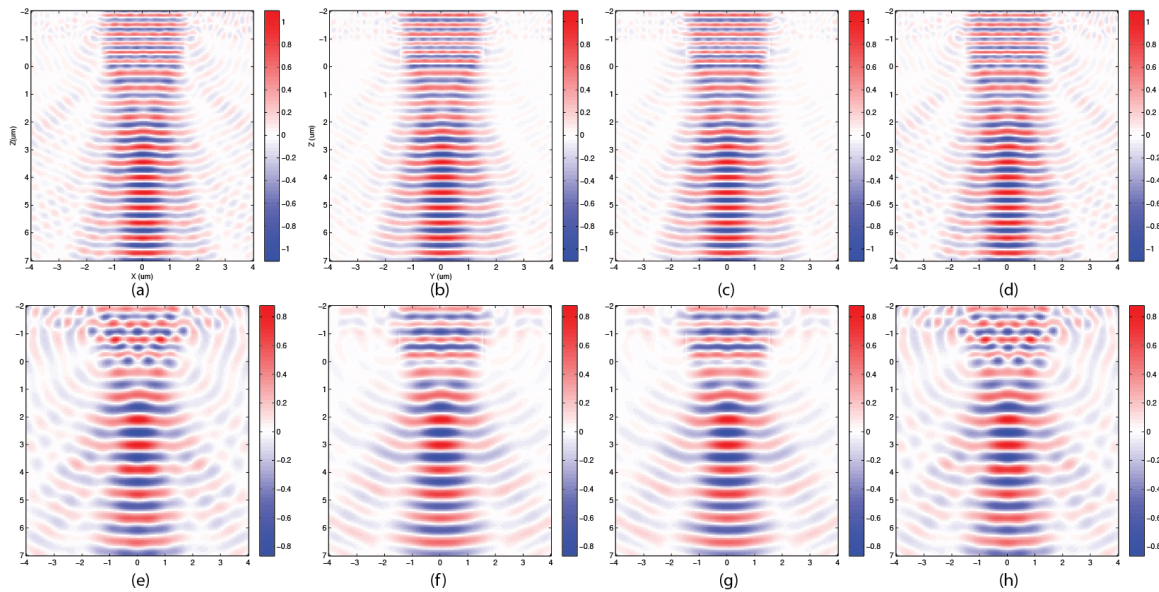
Figure 5.23. 3D FDTD simulation results of single pixel under two orthogonal polarization states. (a) – (d) Illumination wavelength 538nm. (e) – (h) Illumination wavelength 850nm. (a), (b), (e) and (f) Incidence light polarized along X direction. (c), (d), (g) and (h) Incident light polarized along Y direction. (a), (c), (e) and (g) Real part of electric field at XZ cross-section. (b), (d), (f) and (h) Real part of electric field at YZ cross-section.

Table 5.1 Design and geometric parameters of five lenses.

| Pixel size	3 µm				
Number of pixels	198 × 198				
Physical size	0.594 mm × 0.594 mm				
Maximum height	1.4 µm				
Number of grayscale levels	57				
Unit height	25 nm				
Focal length	2.9 mm			2.2 mm		
NA	0.102			0.134		
Design wavelength	450 nm	538 nm	610 nm	780 nm	850 nm

Table 5.2 Optical efficiency

	Lens 1 (450nm)	Lens 2 (538nm)	Lens 3 (610nm)	Lens 4 (780nm)	Lens 5 (850nm)
Bandwidth 10nm	57.60%	70.69%	62.81%	64.80%	57.82%
	94.92%	**98.21%**	**97.62%**	**97.27%**	**96.42%**
Bandwidth 50nm	42.88%	56.58%	47.15%	55.42%	27.31%
	77.51%	**80.41%**	**77.42%**	**86.35%**	**49.27%**
Bandwidth 100nm	27.13%	37.31%	24.23%	33.03%	9.30%
	47.83%	**54.94%**	**44.19%**	**55.23%**	**18.07%**
Bandwidth 200nm	12.98%	26.31%	10.82%	6.09%	1.44%
	23.07%	**41.30%**	**24.15%**	**13.46%**	**2.81%**

Table 5.3 FWHM

		Lens 1 (450nm)	Lens 2 (538nm)	Lens 3 (610nm)	Lens 4 (780nm)	Lens 5 (850nm)
Bandwidth 10nm	X	3.2325um	3.1993um	3.4438um	3.3406um	3.4184um
	Y	3.4959um	3.1349um	3.1858um	3.1224um	3.3274um
Bandwidth 50nm	X	3.5045um	3.4792um	3.5580um	3.4449um	3.4547um
	Y	3.8853um	3.4797um	3.3352um	3.2541um	3.3624um
Bandwidth 100nm	X	3.5901um	3.5877um	3.5825um	3.5162um	3.4053um
	Y	3.7947um	3.5843um	3.3556um	3.3106um	3.2455um
Bandwidth 200nm	X	3.3545um	3.5134um	3.6558um	3.5758um	2.9638um
	Y	3.6727um	3.4805um	3.3160um	3.3412um	2.6986um

Table 5.4 Focal length, magnification, object and image distance

Lens design	Object distance (mm)	Image distance (mm)	Focal length (mm)	Magnification
L1	104	2.98	2.9	0.0286
L2	104	2.98	2.9	0.0286
L3	104	2.98	2.9	0.0286
L4	93	2.25	2.2	0.0242
L5	93	2.25	2.2	0.0242

5.8 References

[1] B. Kress, and P. Meyrueis, *Digital Diffractive Optics: An Introduction to Planar Diffractive Optics and Related Technology* (Wiley-VCH, 2000)

[2] R. Menon, P. Rogge, and H-Y Tsai, "Design of diffractive lenses that generate optical nulls without phase singularities," J. Opt. Soc. Am A **26**, 297-304 (2009).

[3] X. Wan, B. Shen, and R. Menon, "Diffractive lens design for optimized focusing," J. Opt. Soc. Am A **31**, B27-B33 (2014).

[4] A. Arbabi, E. Arbabi, S. M. Kamali, Y. Horie, S. Han, and A. Faraon, "Miniature optical planar camera based on a wide-angle metasurface doublet corrected for monochromatic aberrations," Nat. Commun. **7**, 13682 (2016).

[5] M. Khorasaninejad, W. T. Chen, R. C. Devlin, J. Oh, A. Y. Zhu, and F. Capasso, "Metalenses at visible wavelengths: Diffraction-limited focusing and subwavelength resolution imaging," Science **352**, 1190-1194 (2016).

[6] A. Arbabi and A. Faraon, "Fundamental limits of ultrathin metasurfaces," Sci. Rep. **7**, 43722 (2017).

[7] F. Aieta, P. Genevet, M. A. Kats, N. Yu, R. Blanchard, Z. Gaburro, and F. Capasso, "Aberration-free ultrathin flat lenses and axicons at telecom wavelengths based on plasmonic metasurfaces," Nano Lett. **12**, 4932 (2012).

[8] P. Genevet, N. Yu, F. Aieta, J. Lin, M. A. Kats, R. Blanchard, M. O. Scully, Z. Gaburro, and F. Capasso, "Ultra-thin plasmonic optical vortex plate based on phase discontinuities," Appl. Phys. Lett. **100**, 013101 (2012).

[9] F. Aieta, M. A. Kats, P. Genevet, and F. Capasso, "Multiwavelength achromatic metasurfaces by dispersive phase compensation," Science **347**, 1342-1345 (2015).

[10] E. Arbabi, A. Arbabi, S. M. Kamali, Y. Horie, and A. Faraon, "Multiwavelength metasurfaces through spatial multiplexing," Sci. Rep. **6**, 32803 (2016).

[11] E. Karimi, S. A. Schulz, I. De Leon, H. Qassim, J. Upham, and R. W. Boyd, "Generating optical orbital angular momentum at visible wavelengths using a plasmonic metasurface," Light Sci. Appl. **3**, e167 (2014).

[12] S. Jahani, and Z. Jacob, "All-dielectric metamaterials," Nat. Nanotechnol. **11**, 23–36 (2016).

[13] N. Yu, and F. Capasso, "Flat optics with designer metasurfaces," Nat. Mater. **13**, 139–50 (2014).

[14] B. Shen, P. Wang, R. C. Polson, and R. Menon, "An ultra-high efficiency Metamaterial Polarizer," Optica **1**, 356-360 (2014).

[15] G. Kim, J. A. Domínguez-Caballero, and R. Menon, "Design and analysis of multi-wavelength diffractive optics," Opt. Express **20**, 2814-2823 (2012).

[16] N. Mohammad, P. Wang, D. J. Friedman, and R. Menon, "Enhancing photovoltaic output power by 3-band spectrum-splitting and concentration using a diffractive micro-optic," Opt. Express **22**, A1519-A1525 (2014).

[17] N. Mohammad, M. Schulz, P. Wang, and R. Menon, "Outdoor measurements of a photovoltaic system using diffractive spectrum-splitting and concentration," AIP Advances **6,** 095311 (2016).

[18] P. Wang, and R. Menon, "Optical microlithography on oblique and multiplane surfaces using diffractive phase masks," J. Micro/Nanolith. MEMS MOEMS. **14**, 023507 (2015).

[19] P. Wang, N. Mohammad, and R. Menon, "Chromatic-aberration-corrected diffractive lenses for ultra-broadband focusing," Sci. Rep. **6,** 21545 (2016).

[20] Y. Peng, Q. Fu, F. Heide, and W. Heidrich, "The diffractive achromat: full spectrum computational imaging with diffractive optics," SIGGRAPH '16 Technical Paper, July 24-28, 2016, Anaheim, CA.

[21] J. W. Goodman, *Introduction to Fourier Optics* (Roberts and Company, 2005).

[22] P. Wang, J. A. Dominguez-Caballero, D. J. Friedman, and R. Menon, "A new class of multi-bandgap high-efficiency photovoltaics enabled by broadband diffractive optics," Prog. Photovolt: Res. Appl. **23**, 1073–1079 (2015).

[23] L. J. Guo, "Recent progress in nanoimprint technology and its applications," J. Phys. D: Appl. Phys **37**, R123-R141 (2004).

[24] McKenna, Curt, Kevin Walsh, Mark Crain, and Joseph Lake. "Maskless Direct Write Grayscale Lithography for MEMS Applications." In 2010 18th Biennial University/Government/Industry Micro/Nano Symposium, pp. 1-4. IEEE, 2010.

[25] Data sheet of Shipley 1813 photoresist:
http://micromaterialstech.com/wp-content/dow_electronic_materials/datasheets/S1800_Photoresist.pdf

[26] Data sheet of Heidelberg μPG 101: http://www.himt.de/index.php/upg-101.html

[27] https://www.thorlabs.us/thorproduct.cfm?partnumber=R3L3S1N

CHAPTER 6

POWER EFFICIENT LIQUID CRYSTAL DISPLAYS

This chapter is adapted from the following manuscript in preparation: Nabil Mohammad, Jose Dominguez-Caballero, Erick Ramos-Murillo, Akihiro Takagi, Kunjal Parikh, and Rajesh Menon, "Power-efficient liquid-crystal displays using broadband diffractive color splitting".

6.1 Abstract

Absorptive color filters significantly reduce the efficiency of color liquid-crystal displays (LCDs) because each color subpixel transmits less than 1/3rd of the incident light. Here, we apply a nonabsorbing diffractive element to separate the incident light into the primary colors, resulting in a significant increase in the overall transmission efficiency of the LCD. The diffractive element, which we call a polychromat, was fabricated using grayscale lithography and we experimentally demonstrated an increase in transmission efficiency of 19% with a standard LCD for a white screen without any decrease in color gamut. Our approach overcomes the fundamental trade-off between light transmission and color gamut, which plagues conventional color filters.

6.2 Introduction

Liquid-crystal displays (LCDs) are widely used in today's cellphones, notebooks, computer monitors and many handheld portable devices. In the vast majority of these devices, a white backlight is used for illumination. Spatially patterned electrodes form pixels by locally controlling the orientation of a thin liquid crystal (LC) layer. Pixel-level light modulation is achieved by placing a pair of polarizers to sandwich the LC layer as illustrated in Figure 6.1(a). A color filter array (CFA) consisting of red, green and blue (RGB) subpixels is placed in precise alignment to the electrodes (Figure 6.1(b)). The CFA is comprised of organic dye molecules that transmit only a certain bandwidth of the incident light, while absorbing the rest. On average, less than 1/3rd of the incident light is actually transmitted, which drastically reduces the overall efficiency of the LCD. Furthermore, the purity of each primary color, which determines the color gamut of the

display, is inversely proportional to the width of the transmitted band. As a result, there is a fundamental trade-off between color gamut and transmission efficiency of the display [1,2].

Several approaches have been proposed in the past to replace the CFA. Rather than absorbing the complementary colors, engineered interference of light using a dispersive microlens pattern can create color separation [3]. Dispersive holographic gratings were used for high-brightness LCD projectors [4]. However, such approaches tend to be very inefficient, since these optics were only designed for a few discrete wavelengths. Diffraction grating and microlens combinations have been reported in [5] for color-filter-less LCD. This system uses a rear illuminator consisting of a total-internal reflecting (TIR) lightguide and a grating along with microlenses to produce spatially separated RGB colors. This system has poor viewing-angle characteristics and poor color gamut. A set of dual-grating and dual-lenticular lens array was proposed in [6] to substitute the color filter. In this approach, color splitting can be achieved via a dual grating. However, a dual-lenticular-lens array is required to scale the beam size. Furthermore, the proposed system was not demonstrated experimentally. In all these prior cases, the overall efficiency is limited by the diffraction efficiency of the grating. Finally, the use of multiple elements renders such displays much thicker than is practical for commercial applications.

6.3 Design Principle

We have previously designed, fabricated and characterized diffractive optics that can operate over a large bandwidth with high efficiency [7-9]. Here, we utilize these optics to spectrally split the backlight illumination into red, green and blue color subpixels, and

thereby enhance the overall transmission efficiency of LCDs. The schematic of our modified display is shown in Figure 6.1(c). Our optic, which we call a polychromat is comprised of a 2D array of square "pixels", the heights of which are determined by an optimization-based design algorithm [10]. Note that the polychromat is periodic and the period is determined by the periodicity of the LCD pixels, 133.5µm in our experiments. The final design of the polychromat is illustrated in Figure 6.1(d), where we assumed that the polychromat pixels are of width, W = 9µm, the heights were allowed to vary between 0 and 2µm, and the distance between the polychromat and the image plane, d = 1mm. Only one period of the polychromat comprised of 14 X 14 pixels is shown. A small unpatterned buffer layer is added to ensure that the periodicity of 133.5µm matches that of the LCD pixels. The simulated transmission efficiency spectrum of the polychromat is shown in Figure 6.1(e). A backlight with an angular full-width at half-maximum (FWHM) of 4° was assumed. The measured spectrum of the backlight and the transmittance spectrum of the CFA were incorporated into our model. From the transmission efficiency spectrum, we can calculate the expected increase in luminance for the 3 primary colors as: 28% (red), 12% (green) and 12% (blue), which corresponds to an average increase in luminance of 17%. Note that such a transmission spectrum is quite different than what one would expect from a diffraction grating or a simple diffractive lens. The color gamut was preserved the same as that of the original display.

In order to indicate the potential of our approach, we also performed a polychromat design that is able to obtain an increase in luminance of 1.58X for each primary color with the same illumination as in Figure 6.1(e). Higher luminance can be obtained by using smaller (pixel width = 2.8µm) and taller pixels (maximum height = 4.5µm) in the

polychromat design as well as by reducing the distance between the polychromat and the image-reconstruction plane (d=0.6mm). The simulated transmission spectrum of the designed polychromat along with the pixel geometries is summarized in Figure 6.1(f). Note that a 1D polychromat was designed in this case for computational simplicity. In general, relative increase in luminance of 1.5X or more can be attained using this approach by using more complex polychromat geometries.

6.4 Experiment and Results

For experimental simplicity, we chose to fabricate the design shown in Figure 6.1(d). This polychromat was fabricated using grayscale optical lithography as a multi-level pattern in photoresist atop a glass substrate. Details of the fabrication process are included in the Supplementary Information. A photograph of the final device is shown in Figure 6.2(a). The optical micrograph in Figure 6.2(b) shows that the geometry is consistent with the design in Figure 6.1(d). The pixel heights from various rows of the device were measured using a stylus profilometer and we confirmed that the average error of the fabricated heights from the designed heights is less than 80 nm (See Supplementary Information for details). A laser scanning confocal microscope (Keyence VK-X250) was used to confirm the multilevel structure of the polychromat (Figure 6.2(c)).

As part of the optical characterization, the polychromat was illuminated with a custom backlight (FWHM=4°) and the reconstructed image plane was magnified using an objective lens (20X) onto a diffuser as shown in Figure 6.3(a). The magnified image was photographed as shown. The incident white light is clearly separated into the 3 color components as expected.

A chrome-on-glass mask was fabricated to mimic the aperture of each color sub-pixel in the LCD as illustrated in Figure 6.3(b). Details of the experimental setup and measurement process are provided in Supplementary Information. The mask was placed in the image plane of the polychromat, which was illuminated by the same backlight as before, but the angular divergence was adjusted to $2°$. Then, the transmitted spectrum was measured using a fiber-input spectrometer equipped with a cosine corrector. The aperture of the mask was aligned to each color subpixel using a micrometer stage. The measured transmitted spectra for the red, green and blue colors are plotted in Figure 6.3(c). A baseline spectrum was also taken without the polychromat. From the spectra, we can compute the relative increase in luminance averaged over all 3 colors as a result of the polychromat as 1.25X. As expected, the increase in luminance is dependent upon the angular divergence of the backlight. In the inset of Figure 6.3(c), we plot the measured increase in luminance as a function of the angular divergence of the backlight illumination.

Finally, we measured the transmitted spectrum after adding the LCD. The LCD was a commercially available display (Chimei Innolux N116HSE-EJ1), whose backlight was carefully removed (see Supplementary Information). In this case, the LCD was made entirely uniform of a given color (red, green, blue or white). The polychromat was aligned using a micrometer stage to have its reconstruction plane match the corresponding color subpixels in the LCD. The transmitted spectra were measured in the same manner as before and compared to the baseline case. The results are plotted in Figure 6.4. Note that the CFA was not removed from the LCD as indicated in Figure 6.1(c). The polychromat resulted in a significant increase in luminance for the red, green and white screens. A small reduction in luminance was noticed for blue, which was attributed to fabrication and measurement

alignment errors.

A diffuser has to be placed closer to the viewer in order to increase the viewing angle. As described in the Supplement Information, we performed preliminary experiments to confirm that the diffuser does not adversely impact the sharpness of the display even at large viewing angles. We also computed the color gamut of the display based upon the measured transmission spectra (see Supplementary Information and Figure 6.14) and showed that the gamut of the display is preserved.

6.5 Discussions

In this paper, we have reported a new power-efficient LCD that utilizes a broadband diffractive element to split white light into the primary colors and thereby, increase the overall transmission efficiency. Our simulations indicate that the luminance of conventional LCDs can be increased by over 50% using this technique. We experimentally demonstrated an average increase in luminance of the white screen of ~19% using a polychromat with 9µm-wide pixels and a conventional LCD. The polychromats can be manufactured at low cost using standard imprinting techniques. By combining the polychromat with compact collimated backlights, we expect to drastically increase the power efficiency of LCDs. This is of particular importance in mobile devices, where outdoor usage and battery life are key metrics that could be significantly improved using this technology.

6.6 Supplementary Information

6.6.1 Device Fabrication

Grayscale optical lithography was used to fabricate the polychromat [11]. Grayscale exposure was done using μPG 101 pattern generator tool from Heidelberg Instruments [12]. The fabrication process flow is shown in Figures 6.5(a) and (b). A 3"×3"×0.06" soda lime clear glass substrate was RCA cleaned. A commercially available photoresist, Microposit S1813 [13], was spin coated on the glass substrate at 1000 rpm for 60 seconds using CEE 200X spinner. This led to a ~2.6μm thick uniform film of S1813. The sample was baked in an oven (Binder FD53-UL) at 110° C for 30 minutes. The sample was kept in a fume hood overnight for rehydration. Two samples were prepared using the same process: one for calibrating the grayscale exposure and the other for fabricating the polychromat design. The calibration design (Figure 6.5(c)) is a bmp file which consists of 50 rectangles (27μm × 500μm) with grayscale values varying from 1 to 99 in a step of 2. The gap between the rectangles is 42μm and the grayscale of this region is 0. The sample was exposed with this calibration design using the pattern generator tool. As the write head scans the sample surface, the exposure dose is modulated according to the grayscale values of the calibration design (Figure 6.5(a)). After exposure the sample was developed in AZ 1:1 developer for 1 minute 30 seconds. The sample was rinsed with DI water and dried with N2 blow. An optical micrograph of the calibration sample is shown in Figure 6.5(d). A stylus profilometer (Tencor P-10) was used to measure the depth of the exposed regions. The measurement is shown in Figure 6.5(e). As expected, the depth of the exposed region increases with grayscale values. This calibration was used to convert the 2D height distribution of the polychromat design into a 2D grayscale map shown in Figure 6.6(a).

The other sample was exposed with this 2D design. The design was repeated 74 times in X and 52 times in Y direction with a gap of 7.5µm between the designs in both directions. This resulted in a polychromat with an area of 9879µm x 6942µm after development. The fabricated microstructures were characterized by scanning the tip of the stylus profilometer (Tencor P-10) on the surface of the device. Measurements were done at three different locations (row 3, 4 and 10 of different periods) which were randomly chosen. Mean difference between design and measured heights were 70nm, 69nm and 102nm, respectively. Measurements are shown in Figures 6.6(b)-(d). Excellent agreement between the design and measurement can be noted.

6.6.2 Backlight Source

An LED flashlight was used as the illumination source (backlight) for our experiments. The flashlight was connected to a regulated DC power supply (Longwei Electric PS-305D) and run in constant current mode (1A). The flashlight was placed at three different distances from the polychromat to get three angular divergences, FWHM=2°, 3° and 4°. FWHM is defined as: $\Theta=2\arctan((D_f-D_i)/2l)$, D_f, D_i are beam diameters at two separate points and l is the distance between these two points. The spectrum of the flashlight for FWHM=4° is shown in Figure 6.7.

6.6.3 Inspection of Reconstruction Plane of Polychromat

The polychromat was mounted onto a cage rotation mount (Thorlabs LCRM2/M) which in turn was mounted onto a manual linear stage (Newport 423 series). This setup was then mounted onto a two-axis linear translation stage with rotating platform (Thorlabs

XYR1) via an angle bracket (Newport 360-90). This setup allows us to move the polychromat in X, Y and Z directions and also rotate it in XY and XZ planes as shown in Figure 6.8(a). To magnify the reconstruction plane of the polychromat, an objective lens (Olympus UMPlanFl 20x/0.46) was placed in front of the polychromat. Both the polychromat and the objective was aligned in a way such that they were in a plane perpendicular to the beam propagating from a red laser diode (Thorlabs CPS180). The polychromat was illuminated by the LED flashlight (FWHM= 4°). The polychromat was moved in the Z direction using the micrometer stage until the objective focused the reconstruction plane onto a diffuser. Figure 6.8(b) shows the experimental setup.

6.6.4 Characterization of Polychromat with Chrome-on-Glass Mask

Figure 6.9(a) shows the schematic of the setup for measuring luminance boost using a chrome-on-glass mask. Actual setup is shown in Fig. 6.9(b) and a close view is provided in Figure 6.9(c). A 3" x 3" microfabricated chrome mask (fabricated by Front Range Photomask LLC) was mounted onto a filter holder. A beam from a red laser diode (Thorlabs CPS180) was shined onto the chrome mask and the corresponding retro reflection from the surface of the mask was used to align it in a plane perpendicular to the beam propagation. The polychromat was brought close to the chrome mask and also aligned perpendicular to the laser beam. The gap between the mask and polychromat was adjusted to 1mm. The polychromat was illuminated by the LED flashlight (FWHM=2°). A red filter (K&F Concept 52mm) was placed in between the polychromat and flashlight [Figure 6.9(c)]. At this point the surface of the chrome mask is parallel to the surface of the polychromat but the RGB bands created by the polychromat are not in alignment with

the mask apertures. A diffuser was placed just in front of the mask. A moiré pattern appeared as shown in Figure 6.9(d). The polychromat was rotated in the XY plane until the moiré fringes disappeared (Figure 6.9(e)). The diffuser was removed and a fiber patch cord (Ocean P400-1-UV-VIS), equipped with a cosine corrector (Thorlabs CCSA1), was placed just in front of the mask touching its surface. The other end of the cord was connected to a spectrometer (Ocean Optics Jaz series). The polychromat was moved in X and Y direction until the intensity counts of the transmitted spectrum reached a maximum value. At this point, only red sub-bands were produced by the polychromat (because of the red filter) and they were aligned to mask apertures in both X and Y directions. A slight adjustment in the Z direction was also made to ensure that the reconstruction plane of the polychromat coincides with the mask rear surface. The red filter was removed and the polychromat was illuminated by white light emanating from the flashlight (FWHM=2°). As a result, all three sub-bands (RGB) were produced by the polychromat at this time and the red sub-bands were still in alignment with the mask apertures. Transmitted spectrum was measured using the spectrometer. The polychromat was then moved by ~44.5µm in the X direction to align the green sub-bands and then another ~44.5µm to align the blue sub-bands with mask apertures and the corresponding transmittance were measured. For baseline measurements, the polychromat was moved in the XY direction so that the cosine corrector received light through the unpatterned region of the photoresist on the polychromat substrate with the mask still in front of it. From each measurement, tristimulus values and corresponding luminance were calculated using MATLAB. Luminance boost was then calculated as follows:

$$Boost=(L_R+L_G+L_B)/(3{\times}L_{Baseline}) \quad (6.1)$$

Here, L_R, L_G, L_B and $L_{Baseline}$ are the luminance values for cases when red, green, blue sub-bands and unpatterned region were aligned to the chrome mask apertures, respectively. The process was repeated for backlight angular divergences of 3° and 4°. Spectrometer measurements are shown in Figure 6.10.

6.6.5 Characterization of Polychromat with a Standard Display

In this case, the chrome-on-glass mask was replaced by a CMI display (CHIMEI INNOLUX N116HSE-EJ1). The backlight and diffusers were removed from the display (Figure 6.11(a)) and the remaining part (LC stack) was connected to a laptop (Sony Vio Pro 13) via a flex cable (Figure 6.11(b)). Figure 6.12(a) shows the schematic of the setup for measuring luminance boost using the modified display. Photographs of the actual setup are shown in Figures 6.12(b) and (c). The display and the polychromat were aligned perpendicular to the red laser beam. The gap between the two was adjusted to ~667µm. The polychromat was designed for a gap of 1mm assuming that the medium between the polychromat surface and the reconstruction plane is air. However, the medium between the polychromat and color filter array (CFA) in the display is not completely air because of the stack of glass and polarizer behind the CFA. Thickness of this stack is ~500µm. Considering an effective index of refraction of 1.5 this translates into ~333µm. This gives the effective gap of ~667µm. The polychromat was illuminated by the white light (FWHM=2°). A red screen was displayed on the modified display with the aid of an external monitor connected to the laptop. This essentially allowed the red subpixels of the

display, i.e., subpixels aligned with the red filter of CFA, to turn on. Misalignment between the CFA subpixels and red sub-bands of polychromat reconstruction plane produced moiré fringes (Figure 6.12(d)) and the polychromat was rotated in the XY plane until the disappearance of the fringes (Figure 6.12(e)). The cosine corrector, mounted on the spectrometer fiber tip, was then placed in front of the display. The polychromat was moved in X and Y directions using the micrometer stages until a maximum value in the transmitted spectrum was noted. A slight adjustment in Z direction was also made. Once done with the alignment, red, green, blue and white screens were displayed on the screen one after another and corresponding spectrometer measurements were done. To take the baseline measurements, the polychromat was moved in XY plane such that the light through the unpatterned photoresist of the substrate (with the display still in front of it) reached the cosine corrector. Similar to the polychromat case, spectrometer measurements were done for red, green, blue and white screens. Tristimulus values and corresponding luminance values were calculated for each measurement and luminance boost was obtained for each color as follows:

$$Boost_i = L_{poly\_i}/L_{unpat\_i} \quad (6.2)$$

Here, i stands for different colors, *i.e.*, red, green, blue and white. L_{poly_i} and L_{unpat_i} are the luminance values while the measurements were done for the patterned and unpatterned regions of the sample, respectively. These measurements were repeated for backlight FWHM 3° and 4°. The results are shown in Figure 6.13.

6.6.6 Impact of Diffuser

A diffuser needs to be placed in front of the display to preserve the viewing angle. However, it is important that the sharpness of the display is not affected because of the diffuser. Figure 6.15 shows photographs of the display with polychromat and diffuser in place. A text 'UTAH' was displayed along with colored backgrounds. The text was positioned on the display in such a way that it appeared in front of the polychromat. For each color, photographs were taken at different viewing angles (0°, ~30° and ~60° with respect to display normal).

6.7 Author Contributions

J.A.D-C., A.T., K.P., and R.M. conceived and designed the experiments. N.B, J.A.D-C and R.M. modeled, optimized and characterized the devices. N.M. fabricated the devices. N.M, E.R.M, J.A.D-C and A.T. performed the experiments and numerical analysis. N.M, J.A.D-C. and R.M. analyzed the data and wrote the paper.
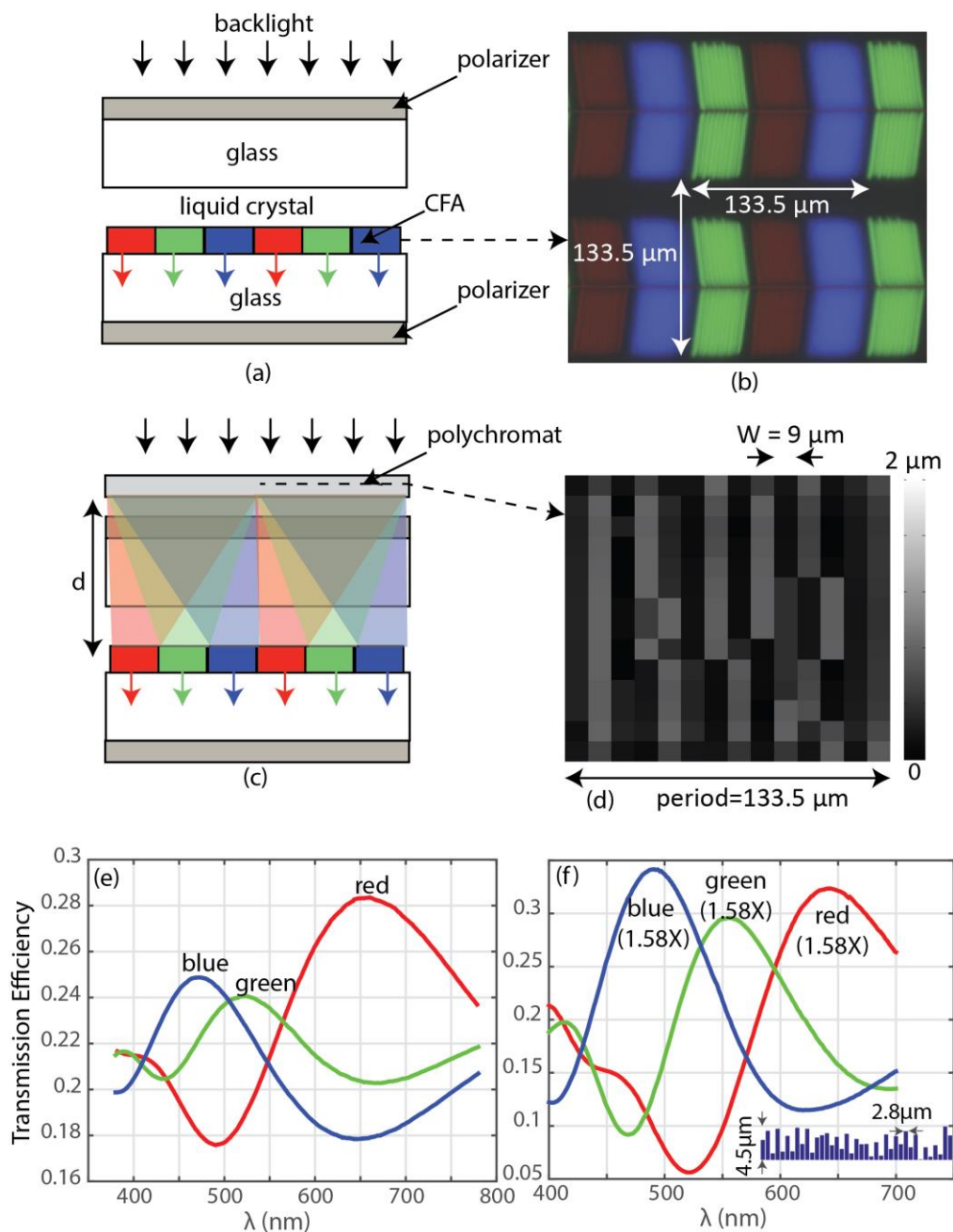
Figure 6.1. Details of the polychromat based LCD. (a) Conventional liquid-crystal cell. (b) Optical micrograph of the color-filter array from a CMI display (CHIMEI INNOLUX N116HSE-EJ1). (c) Liquid-crystal cell using a polychromat to enhance transmission efficiency. The polychromat separates the red, green and blue colors, and concentrates them onto the appropriate CFA color sub-pixels. (d) Polychromat design used in our experiments. (e) Simulated transmission-efficiency spectrum of the polychromat. (f) Simulated transmission-efficiency spectrum of a 1D polychromat showing an increase in luminance of 1.58X. Better performance is achieved in this case due to the smaller pixel widths (2.8μm), larger maximum pixel heights (4.5μm) and shorter image distance (0.6mm). The design heights of 48 pixels are shown in the bottom-right inset.
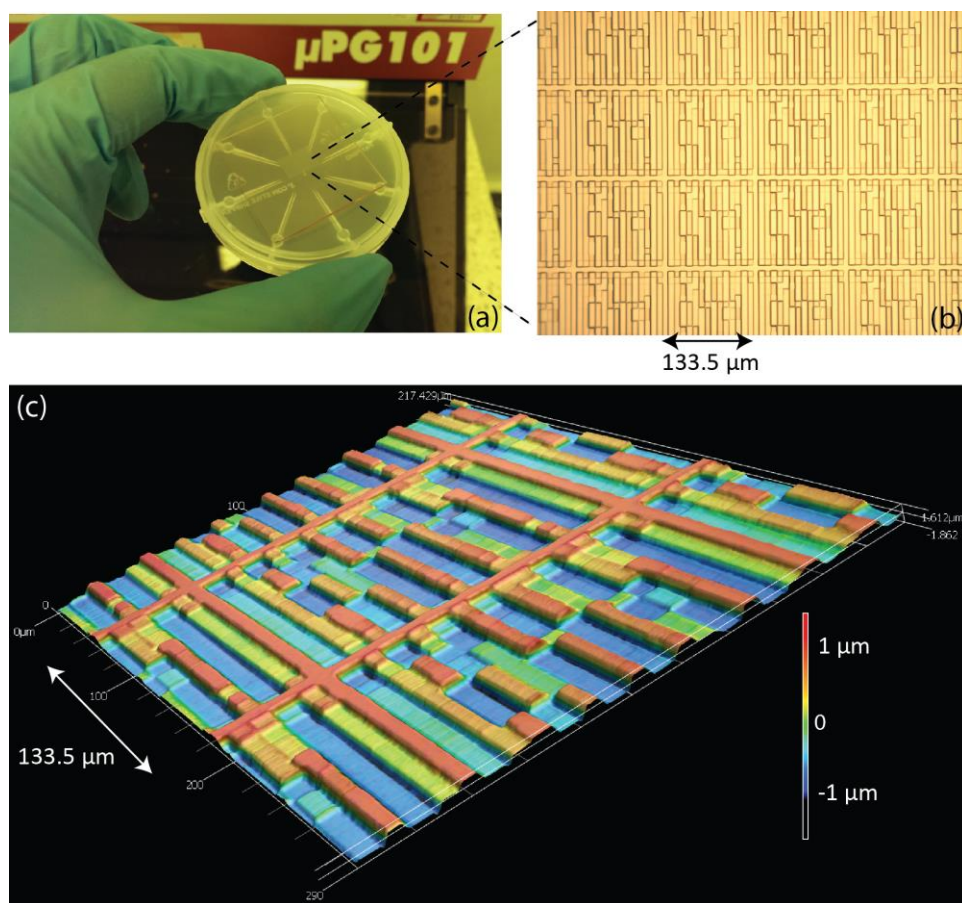
Figure 6.2. Fabricated polychromat. (a) Photograph of device fabricated in photoresist on a glass substrate. (b) Optical micrograph of a portion of the polychromat. (c) Image of the polychromat using a laser-scanning-confocal microscope.
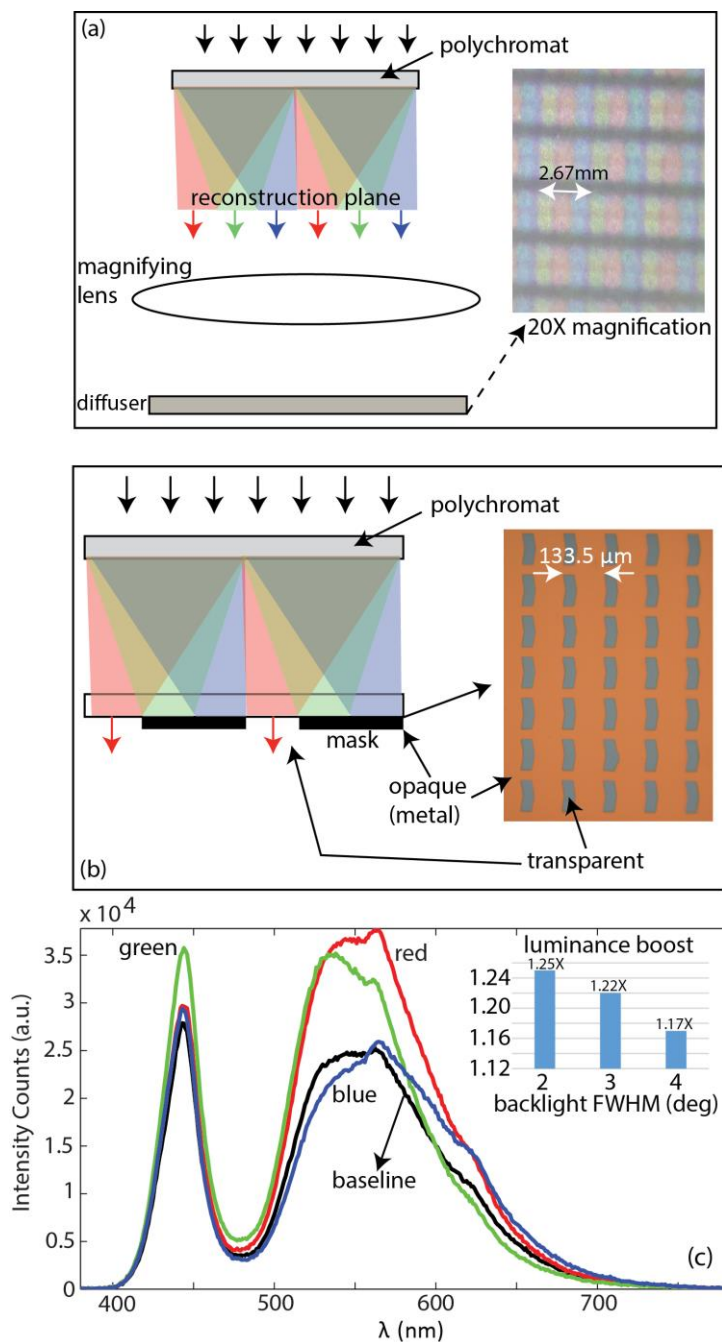
Figure 6.3. Characterization of the polychromat without the LCD. (a) The reconstruction plane was magnified onto a diffuser. A photograph of the magnified image showing the color splitting is shown on the right. (b) A microfabricated mask was used to measure the increase in luminance due to the polychromat. An optical micrograph of the mask is shown on the right. (c) Measured spectrum through the mask. Baseline spectrum is without the polychromat. A cosine corrector was attached to the fiber input of the spectrometer. The polychromat increases luminance by 1.25X for a backlight FWHM=2°. The inset shows the measured luminance boost as a function of the angular divergence of the backlight.
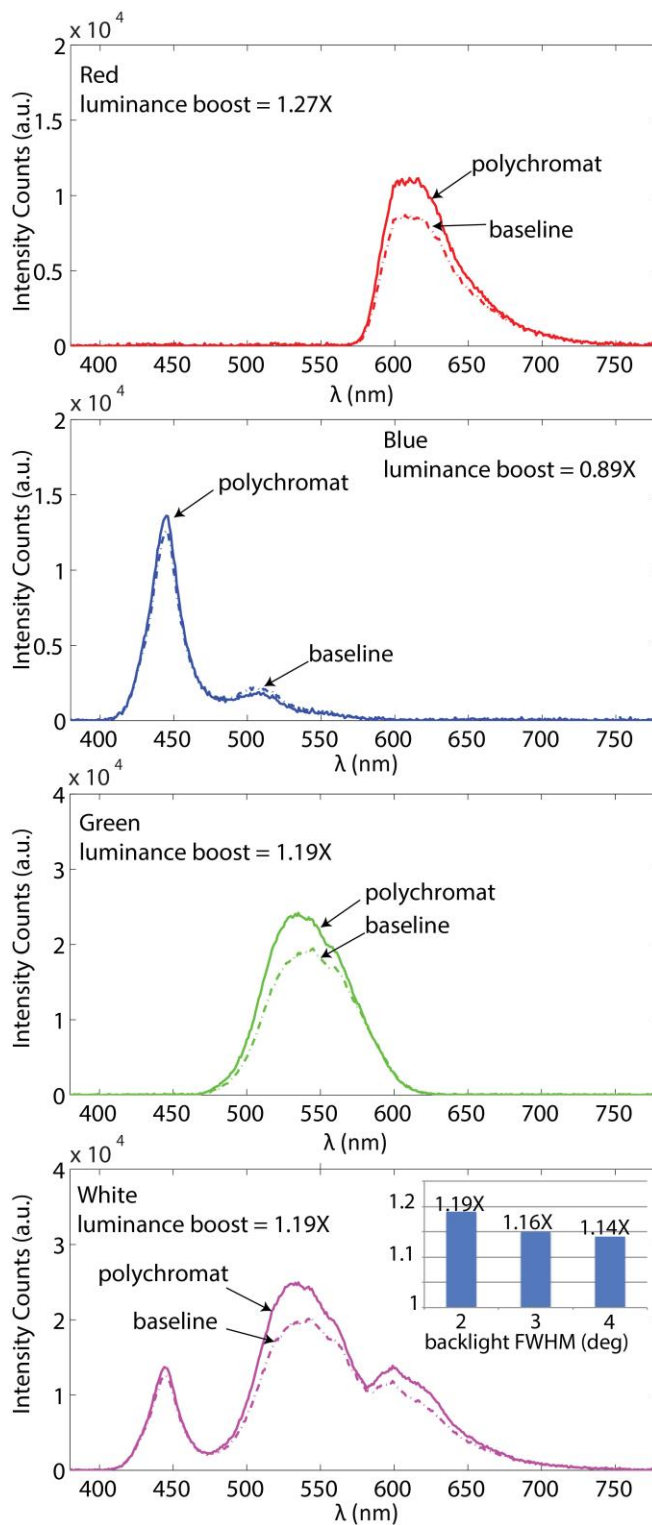
Figure 6.4. Measurements of polychromat with LCD. Transmitted spectra with the polychromat (solid lines) and without the polychromat (baseline, dashed lines) for (a) red, (b) green, (c) blue and (d) white screens. (d) Inset: The increase in luminance as a function of the angular divergence of the backlight for the white screen.
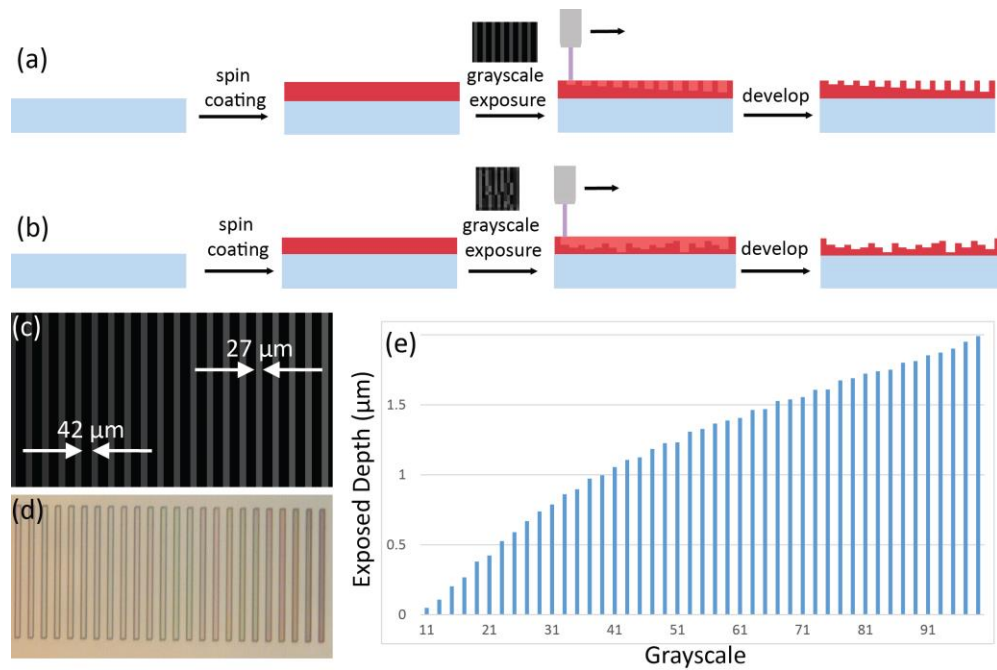
Figure 6.5. Fabrication of polychromat. (a)-(b) Process flow for calibration and actual polychromat fabrication, respectively. (c) Calibration design. (d) Optical micrograph of calibration sample. (e) Stylus profilometer measurement of calibration sample.
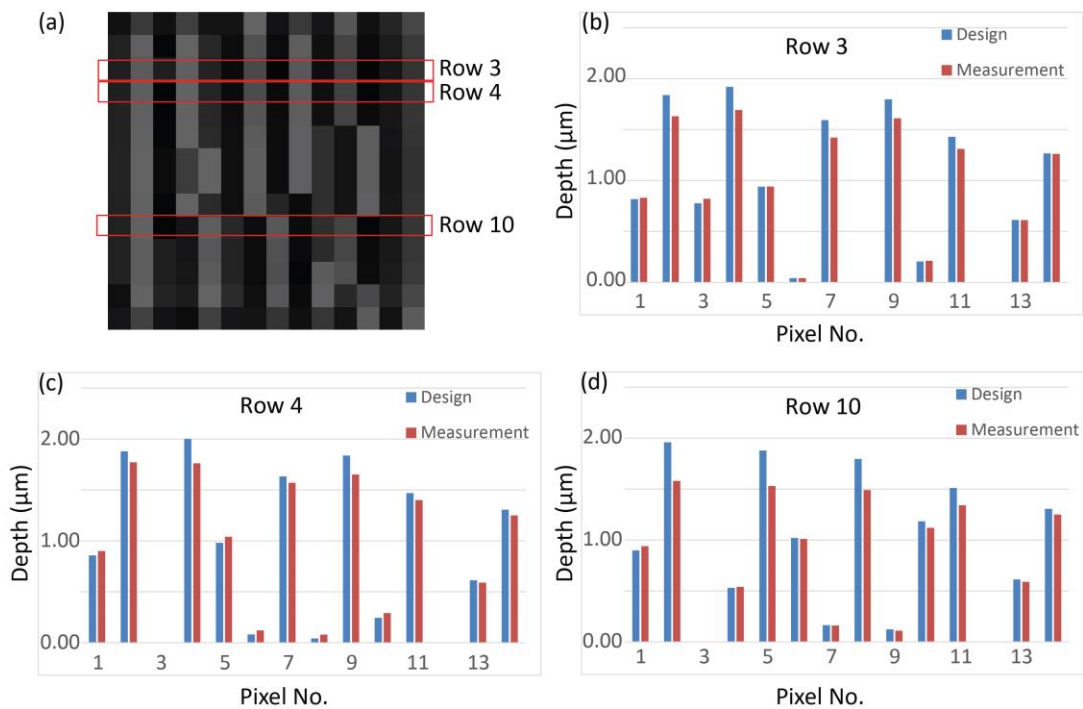
Figure 6.6. Comparison between design and measured heights. (a) Grayscale design of polychromat (one period). (b)-(d) Stylus profilometer measurements of row 3, 4 and 10, respectively. Although shown on the same period in (a) for simplicity, the rows belong to different periods of the polychromat.
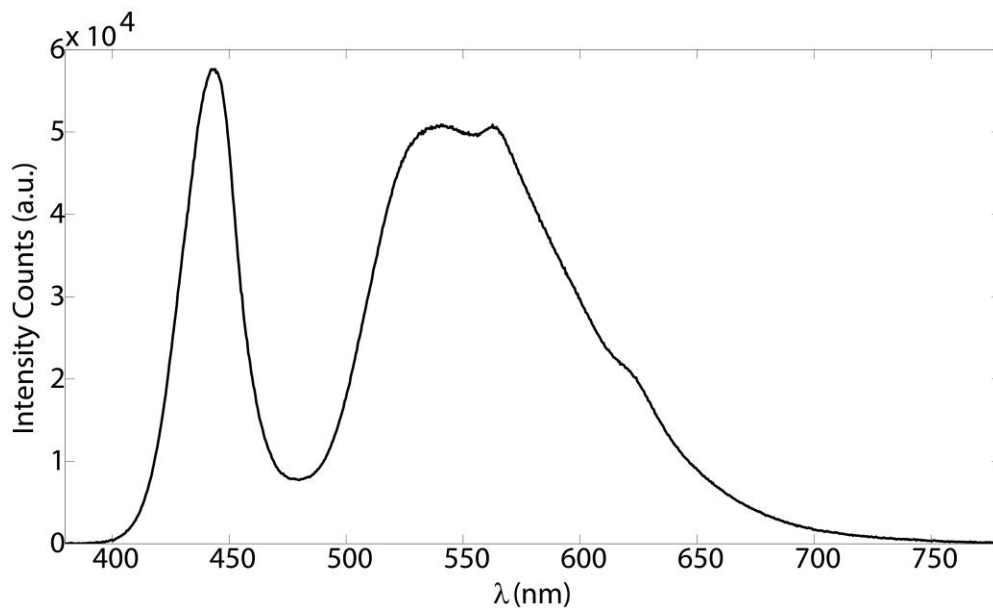

Figure 6.7. Spectrum of LED flashlight (FWHM=4°).
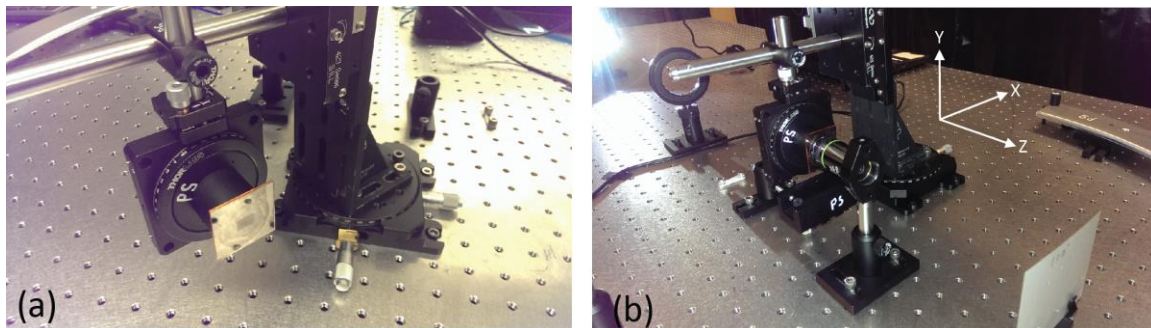
Figure 6.8. Experimental setup. (a) Polychromat mounted on to a three axis micrometer stage (with rotating platforms). (b) Magnification of polychromat reconstruction plane using a 20X objective lens.
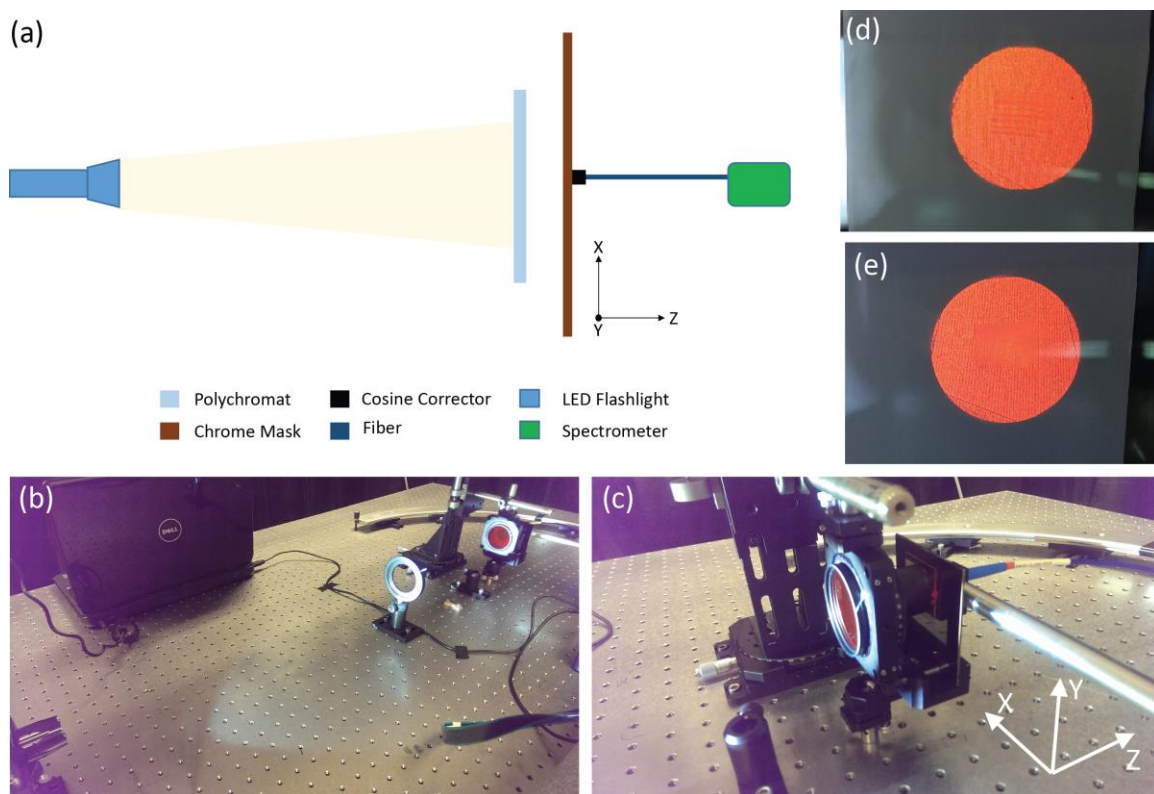
Figure 6.9. Experimental setup for measuring luminance boost using the chrome mask. (a) Simplified schematic (top view) of the setup for characterizing the polychromat using a chrome-on-glass mask. (b)-(c) Photographs of the actual setup. The red filter was used for polychromat alignment. Spectrometer measurements were done without the filter. (d) Appearance of moiré pattern before polychromat alignment. (e) The pattern disappeared once the rotation of the polychromat was adjusted in the XY plane.
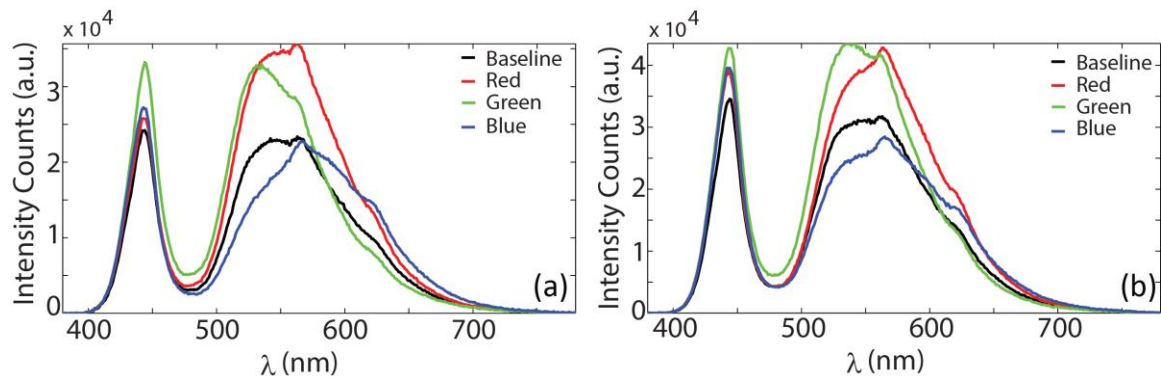
Figure 6.10. Measured spectrum through the mask. (a)-(b) The polychromat increases luminance by 1.22X and 1.17X for backlight FWHM of 3° and 4°, respectively.
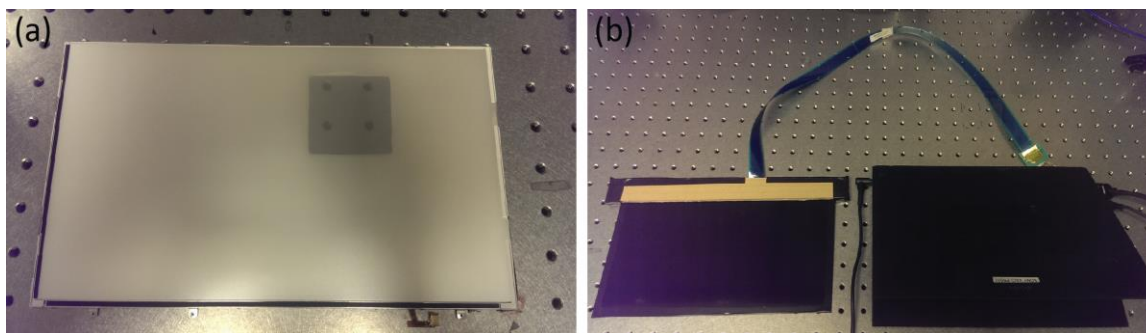
Figure 6.11. CMI display used in the experiment. (a) Removed backlight and diffuser. (b) LC stack connected to a Sony Vio Pro 13 laptop via a flex cable.
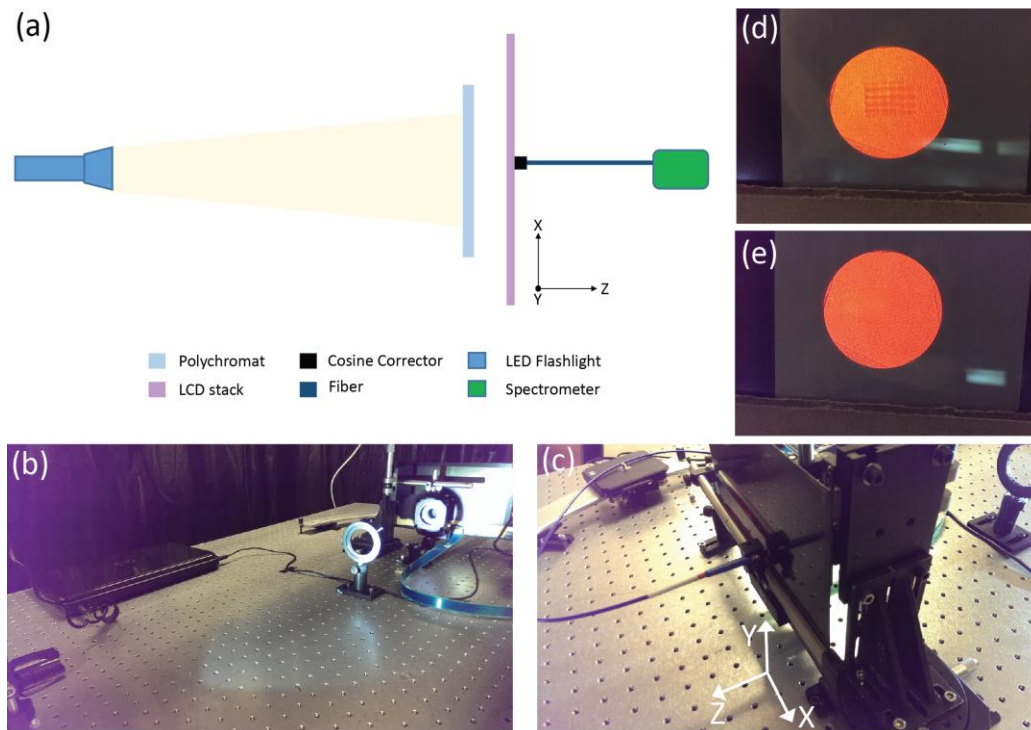
Figure 6.12. Experimental setup for measuring luminance boost using the lcd. (a) Simplified schematic of the setup (top view). (b)-(c) Photographs of the actual setup: rear view and front view, respectively. (d) Moiré pattern appeared due to tilt of the reconstructed RGB color sub-bands in the XY plane with respect to the RGB sub-pixels of the display. (e) As the polychromat was rotated in the XY plane, moiré fringes disappeared.
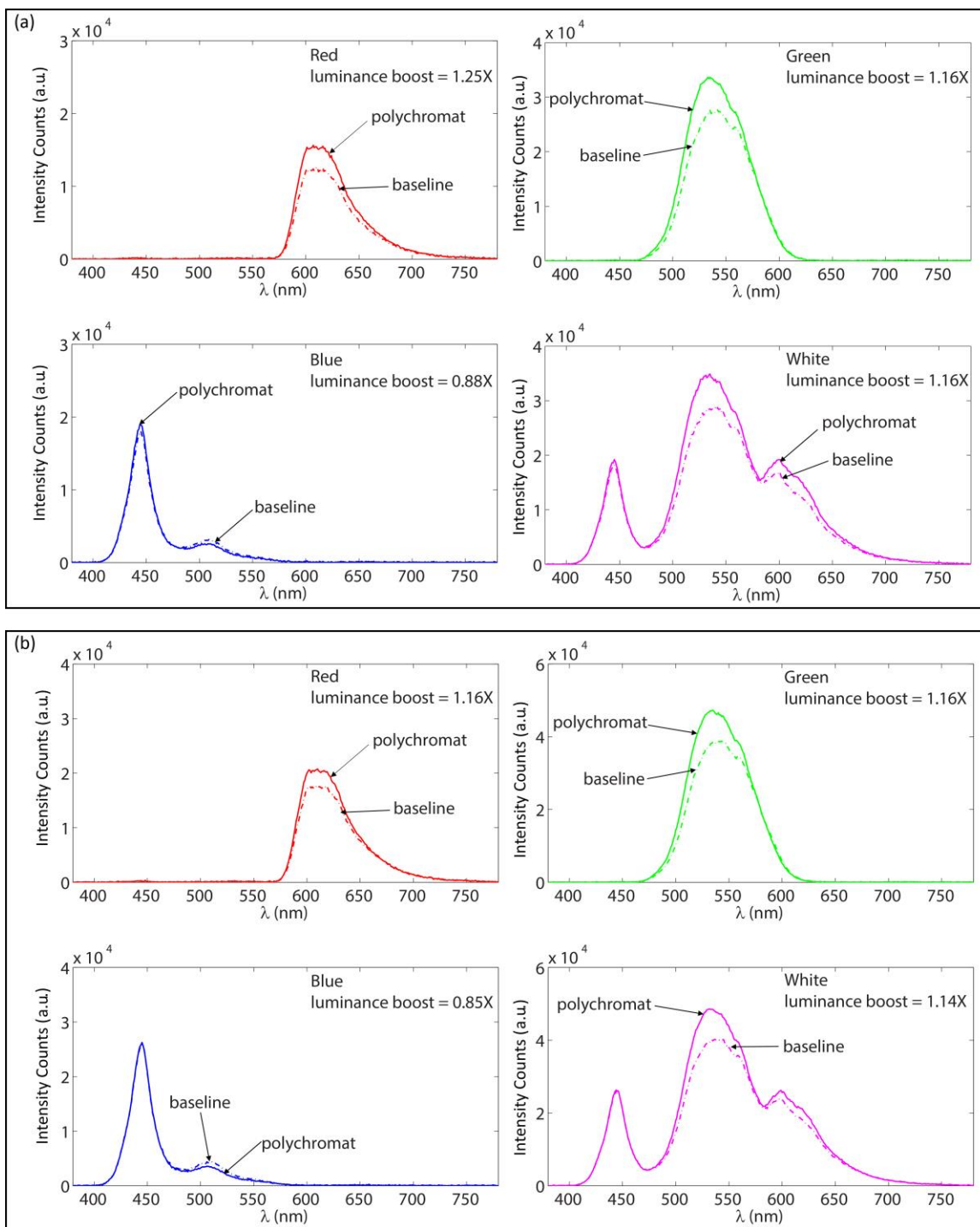
Figure 6.13. Experimental results. (a)-(b) Spectrometer measurements of transmitted spectrum through polychromat (solid lines) and without polychromat (dashed lines) for backlight FWHM=3° and 4°, respectively. The luminance was increased by 1.16X and 1.14X at the presence of the polychromat.
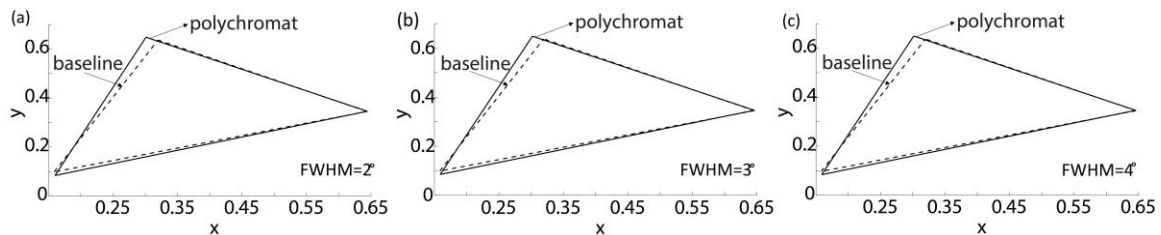
Figure 6.14. Color gamut with the polychromat compared to the reference case using the measured spectra under 3 different backlight illumination.
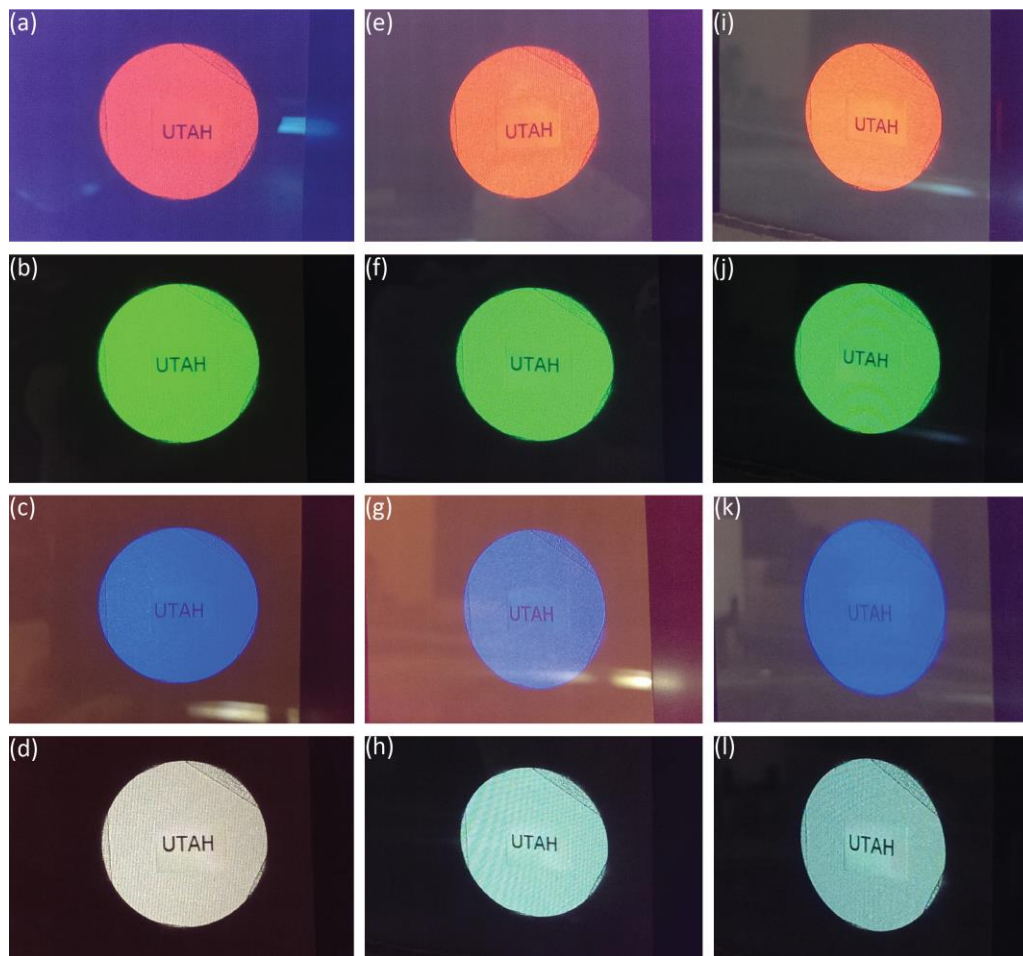
Figure 6.15. Testing sharpness of the display. Photographs were taken at different viewing angles: (a)-(d) 0 degree, (e)-(h) ~30 degrees, (i)-(l) ~60 degrees.

6.8 References

[1] S. Roth, I. Ben-David, M. Ben-Chorin, D. Eliav, and O. Ben-David, "10.2: Wide gamut, high brightness multiple primaries single panel projection displays," in SID Symposium Digest of Technical Papers (Blackwell Publishing Ltd, 2003), p. 118.

[2] Z. Luo, Y. Chen, and S. T. Wu., "Wide color gamut LCD with a quantum dot backlight," Opt. Express **21**, 26269 (2013).

[3] T. V. Gunn, and W. H. Halstead, "Diffractive color separation fabrication." in Aerospace/Defense Sensing and Controls (International Society for Optics and Photonics, 1998), p. 198.

[4] C. Joubert, B. Loiseaux, A. Delboulbe, and J. P. Huignard, "Phase volume holographic optical components for high-brightness single-LCD projectors," Appl. Opt. **36**, 4761 (1997).

[5] Y. Taira, D. Nakano, H. Numata, A. Nishikai, S. Ono, F. Yamada, M. Suzuki, M. Noguchi, R. Singh, and E. G. Colgan, "50.1: Low-power LCD using a Novel Optical System," in SID Symposium Digest of Technical Papers (Blackwell Publishing Ltd, 2002), p. 1313.

[6] H. H. Lin, and M. H. Lu, "Design of hybrid grating for color filter application in liquid crystal display," Jpn. J. Appl. Phys. **46**, 5414 (2007).

[7] P. Wang, J. A. Dominguez-Caballero, D. J. Friedman, and R. Menon, "A new class of multi-bandgap high-efficiency photovoltaics enabled by broadband diffractive optics," Prog. Photovolt.: Res. and Appl. **23**, 1073 (2014).

[8] N. Mohammad, P. Wang, D. J. Friedman, and R. Menon, "Enhancing photovoltaic output power by 3-band spectrum-splitting and concentration using a diffractive micro-optic," Opt. Express **22**, A1519 (2014).

[9] P. Wang, N. Mohammad, and Rajesh Menon, "Chromatic-aberration-corrected diffractive lenses for ultra-broadband focusing," Sci. Rep. **6**, 21545 (2016).

[10] G. Kim, J. A. Dominguez-Caballero, and R. Menon, "Design and analysis of multi-wavelength diffractive optics," Opt. Express **20**, 2814 (2012).

[11] K. Reimer, H. J. Quenzer, M. Jurss, and B. Wagner, "Micro-optic fabrication using one-level gray-tone lithography," Proc. SPIE **3008**, 279-288 (1997).

[12] Data sheet of Heidelberg μPG 101: http://www.himt.de/index.php/upg-101.html

[13] Data sheet of S1813: http://www.microchem.com/PDFs_Dow/S1800.pdf

CHAPTER 7

FULL-COLOR, LARGE AREA, TRANSMISSIVE HOLOGRAMS

This chapter is adapted with permission from the author's previous publication: N. Mohammad, M. Meem, X. Wan, and R. Menon, "Full-color, large area, transmissive holograms enabled by multi-level diffractive optics," Sci. Rep. **7**, 5789 (2017).

7.1 Abstract

We show that multilevel diffractive microstructures can enable broadband, on-axis transmissive holograms that can project complex full-color images, which are invariant to viewing angle. Compared to alternatives like metaholograms, diffractive holograms utilize much larger minimum features (>10µm), much smaller aspect ratios (<0.2) and thereby, can be fabricated in a single lithography step over relatively large areas (>30mmX30mm). We designed, fabricated and characterized holograms that encode various full-color images. Our devices demonstrate absolute transmission efficiencies of >86% across the visible spectrum from 405nm to 633nm (peak value of about 92%), and excellent color fidelity. Furthermore, these devices do not exhibit polarization dependence. Finally, we emphasize that our devices exhibit negligible absorption and are phase-only holograms with high diffraction efficiency.

7.2 Introduction

The word, hologram originates from the Greek word, holos, which means whole [1]. In general, the whole refers to the ability to control phase and amplitude of a wavefront to create a desired intensity image projection. In conventional holography, this is achieved via the interference between two coherent beams, one containing the information about the scene and another a reference beam [2]. Digital holograms and computer-generated holograms have also been used extensively to achieve the same effect either via spatial-light modulators [3] or using surface-relief structures [4]. Lipmann photographs is a class of color holograms, where broadband interference fringes were recorded in a special photopolymer medium [5]. However, their efficiency and field of view are highly limited

due to the underlying Bragg diffraction. It is well known that multilevel diffractive optics (also referred to as kinoforms) can achieve very high efficiencies at a single wavelength [6, 7]. However, extension to full color computer-generated holograms is challenging and typically requires one device for each color [8]. In addition, such surface-relief devices required multistep lithographic processes, exhibited relatively low diffraction efficiencies and required coherent illumination. Metasurfaces, which may be defined as 2D photonic devices whose unit cells are comprised of subwavelength structures, have recently been applied to holography [9-15]. These devices can engineer the amplitude, phase and polarization of light. The key functional difference between conventional holograms that utilize superwavelength features and metasurfaces is the fact that metasurfaces can manipulate vector properties of the electromagnetic wave, namely polarization [16,17]. Here, we emphasize that if one is interested in only scalar properties of light, such as intensity images, then metasurfaces are not required. In fact, metasurface-based holograms require very complex fabrication due to the subwavelength constituent features. Furthermore, they generally suffer from polarization dependence and relatively small operating bandwidths. Previously, we have described numerical studies of broadband transmissive holograms with peak efficiency greater than 90% that do not have any of the disadvantages of metasurfaces [18]. Here, we experimentally demonstrate high-efficiency, on-axis, transparent, full-color holograms using multilevel diffractive optics.

Broadband diffractive optical elements using multilevel superwavelength features have been applied for spectrum-splitting and concentration in photovoltaics [19-21], and for super-achromatic cylindrical lenses [22]. In this work, we extend the application of this concept to broadband computer-generated holography by designing, fabricating and

characterizing a variety of holograms. We show that average transmission efficiencies of over 86% can be achieved experimentally for the visible spectrum (405nm to 633nm). Note that transmission efficiency is the figure of merit used to characterize holograms based on metasurfaces [9]. We further show that complex image projections with large viewing angles such as color photographs can be achieved. All our devices utilize minimum feature size of 10µm or larger and can be readily manufactured using microimprinting or embossing techniques, potentially over large areas, if desired [23].

7.3 Working Principle

Each hologram is comprised of square pixels as shown in Figure 7.1(a). Each pixel has a width, Δ and the heights of the pixels can vary from 0 to a maximum height of H in steps of Δh. When illuminated with appropriate wavelenghts of light, the hologram produces an image at a certain distance, d. The pixel heights are selected using an optimization procedure based on the target design as described below. In this work, we used 3 different target images: a color-encoded image, where each color produces a different image (overlapping in space), a Macbeth color-chart to showcase the range of colors, and finally, a color photograph of an outdoor scene. In the first design, our minimum feature size is 10µm and maximum pixel height is 2µm. In the 2nd design, the minimum feature size is 20µm and the maximum pixel height is 2µm, while for the 3rd design, the minimum feature size is 20µm and the maximum pixel height is 2.4µm. The large pixel widths ensure that these device are polarization independent. In all cases, we designed the devices for 3 discrete wavelengths, 405nm, 532nm and 633nm. All the devices were designed using periodic boundary conditions. Other geometric and design parameters are

fully described in the supplementary information.

The holograms are designed using nonlinear optimization with the objective of maximizing a figure of a merit defined as [18]:

$$\eta = \frac{1}{N}\sum_\lambda \frac{\sum_m \sum_n I_T^{(\lambda)}|U(p_{m,n})|^2}{P_{in}^{(\lambda)}} \quad (7.1)$$

where, η is the wavelength averaged diffraction efficiency, λ is the design wavelength, N is the number of design wavelengths, $I_T^{(\lambda)}$ is the target image pattern at wavelength λ, $U(p_{m,n})$ is the complex amplitude at the reconstruction plane diffracted by the hologram with height profile distribution $p_{m,n}$, m and n are the pixel indices, and $P_{in}^{(\lambda)}$ is the input power at wavelength λ. The objective of the optimization is to determine a height profile $(p_{m,n})$ so that the wavelength averaged diffraction efficiency is maximized.

7.4 Experiment and Results

The holograms were fabricated using single-step grayscale lithography on a glass wafer spin coated with positive photoresist. In order to emulate the periodic boundary conditions used during design, the same design was repeated 3 times in the X direction and 3 times in the Y direction during fabrication. Details of the fabrication process are described in the supplementary information. For characterization, each hologram was illuminated by a collimated beam from a supercontinuum source with a tunable bandpass filter or from a white collimated backlight. The projected intensity images were captured either onto an image sensor (see Figure 7.5) or projected onto a screen and photographed (see Figure 7.6). A white translucent screen was used to capture on-axis images in

transmission, while an opaque white screen was used to capture off-axis images in reflection. Further details of the imaging setup and characterization procedure are described in the supplementary information.

The diffraction efficiency (η_{diff}) was calculated as the power inside the outline of the target image divided by the total power inside the aperture of the hologram (see equation 7.1). This definition follows that used in ref [18] and we adopt this same metric during design. This metric was measured only for the simple images in the color-encoded hologram. For all holograms, we also measured the transmission efficiency (η_{trans}) as described later. Details of the efficiency measurements are included in the supplementary information.

The target images for the color-encoded hologram are the letters "R", "G" and "B" at λ=633nm, 532nm and 405nm, respectively. The designed pixel-height distribution is shown in Figure 7.1(b), while the optical micrograph of a small portion of the device is shown in Figure 7.1(c). We measured the pixel heights of the fabricated device and estimated the average error as only 46nm (see the supplementary information). Although the blue wavelength used for design was 405nm, we had to use 415nm during the experiments, since that was the lowest wavelength with sufficient power accessible with our super-continuum source. Furthermore, the quantum efficiency of the image sensor is low at 405nm. The simulated image at 405nm is included in the supplementary information (Figure 7.8). The simulated images at λ=633nm, 532nm and 415nm are shown in Figures 7.1(d)-(f), respectively. Photographs of the corresponding images reflected off an opaque white screen are shown in Figures 7.1(g)-(i) (see the supplementary information for setup). The illumination bandwidth in each case was 10nm. Corresponding images were also

captured directly onto an image sensor (Figure 7.10 and setup in Figure 7.5) and the diffraction efficiencies were computed from these images. There is good qualitative agreement between the measured and simulated images. The measured average diffraction efficiencies are lower than expected (61% in experiments vs 74% in simulations). The discrepancy can be partly attributed to imperfect collimation of the incident light, which also accounts for blurring of the image edges compared to the simulations. We also performed a careful experimental analysis of the spectral response of this hologram and described the results in Figure 7.11. These images clearly show the transitions between the images at wavelengths intermediate to the design wavelengths.

The second device we designed had a target image of a portion of the Macbeth color chart. The design pixel-height distribution is shown in Figure 7.2(a) and an optical micrograph of a small portion of the fabricated device is shown in Figure 7.2(b). The target image, the simulated image and a photograph of the experimental image projected onto a translucent white screen (see Figure 7.6(a) for details) are shown in Figures 7.2(c), (d), and (e), respectively. The dashed white lines in Figure 7.2(e) demarcate one period of the image. Figure 7.2(f) shows the photograph of the image projected onto an opaque white screen (see Figure 7.6(b) for details). Note that the photograph was taken at an oblique viewing angle illustrating that the image quality is maintained for a large range of viewing angles. Photographs taken at many other viewing angles are also shown in Figure 7.14. Full white spectrum from the supercontinuum source (Figure 7.7 blue curve) was used as illumination in both cases. The simulated diffraction efficiencies (from equation 7.1) for this device were 64%, 53% and 65% at λ=633nm, 532nm and 405nm, respectively. The color range of the Macbeth chart is reproduced reasonably well considering that the design

was performed only for 3 discrete wavelengths. Using more wavelengths during design will increase the color-reproduction accuracy.

The third device encodes a color photograph and its pixel-height distribution is shown in Figure 7.3(a). An optical micrograph of a portion of the fabricated device is shown in Figure 7.3(b). The simulated diffraction efficiencies were 77%, 85% and 86% for λ=633nm, 532nm and 405nm, respectively. The target image, the simulated image and a photograph of 3 X 3 periods of the projected image reflected off an opaque white screen are shown in Figures 7.3(c), (d) and (e), respectively. Note that the photograph indicates good color reproduction even at an oblique viewing angle. Photographs at many more viewing angles are shown in Figure 7.15. In order to increase the resolution of the projected image, we also designed and fabricated another device containing 1500 X 1500 pixels (Figure 7.13). To reduce fabrication time, only one period of this device was fabricated and characterized. A photograph of the projected image reflecting off an opaque white screen is shown in Figure 7.3(f). A photograph of this single-period hologram is shown in Figure 7.3(g). This result coupled with the simulated image of a single-period hologram (Figure 7.13) confirms that periodic boundary conditions are not a limitation of our design method. In all cases in Figure 7.3, the devices were illuminated with the white collimated backlight.

We also measured the transmission efficiency of our devices. Note that transmission efficiency was used earlier as a figure of merit for metalens-based holograms [9]. First, an aperture of the same size as one period of the hologram was placed directly in front of the hologram (see Figure 7.12). The absolute transmission efficiency was defined as the ratio of the power transmitted through the hologram to that incident on the hologram. We also measured the relative transmission efficiency, which is defined as the ratio of the

power transmitted through the hologram to that transmitted through an unpatterned region. The results, as a function of illumination wavelength, are plotted in Figure 7.4 (dashed lines show absolute values, while solid lines show relative values). The illumination was the supercontinuum source coupled to a tunable filter. A bandwidth of 10nm was used for each wavelength sample for the transmission-efficiency measurements. The average absolute transmission efficiencies (from 405nm to 633nm) are 87%, 87% and 86% for the color-encoded hologram, the photograph hologram and the Macbeth hologram, respectively. Some of the relative efficiencies are higher than 100% indicating that the hologram pattern acts as an antireflection coating (right inset in Figure 7.4). It is useful to note that the absolute transmission efficiencies can be even higher by applying a properly designed antireflection coating on the unpatterned side of the hologram substrate.

7.5 Conclusions

In conclusion, we show that broadband transmissive holograms can be enabled by multilevel diffractive optics, which are much simpler to fabricate and offer polarization independence than when compared to alternatives such as those based upon metasurfaces. This is another example of an application where diffractive optics is sufficient when manipulating scalar properties of the electromagnetic field (intensity in this case). Multi-level diffractive optics can be readily manufactured at low cost via embossing techniques [23] that have been used to create surface-relief-based Bragg holograms. However, unlike Bragg holograms, multilevel diffractive holograms can be transmissive and create images that are relatively invariant with viewing angle. We note that there has been significant progress in the design methods of color computer-generated holograms (CGHs) using

techniques like depth division and space division to multiplex the images at different wavelengths [24-26]. However, experimental demonstrations of such devices often utilize spatial-light modulators and therefore are constrained by the associated space-bandwidth product. Furthermore, these require relatively narrowband sources such as lasers or light-emitting diodes. Broadband white sources have been used for certain color CGHs. However these suffer from significant chromatic aberrations especially at higher resolutions.

<u>7.6 Supplementary Information</u>

7.6.1 Design and Geometric Parameters of the Holograms

The holograms are pixelated in X and Y directions, and height of each pixel is quantized into multiple levels. Different parameters have been used for the three hologram designs. These are summarized in Table 7.1. The simulated diffraction efficiencies for the three designs are summarized in Table 7.2.

7.6.2 Fabrication

Direct laser-write lithography [27] was used to fabricate the holograms in a single lithography step using the grayscale mode. Shipley 1813 photoresist [28] was spin coated on RCA cleaned 2" D263 glass wafers at 1000 rpm. The samples were then baked in an oven at 110 degree C for 30 minutes. The hologram designs were written on the samples using Heidelberg Micro Pattern Generator 101 tool [29] and developed in AZ 1:1 solution [30] for 1 minute 30 seconds. A calibration step was performed on a separate sample (prepared with the same process conditions) before fabricating the holograms. The goal of

the calibration step was to determine the exposed depths at a particular gray scale level. Details of the calibration have been discussed elsewhere [31].

7.6.3 Imaging Setup

We used 3 different methods to characterize the holograms. A color sensor (DFM 22BUCO3-ML, Imaging Source) [34] was placed at the reconstruction plane of the hologram to record the image as shown in Figure 7.5. Secondly, we projected the image onto a translucent white screen and photographed the image from behind but on-axis as illustrated in Figure 7.6(a). Thirdly, we also simply projected the image onto a white screen and photographed the reflected image (Figure 7.6(b)). We used two different illumination sources. One was collimated and expanded beam from SuperK VARIA filter [32] which in turn connected to SuperK EXTREME EXW-6 source [33] while the other was a white collimated backlight. In the case of the color-encoded hologram, the device was illuminated with the three wavelengths from the SuperK (415 nm, 532 nm, 633 nm with 10 nm bandwidth) one by one and corresponding reconstructed images were captured with the setup shown in Figure 7.5. These images are shown in Figures 7.10 and 7.11. The images were also projected onto a white screen and photographed using the setup shown in Figure 7.6(b). These images were shown in Figure 7.1(h-j). Note that 415 nm was used instead of 405 nm because of the low quantum efficiency of the color sensor at this wavelength and due to the low power from our source at 405nm. In the case of the Macbeth color-chart and the photograph holograms, the reconstructed images were captured using the setups shown in Figure 7.6. The image shown in Figure 7.2(e) was taken using the setup shown in Figure 7.6(a) while those in Figures 7.2(f), 7.3(e) and 7.3(f) were taken with the

setup shown in Figure 7.6(b). The illumination source was SuperK (405nm-633nm) for the images in Figures 7.2(e) and 7.2(f) and collimated white backlight for those Figures 7.3(e) and 7.3(f). More details about the source spectra are described in the next section.

7.6.4 Incident Spectra

As describe in the last section, we used two types of illumination for the holograms. The first used a super-continuum source (NKT Photonics) coupled with a tunable filter (Varia from NKT Photonics), which allows us to create spatially coherent light, whose central wavelength and bandwidth can be selected. We performed narrowband illumination to characterize the color-encoded holograms as described in the main text. For all other holograms, we used the full visible spectrum, and the measured incident spectrum from this source is shown in Figure 7.7 (blue curve).

The second source we used was a collimated white backlight placed about 2m away from the hologram to ensure that the illumination was collimated. The incident spectrum of this source is shown in Figure 7.7 (red curve).

7.6.5 Design of Color-Encoded-Hologram

The color-encoded hologram was designed for $\lambda=405$nm, 532nm, 633nm. Due to the low quantum efficiency of the color sensor, illumination wavelength was set to 415nm instead of and this result was shown in the main text. The simulated image at the design wavelength in blue, $\lambda=405$nm is shown in Figure 7.8. The difference is minimal between 415nm and 405nm.

7.6.6 Metrology of the Fabricated Color-Encoded-Hologram

The pixel heights of the fabricated color-encoded hologram were measured using a stylus profilometer. Five pixel rows were measured for simplicity. The results along with the design values are summarized in Figure 7.9. From these data, we estimated an average error in pixel height of 46nm and a standard deviation of 33nm.

7.6.7 Image Captured on Sensor

In case of the color-encoded-hologram, the diffraction efficiencies were determined from the images captured on the color image sensor. The captured images are shown in Figure 7.10.

7.6.8 Spectral Analysis

The holograms were designed for three discrete wavelengths: 405 nm, 532 nm and 633 nm. To investigate the spectral response of the hologram designs, the holograms were illuminated at 14 different wavelengths with 10 nm bandwidth. Here, the response of only the color-encoded hologram is presented. The setup shown in Figure 7.5 was used for this purpose. For each illumination wavelength, corresponding reconstructed image was captured by the color sensor. In each case, a dark image was also recorded and subtracted from the reconstructed images. These raw images were then normalized and converted into gray scale images. Both the raw and grayscale images are presented in Figure 7.11.

7.6.9 Calculation of Transmission and Diffraction Efficiency

An aperture with dimension equal to one period of the hologram design was placed in front of it (see Figure 7.12). A power meter (PM 100A-S130C sensor, Thorlabs) was used to measure the power of the transmitted beam through the hologram pattern, unpatterned photoresist and aperture. Absolute transmission efficiency was then calculated by taking the ratio of the power through the hologram pattern and power through the aperture. Ratio of the power through the hologram pattern and unpatterned photoresist was used to calculate the relative transmission efficiency.

To determine the diffraction efficiency of the color-encoded hologram experimentally, the ratio of the intensity integrated over the letters to the intensity over one period was calculated from the images captured by the sensor. Corresponding dark images were subtracted in each case.

7.6.10 Design of 1500X1500 Pixel Hologram

As described in the main text, we also designed a high-resolution hologram that projects a photographic image. In this case, we used 1500 X 1500 pixels for one period. The distance between hologram and the image was 1m. The designed height distribution of this device is shown in Figure 7.13(a) and 50 X 50 pixels in the top left corner are shown in Figure 7.13(b). The simulated image is shown in Figure 7.13(c). A photograph of the fabricated device is shown in Figure 7.13(d).

7.6.11 Images at Various Viewing Angles

The images at various viewing angles are shown in Figures 7.14 and 7.15.

7.7 Author Contributions

R.M. and N.M. conceived and designed the experiments. M.M. and X.W. modeled and optimized the devices. N.M. and M.M. fabricated the devices, performed the experiments and numerical analysis. N.M. and R.M. analyzed the data and wrote the paper.
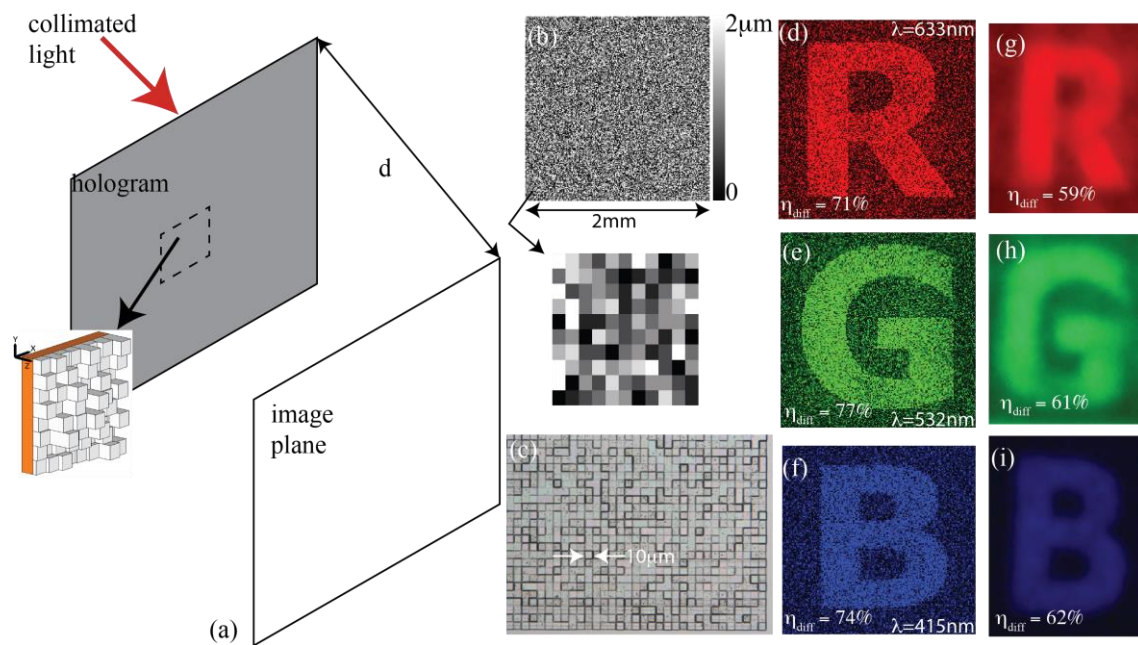

Figure 7.1. Working principle of the hologram. (a) Schematic of hologram. (b) Designed height map of color-encoded hologram. Bottom inset: Magnified view of 11X10 pixels of bottom left corner. (c) Magnified optical micrograph of a small portion of the device. Simulated images at (d) λ=633nm, (e) λ =532nm and (f) λ =415nm are shown. The corresponding experimental images reflecting of a white opaque screen are shown in (g)-(i), respectively. The simulated and measured diffraction efficiencies are noted in each image.
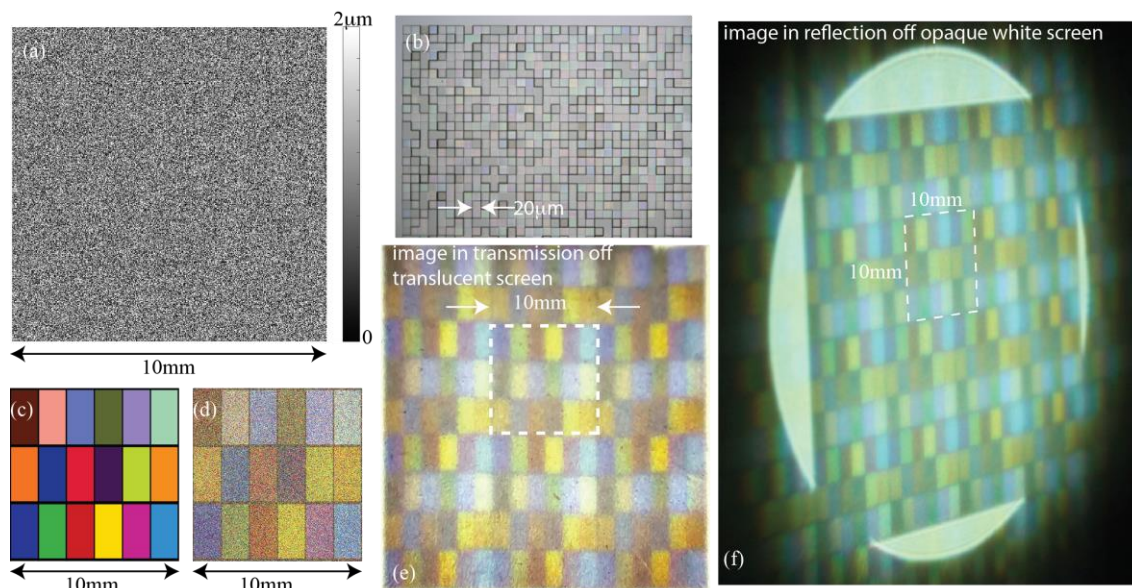
Figure 7.2. Hologram encoding a Macbeth color chart. (a) Design height map of the hologram. (b) Optical micrograph of a portion of the hologram. (c) Target image of the Macbeth chart. (d) Simulated image created by the hologram, when it is illuminated by the design wavelengths. (e) Photograph of the image on a white translucent screen taken in transmission at normal viewing angle. Note that the color image does not change with viewing angle (also see Figs. S10 and S11). (f) Photograph of the image reflected off a white opaque screen taken at an oblique viewing angle. Illumination is full white spectrum from supercontinuum source for both (e) and (f).
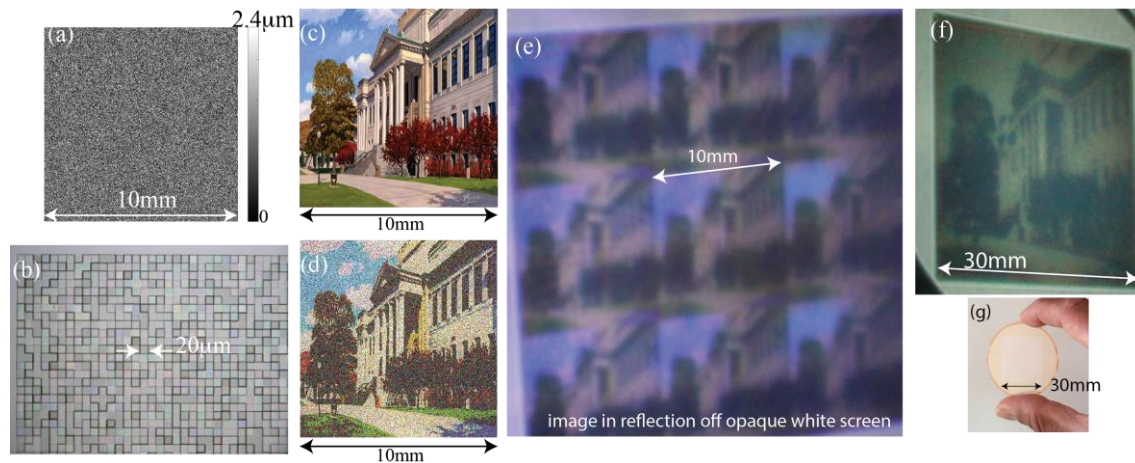
Figure 7.3. Hologram encoding a color photograph. (a) Design height map of the hologram. (b) Optical micrograph of a portion of the fabricated device. (c) Target image corresponding to the color photograph. Image courtesy of the University of Utah. (d) Simulated image created by the hologram, when it is illuminated by the design wavelengths. (e) Photograph of the image reflected of a white opaque screen taken at a small oblique viewing angle. (f) Photograph of image reflected of a white opaque screen for a single-period hologram containing 1500 X 1500 pixels in a single period. In both (e) and (f), the hologram is illuminated by the full visible band. (g) Photograph of single-period hologram. Its size is 30mm X 30mm.
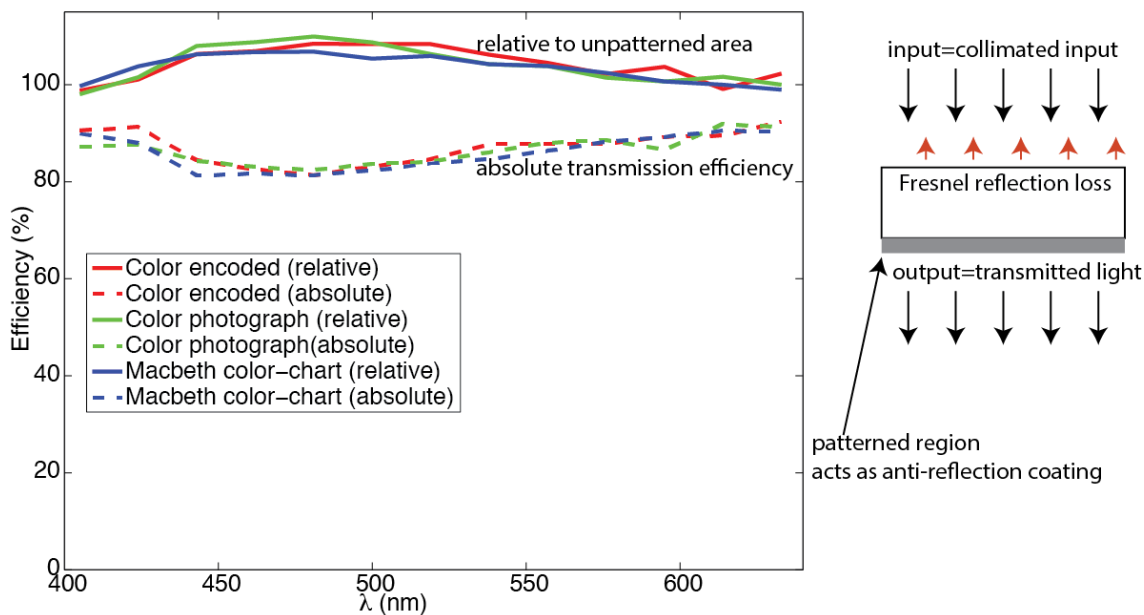
Figure 7.4. Measured transmission efficiency as a function of wavelength for the three hologram designs. The absolute transmission efficiencies are plotted using dashed lines, while the transmission efficiency relative to an unpatterned area is shown with solid lines. Right inset shows how the patterned region reduces reflection losses, which allows for greater than 100% relative transmission.
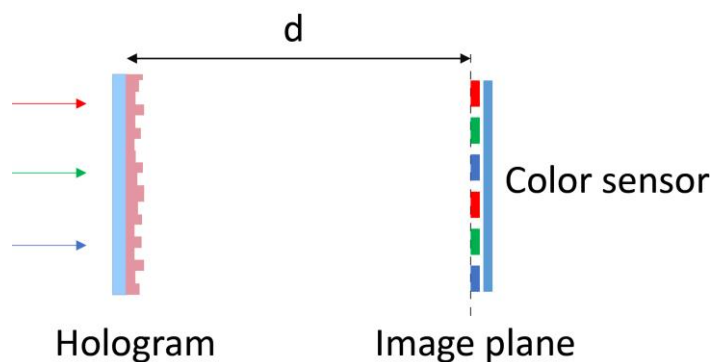

Figure 7.5. Schematics showing characterization of the hologram designs using a color sensor.
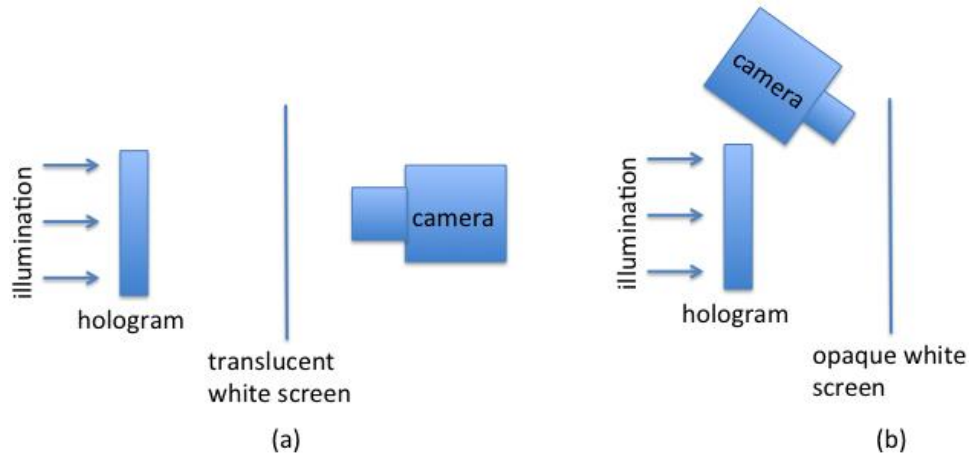
Figure 7.6. Schematic showing two other methods for characterizing the image projected by the hologram.

Figure 7.7. Measured incident spectra for visible illumination.
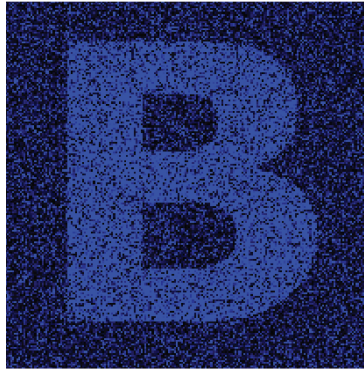
Figure 7.8. Simulated image of the color-encoded hologram, when illuminated at λ=405nm.
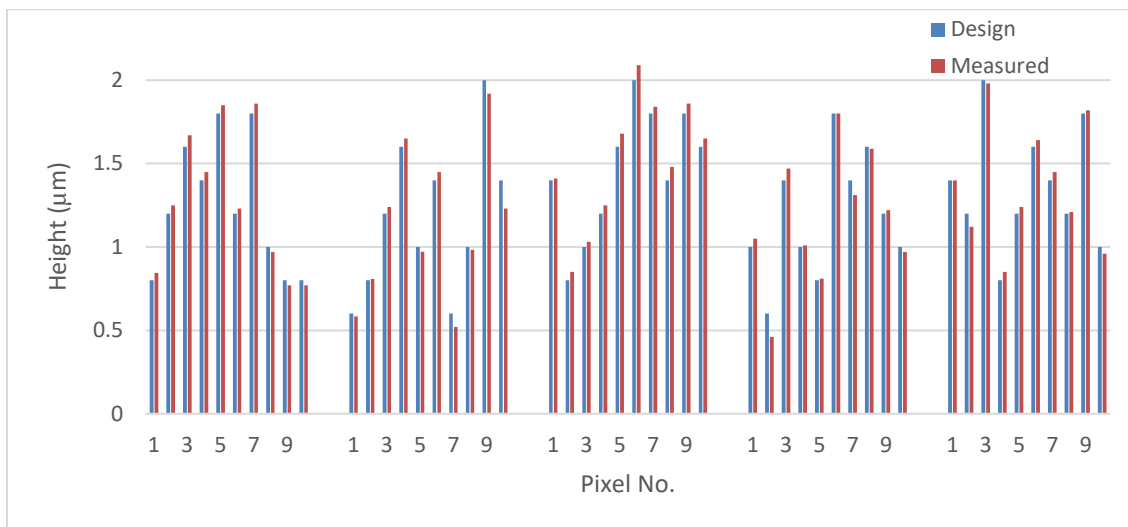
Figure 7.9. Measured pixel heights compared to design values for 5 rows of pixels for the color-encoded hologram.

λ = 633nm   λ = 532nm   λ = 415nm
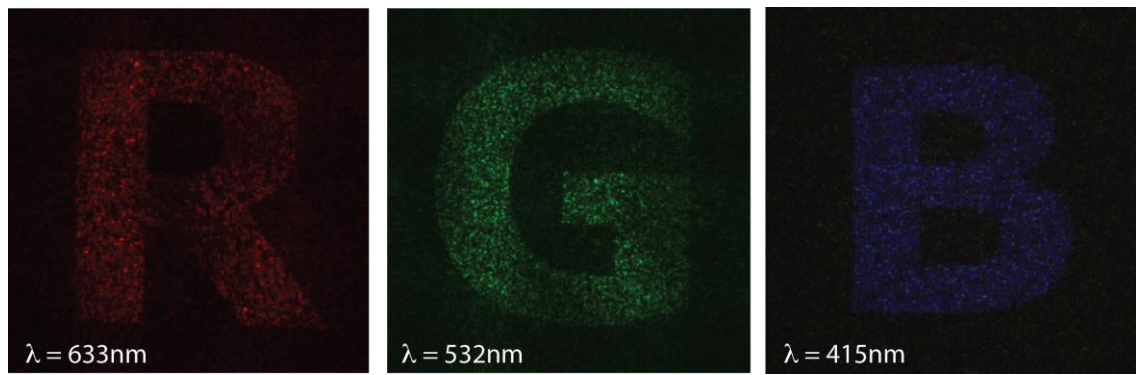
Figure 7.10. Images captured on color sensor for the color-encoded hologram.

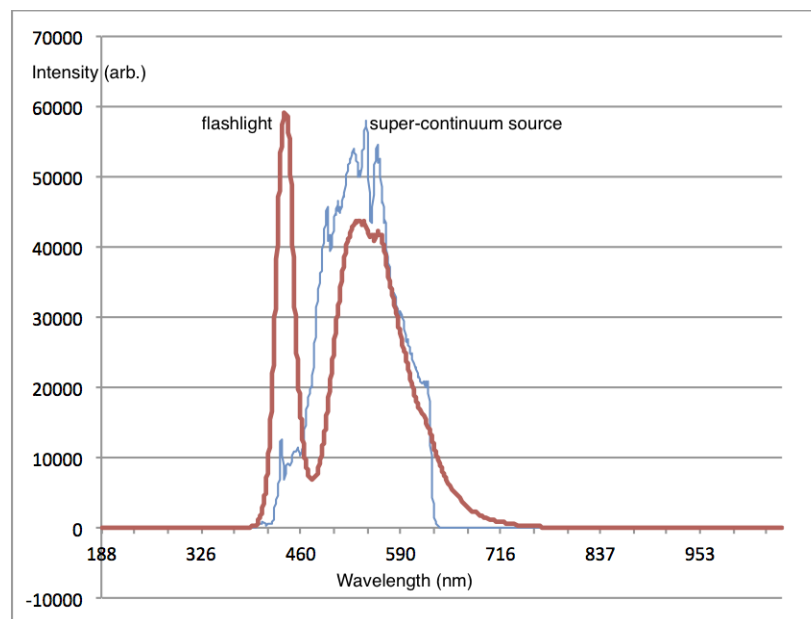|	raw	processed		raw	processed
405 nm			532 nm		
424 nm			538 nm		
443 nm			557 nm		
462 nm			576 nm		
481 nm			595 nm		
500 nm			614 nm		
519 nm			633 nm		
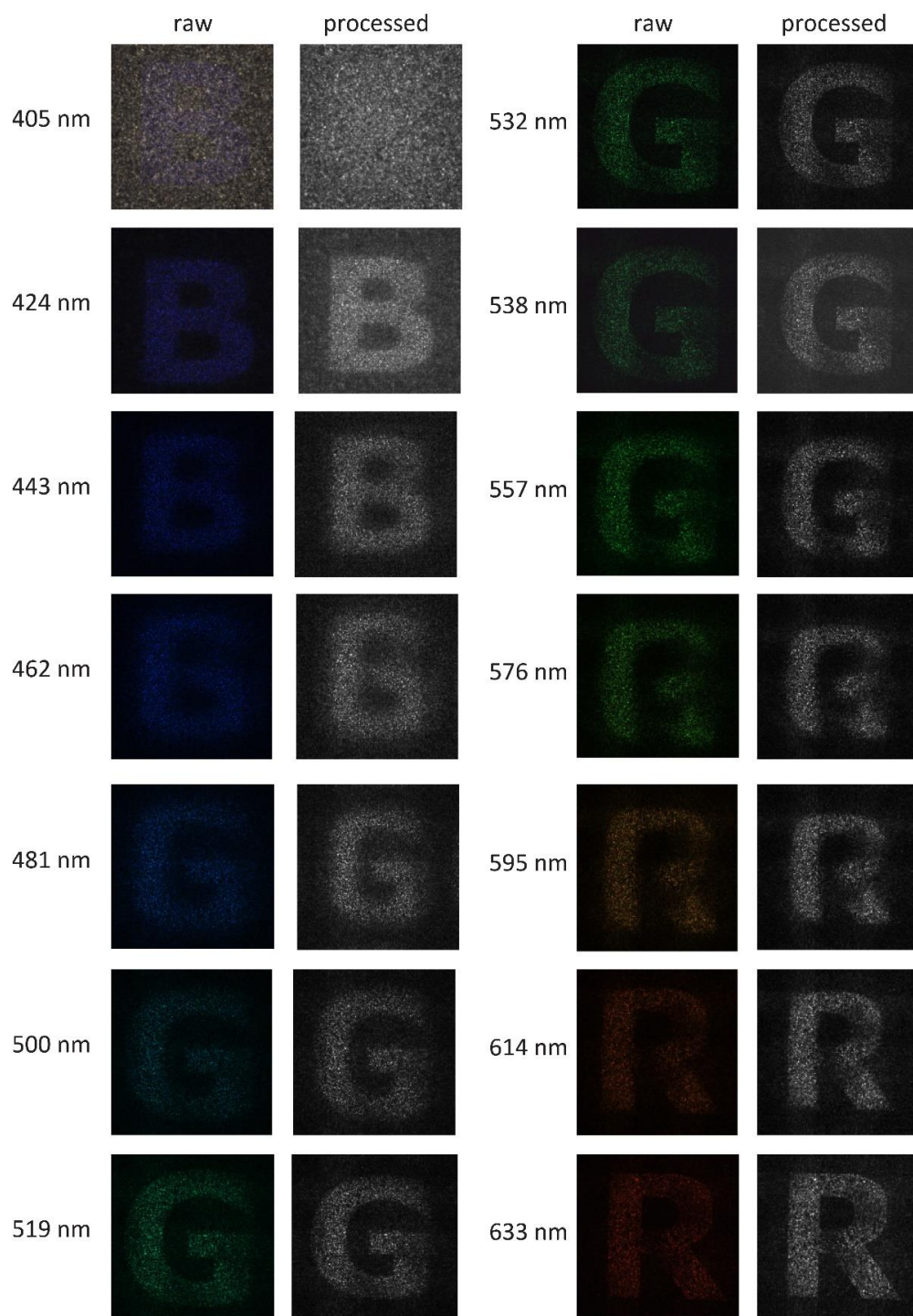
Figure 7.11 Experimental images of the color-encoded hologram at different wavelengths.
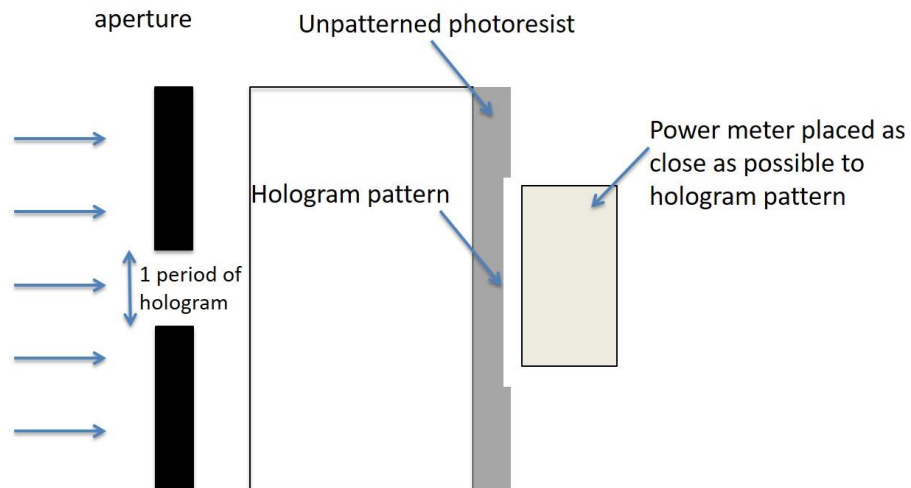
Figure 7.12. Setup used to measure the transmission efficiency of the holograms.
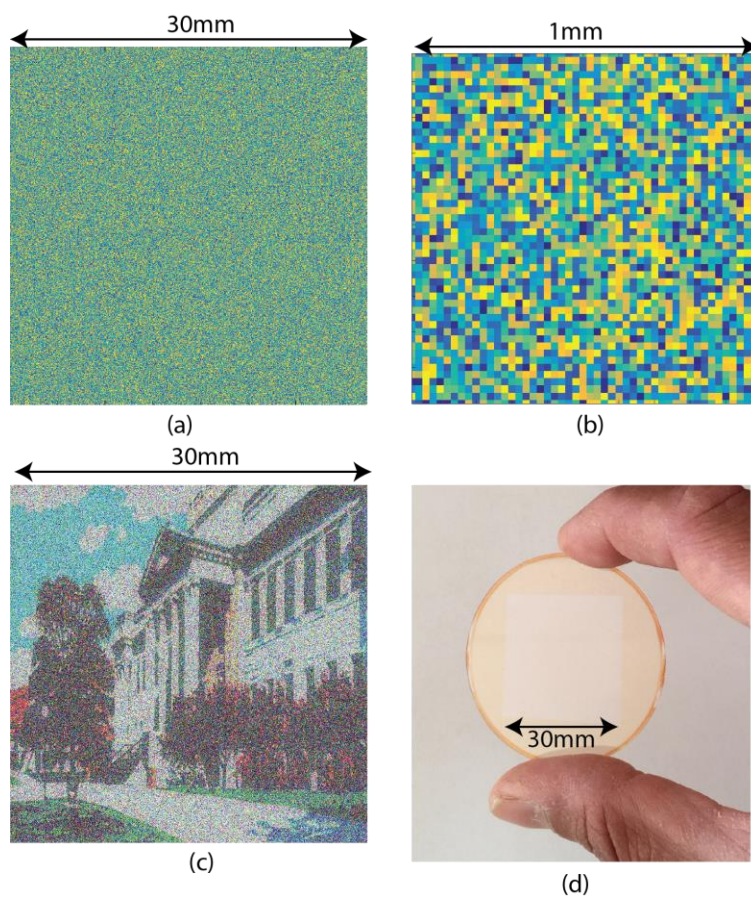
Figure 7.13. Hologram of photograph with 1500 X 1500 pixels. (a) Designed height distribution. (b) 50 X 50 pixels in the top left corner. (c) Simulated image. (d) Photograph of fabricated device.
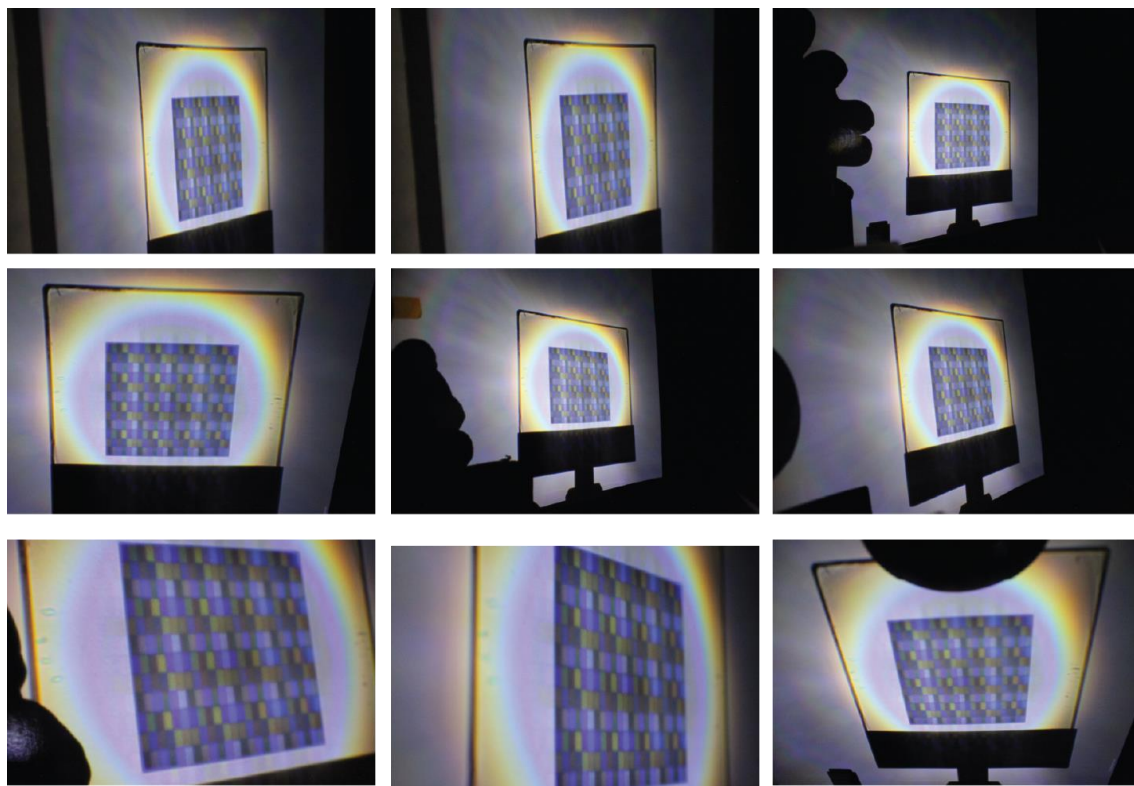
Figure 7.14. Images of the Macbeth hologram result at various viewing angles.
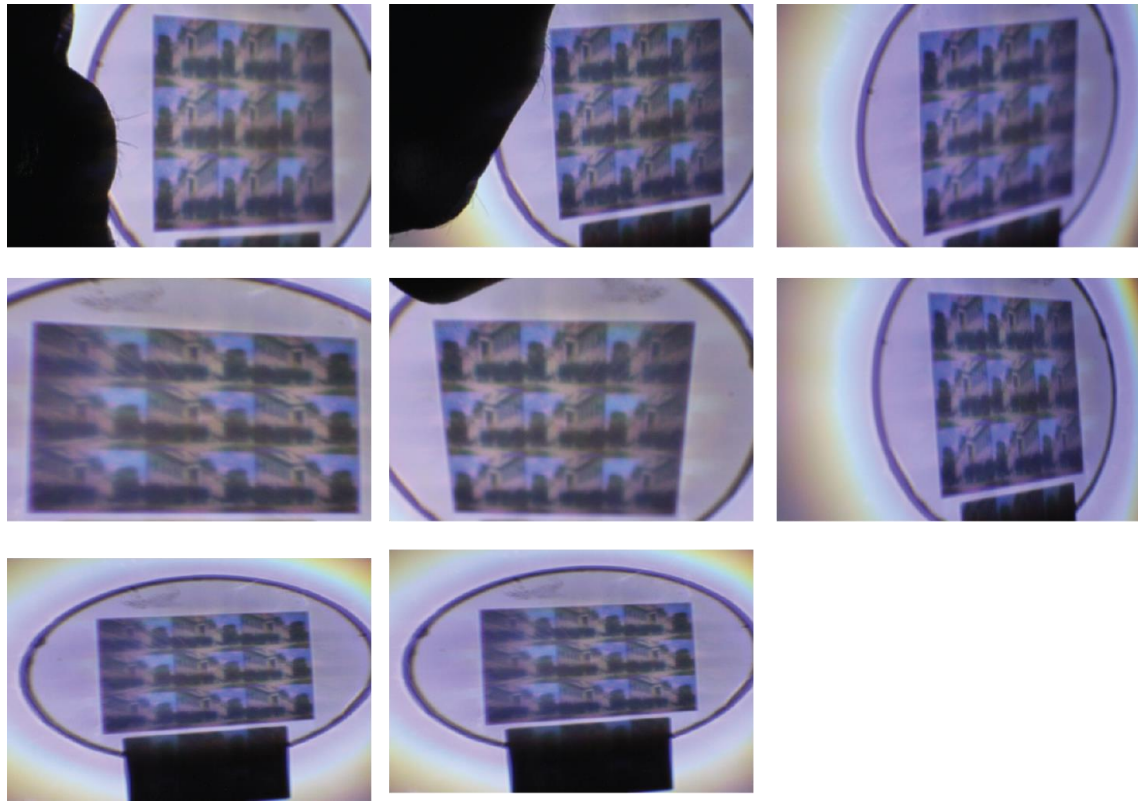
Figure 7.15. Images of the color-photograph hologram result at various viewing angles.

Table 7.1. Design and geometric parameters of three hologram designs.

Hologram design	Color-encoded	Macbeth color-chart	Photograph (also referred to as Park Building)
Pixel size (µm)	10	20	20
Number of pixels	201 X 201	500 X 500	500 X 500
Physical size (mm X mm)	2.01 X 2.01	10 X 10	10 X 10
Maximum height (µm)	2	2	2.4
Number of grayscale levels	8	64	88
Propagation distance (mm)	50	500	500
Design wavelengths (nm)	405, 532, 633	405, 532, 633	405, 532, 633
Refractive index at design wavelengths	1.6894, 1.6482, 1.6347	1.6894, 1.6482, 1.6347	1.6894, 1.6482, 1.6347

Table 7.2. Simulated diffraction efficiencies.

Channel	Color-encoded	Macbeth color-chart	Photograph
Red(633)	71.33	63.49	77.09
Green(532)	76.77	53.11	84.77
Blue(405)	74.63	65.24	86.30

7.8 References

[1] G. Dennis, "A new microscopic principle," Nat. **161**, 777-778 (1948).

[2] J. W. Goodman, *Introduction to Fourier Optics* (Roberts and Company Publishers, 2005).

[3] T. C. ed. Poon, *Digital Holography and Three-Dimensional Display: Principles and Applications* (Springer Science & Business Media, 2006).

[4] B. C. Kress, and P. Meyrueis, *Applied Digital Optics, from Micro-Optics to Nanophotonics* (John Wiley & Sons, 2009).

[5] H. I. Bjelkhagen, "New optical security device based on one-hundred-year-old photographic technique," Opt. Eng **38**, 55-61 (1999).

[6] M. Ekberg, B. Nilsson, M. Larsson, and S. Hård. "Multilevel phase holograms manufactured by electron-beam lithography," Opt. Lett. **15**, 568-569 (1990).

[7] D. A. Buralli, G. M. Morris, and J. R. Rogers, "Optical performance of holographic kinoforms," Appl. Opt. **28**, 976-983 (1989).

[8] K. S. Choi, B. S. Choi, Y. S. Choi, S. I. Kim, J. M. Kim, N. Kim, and S. K. Gil, "Multiphase computer-generated holograms for full-color image generation," P. Soc. Photo-Opt. Ins. 4659, 242-249 (2002).

[9] R. C. Devlin, M. Khorasaninejad, W. T. Chen, J. Oh, and F. Capasso, "Broadband high-efficiency dielectric metasurfaces for the visible spectrum," P. Natl. A. Sci. **113**, 10473–10478 (2016).

[10] Wang, Lei, S. Kruk, H. Tang, T. Li, I. Kravchenko, D. N. Neshev, and Y. S. Kivshar, "Grayscale transparent metasurface holograms," Optica **3**, 1504-1505 (2016).

[11] X. Ni, A. V. Kildishev, and V. M. Shalaev, "Metasurface holograms for visible light," Nat. Commun. **4**, 2807 (2013).

[12] W. T. Chen, K. Yu. Yang, C. M. Wang, Y. W. Huang, G. Sun, I. D. Chiang, C. Y. Liao, W.L. Hsu, H.T. Lin, S. Sun, and L. Zhou, "High-efficiency broadband meta-hologram with polarization-controlled dual images" Nano Lett. **14**, 225-230 (2013).

[13] G. Zheng, H. Mühlenbernd, M. Kenney, G. Li, T. Zentgraf, and S. Zhang, "Metasurface holograms reaching 80% efficiency," Nat. Nanotechnol. **10**, 308-312 (2015).

[14] B. Wang, F. Dong, Q. T. Li, D. Yang, C. Sun, J. Chen, Z. Song, L. Xu, W. Chu, Y. F. Xiao, and Q. Gong, "Visible-frequency dielectric metasurfaces for multiwavelength achromatic and highly dispersive holograms," Nano Lett. **16**, 5235-5240 (2016).

[15] Q. Wang, X. Zhang, Y. Xu, J. Gu, Y. Li, Z. Tian, R. Singh, S. Zhang, J. Han, and W. Zhang, "Broadband metasurface holograms: toward complete phase and amplitude engineering" Sci. Rep. **6**, 32867 (2016).

[16] D. Wen, F. Yue, G. Li, G. Zheng, K. Chan, S. Chen, M. Chen. K. F. Li, P. W. H. Wong, K. W. Cheah, and E. Y. B. Pun, "Helicity multiplexed broadband metasurface holograms," Nat. Commun. **6**, 8241 (2015).

[17] M. Khorasaninejad, A. Ambrosio, P. Kanhaiya, and F. Capasso, "Broadband and chiral binary dielectric meta-holograms," Science Advances **2**, e1501258 (2016).

[18] G. Kim, J. A. Domínguez-Caballero, and R. Menon, "Design and analysis of multi-wavelength diffractive optics," Opt. Express **20**, 2814-2823 (2012).

[19] P. Wang, J. A. Dominguez-Caballero, D. J. Friedman, and R. Menon, "A new class of multi-bandgap high-efficiency photovoltaics enabled by broadband diffractive optics," Prog. Photovolt: Res. Appl. **23**, 1073-1079 (2015).

[20] N. Mohammad, P. Wang, D. J. Friedman, and R. Menon, "Enhancing photovoltaic output power by 3-band spectrum-splitting and concentration using a diffractive micro-optic," Opt. Express **22**, A1519-A1525 (2014).

[21] N. Mohammad, M. Schulz, P. Wang, and R. Menon, "Outdoor measurements of a photovoltaic system using diffractive spectrum-splitting and concentration," AIP Adv. **6**, 095311 (2016).

[22] P. Wang, N. Mohammad, and R. Menon, "Chromatic-aberration-corrected diffractive lenses for ultra-broadband focusing," Sci. Rep. **6**, 21545 (2016).

[23] N. Kooy, K. Mohamed, L. T. Pin, and O. S. Guan, "A review of roll-to-roll nanoimprint lithography," Nanoscale Res. Lett. **9**, 320 (2014).

[24] T. Shimobaba, M. Makowski, Y. Nagahama, Y. Endo, R. Hirayama, D. Hiyama, S. Hasegawa, M. Sano, T. Kakue, M. Oikawa, and T. Sugie, "Color computer-generated hologram generation using the random phase-free method and color space conversion," Appl. Opt. **55**, 4159-4165 (2016).

[25] M. Makowski, M. Sypek, and A. Kolodziejczyk, "Colorful reconstructions from a thin multi-plane phase hologram," Opt. Exp. **16**, 11618-11623 (2008).

[26] T. Ito, T. Shimobaba, H. Godo, and M. Horiuchi, "Holographic reconstruction with a 10-µm pixel-pitch reflective liquid-crystal display by use of a light-emitting diode reference light," Opt. Lett. **27**, 1406-1408 (2002).

[27] C. McKenna, K. Walsh, M. Crain, and J. Lake, "Maskless direct write grayscale lithography for MEMS applications," In Micro/Nano Symposium (UGIM), 2010 18th Biennial University/Government/Industry, pp. 1-4. IEEE, 2010.

[28] Data sheet of Shipley 1813 photoresist:
http://www.microchem.com/PDFs_Dow/S1800.pdf

[29] Data sheet of Heidelberg μPG 101: http://www.himt.de/index.php/upg-101.html

[30] Data sheet of AZ developer:http://www.microchemicals.com/micro/az_developer.pdf

[31] P. Wang, J. A. Dominguez-Caballero, D. J. Friedman, and R. Menon, "A new class of multi-bandgap high-efficiency photovoltaics enabled by broadband diffractive optics," Prog. Photovolt: Res. Appl. **23**, 1073-1079 (2015).

[32] Data sheet of SuperK Varia Filter:
http://www.nktphotonics.com/wp-content/uploads/2015/03/SuperK_VARIA.pdf

[33] Data sheet of SuperK Extreme:
http://www.nktphotonics.com/wp-content/uploads/2015/05/superk-extreme.pdf

[34] Data sheet of color camera:
https://s1.dl.theimagingsource.com/api/2.0/packages/publications/factsheets-single/fsdfm22buc03ml/c059478acb/fsdfm22buc03ml.en_US.pdf

CHAPTER 8

SUMMARY AND FUTURE WORK

8.1 Summary

In this dissertation, a recently developed diffractive micro-optical element (polychromat) has been explored extensively to solve different technological issues. The polychromat is ultrathin, flat and lightweight. It can create complex diffraction patterns with high efficiency under broadband illumination. It is a pixelated or grooved structure with multilevel height topography. Scalar diffraction theory along with modified direct binary search algorithm was used to optimize the height profile to achieve a desired diffraction pattern. The polychromat was fabricated using single step grayscale lithography.

Chapter 1 provided a brief description of diffractive optics, the significance of the polychromat over conventional diffractive optical elements as well as design and fabrication of this micro-optical element. Broadband applications of the polychromat were described in the rest of the dissertation (Chapters 2-7). This included a) a polychromat based photovoltaic system that produces more output power compared to a standard photovoltaic system via 3-band spectrum splitting and concentration b) outdoor measurements of a photovoltaic system that utilized polychromat for 2-band spectrum splitting and 3X concentration, c) a cylindrical lens that demonstrated chromatic aberration

correction over the entire visible range, d) an ultrathin flat diffractive lens for broadband imaging, e) a modified LCD that has high transmission efficiency achieved using diffractive color splitting, and f) transmission holograms that project complex full color images invariant to viewing angles.

8.2 Future Work

The algorithm that we used for optimizing the height profile requires a very large number of simulations due to its heuristic nature. The computation time increases significantly with the number of design variables hence making this algorithm very inefficient for large polychromat designs. Recently, inverse electromagnetic simulation called the adjoint method was demonstrated to optimize the height profile of such multi-level diffractive optical element. This approach does not scale with the number of design variables. As a result, large polychromat devices can be optimized without incurring an increase in computational time. As a next step, we are exploring better algorithms compared to the adjoint method to decrease the computational time further.

In our work, the pixel width (3 µm) was large compared to the maximum wavelength of light considered (1200 nm). Since reducing the pixel size will increase the efficiency of the polychromat, we plan to use a smaller pixel width in our next polychromat designs. However, as the pixel width approaches close to the wavelength, the scalar diffraction theory will no longer be valid. Therefore, we will incorporate full electromagnetic simulation in our design model.

We used direct laser write grayscale lithography to fabricate the polychromat devices. However, due to the limited resolution of the pattern generator tool we were

restricted to 3 µm pixel width in our case. A new pattern generator tool with smaller resolution (1.2 µm) is available at the Utah Nanofab now. We are working to optimize the grayscale process parameters for this tool. With the smaller pixel width, we expect to have higher diffraction efficiency of the polychromat which will benefit all the applications demonstrated in this dissertation as well as the future applications. Furthermore, we will explore proximity effects during grayscale lithography to reduce the fabrication errors. Besides the grayscale lithography, we plan to explore other lithography techniques such as two-photon 3D lithography and compare its performance over grayscale lithography.

In the photovoltaic project (Chapter 2 and 3), we utilized only one-dimensional form of the polychromat for spectrum splitting and concentration. As our next step, we will extend this work to two-dimensional spectrum splitting with four or more bandgap solar cells to absorb the spectral bands. This will increase the efficiency of the photovoltaic system by a large factor. Also, we aim to test the polychromat-photovoltaic system under direct sunlight over the whole year to better understand the impact of spectral variation on the polychromat performance. Also, we will develop an automatic tracking system for the polychromat-photovoltaic architecture.

The flat diffractive lenses described in Chapter 5 were designed for single wavelengths and the numerical aperture was low. We are currently designing, fabricating and characterizing multiwavelength diffractive lenses with higher numerical aperture (0.18). We also plan to build a compact camera using this ultrathin lens and compare it with the present solutions.

The hologram designs presented in Chapter 7 projected two-dimensional full-color images. The next logical step will be to demonstrate holograms that create three-

dimensional projection of complex objects. Currently, we are adapting our design code for this application.

Finally, all the polychromat devices were fabricated on photoresist spin coated on a glass substrate. For commercial applications, the polychromat needs to be manufactured in large scale with low cost. The industry already has well-developed fabrication processes such as nanoimprint lithography that we can utilize for mass production of polychromat. In the future, we will collaborate with external vendors to achieve this goal.

APPENDIX

An example code to calculate the diffraction pattern from a given height profile and other geometrical parameters is given here. In this case, the height profile of the polychromat generates the letters 'R', 'G' and 'B' as shown in Figures 7.1(d), (e) and (f). The code was written in MATLAB R2013a. To run this code, the user should first download the optimized height profile of the polychromat from the following location: https://www.dropbox.com/sh/lohtokvk972gdzr/AAC61DeRXUJ_mKPjWDZ7jIeqa?dl=0. Then the code shown in the following screenshots can be written in MATLAB and saved as .m file. Note that the design heights and the m file should be in the same folder. Once the simulation is run, it will show the images of the diffraction pattern.

```matlab
1 -     clear all; close all; clc;
2       %% Global parameters
3       % Geometric parameters
4 -     global pixelSize;                              % pixel size
5 -     global propDis;                                % propagation distance after the crystal
6 -     global lambda;                                 % wavelengths
7 -     global numLambda;                              % number of wavelength samples
8 -     global n_Poly;                                 % real part of refractive index of the material
9 -     global k_Poly;                                 % imaginary part of refractive index of the material
10      % Design and image
11 -    global designHeight;                           % design in height
12 -    global imageComplex;                           % complex image
13 -    global transferFunc;                           % transfer function
14 -    global RefIndex;                               % refractive index
15 -    global kvec;                                   % k vector
16
17      %% Physical constants
18 -    nm = single(1e-009);
19 -    um = single(1e-006);
20 -    mm = single(1e-003);
21
22      %% Parameters definition
23 -    pixelSize = 10 * um;                           % pixel size
24 -    propDis = 50 * mm;                             % propagation distance after the crystal
25 -    lambda = [405, 532, 633] * nm ;                % design wavelengths
26 -    numLambda = length(lambda);
27 -    n_Poly = single([1.6894, 1.6482, 1.6347]);     % real part of complex refractive index
28 -    k_Poly = single(zeros(size(n_Poly)));          % imaginary part of complex refractive index
29 -    kvec = 2*pi./lambda;
30
```

```matlab
%% Fourier transform
designHeight = importdata('designHeight.mat');

[numPixelYPadded, numPixelXPadded] = size(designHeight);
sizeXPadded = pixelSize * numPixelXPadded;
sizeYPadded = pixelSize * numPixelYPadded;

RefIndex = n_Poly + 1i * k_Poly;

du = 1 / sizeXPadded;
umax = 1 / (2 * pixelSize);
u = (-umax + du / 2) : du : (umax - du / 2);
[U] = meshgrid(u);
U = sqrt((U.^2) + ((U').^2));

for ww = 1 : numLambda
    % Cut-off frequencies
    u_ev = 1 / lambda(ww);                                          % evanescent cut off
    u_np = u_ev * (sizeXPadded / 2 / propDis);                      % Nyquist cut off
    u_cut = min(u_ev, u_np);                                        % cut-off frequency
    Wb = U < u_cut;
    % transfer and transmission functions
    transferFunc{ww} = exp(1i * 2 * pi * propDis / lambda(ww)) .* exp((-1i * pi * lambda(ww) * propDis) .* (U .^ 2));
    transferFunc{ww} = transferFunc{ww} .* Wb;
    phi{ww} = (2 * pi * (RefIndex(ww) - 1) / lambda(ww)) .* designHeight;
    Transmission{ww} = exp(1i .* phi{ww});
    % image complex
    imageComplex{ww} = ifft2(ifftshift(fftshift(fft2(Transmission{ww})) .* transferFunc{ww}));
end


red = double(abs(imageComplex{3}).^2); % Red channel
green = double(abs(imageComplex{2}).^2); % Green channel
blue = double(abs(imageComplex{1}).^2); % Blue channel
a = zeros(size(red));
just_red = cat(3, red, a, a);
just_green = cat(3, a, green, a);
just_blue = cat(3, a, a, blue);
figure, imshow(just_red), title('Red channel')
figure, imshow(just_green), title('Green channel')
figure, imshow(just_blue), title('Blue channel')
```